

DAIGI 789

COMPUTATION OF FLOW AND HEAT TRANSFER IN FLOW AROUND A  
180 DEG BEND(U) UNIVERSITY OF MANCHESTER INST OF  
SCIENCE AND TECHNOLOGY (ENGL) B E LAUNDER OCT 85  
N00014-83-G-0021

1/R

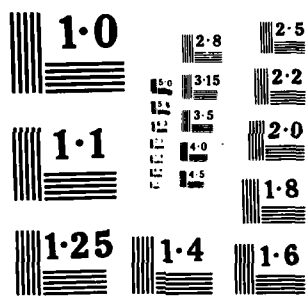
UNCLASSIFIED

F/G 20/4

NL



10-10-85



AD-A161 789

## 1. Introduction

The 1983/84 research year saw the completion of the GNR-funded research at UMIST on turbulent convective heat transfer in  $180^\circ$  bends. As last year, the main report is kept very brief but technical papers and reports are included as appendices. The main research effort during the year, has been directed at bends of circular cross section. Sections 3 and 4 deal respectively with experimental and computational aspects of this work. These are preceded in Section 2 by a brief account of further computational work in the square-sectioned duct. Finally, Section 5 attempts a summing up of what has been achieved and the questions that remain.

In Appendix 1 a complete list of theses and external publications arising from this project is provided. Here we have included contributions made jointly with Professor Humphrey's team at UC Berkeley with whom the whole research programme has been conducted in cordial and, we believe, effective collaboration.

## 2. Computational Studies on Square-Sectioned $180^\circ$ Bend

Following the completion of Johnson's [1] PhD work Professor Choi, an academic visitor to UMIST, continued explorations into the cause of the serious disagreement between experiment and computation for the case of a square-sectioned  $180^\circ$  bend. Several modifications were introduced to the numerical/physical model adopted by Johnson.

- (i) Initially, better estimates of the mean velocity profiles and the corresponding turbulence energy and dissipation profiles at the station just upstream of the bend were attempted. In particular, the representation of the weak streamwise vorticity generated by the anisotropic turbulent stress field during the flow development in the straight 30 diameter-long entry tangent was considerably improved and this led to significantly better agreement with experiment at the  $3^\circ$  position (i.e. just after the start of the bend). There was,

however, negligible effect of these changes in entry condition at stations further downstream. The resultant flow pattern at  $90^\circ$  seemed nearly insensitive to what conditions were prescribed three diameters upstream of the bend inlet.

- (ii) The PSL technique [2], facilitating a very fine near-wall mesh (without core penalty) was introduced first on the flat top wall and subsequently on the curved inner and outer walls of the bend. The desirability of doing this is seen in Figure 1 which shows that the maximum secondary velocity occurs very close to the top wall. With the usual coarse-grid "wall function" treatment the secondary flow is appreciably 'clipped'. Significant refinement of the primary mesh was also made both in the streamwise and cross-stream directions. The finest grid employed in the computations was  $27 \times 47 \times 130$ . Considering that the third-order QUICK scheme was used, it was our view that numerical errors had been reduced to unimportant levels.

Computations showed that (principally due to the use of PSL) the predicted behaviour at  $45^\circ$  into the bend was now in satisfactory agreement with experiment, Figure 2, if allowance were made for what appeared to be an error in the measured bulk flow rate. In Johnson's work, however, the main disagreement with the measured behaviour had not arisen until  $90^\circ$  into the bend. From Figure 3 it is seen that while definite improvements have resulted from the numerical refinements summarized above, there still remains very serious disagreement between the experimental and predicted behaviour.

- (iii) The conclusion drawn was that shortcomings in the turbulence model were principally responsible for remaining discrepancies between the computed and measured flow pattern. As a step in testing this conclusion, a modification was introduced to the "standard" form of the dissipation rate equation. With the  $k \sim \epsilon$  eddy viscosity model (employed over the whole

duct except the PSL region) the source of  $\epsilon$  is taken equal to

$$c_{\epsilon 1} \frac{\epsilon}{k} v_t \frac{\partial U_i}{\partial x_j} \left( \frac{\partial U_i}{\partial x_j} + \frac{\partial U_j}{\partial x_i} \right)$$

where  $v_t$  is the kinematic turbulent viscosity and  $U_i$  denotes the mean velocity in direction  $x_i$ . In some of the PI's earlier studies it has been found that dropping the part of this term involving  $\frac{\partial U_i}{\partial x_j} \frac{\partial U_j}{\partial x_i}$  brought at least qualitatively the correct response of  $v_t$  to streamline curvature. Accordingly, a set of  $180^\circ$ -bend computations was made for the case where the dissipation source term was abbreviated to

$$c_{\epsilon 1} \frac{\epsilon}{k} v_t \left( \frac{\partial U_i}{\partial x_j} \right)^2$$

We note that in a straight thin shear this form still gives essentially the same behaviour as the "standard" version since the omitted term makes a negligible contribution. For the strongly curved  $180^\circ$  bend, however, this model variant predicts major differences in the flow pattern (Figures 4 and 5) including, at  $90^\circ$ , large troughs in mean velocity near the inside of the bend qualitatively in line with experiment. Overall the computed flow pattern cannot be said to be in any better agreement with experiment than when the "standard" model was employed; nevertheless, the results did at least underline the sensitivity of the predicted flow to the turbulence model employed. Birch [3], in a parallel study employing a simple algebraically prescribed turbulence model, has drawn analogous conclusions.

In continuing work, Professor Choi (now returned to Korea University) is trying to obtain predictions to this flow using an algebraic stress model (ASM), a level of turbulence modelling which (while considerably more complex) is known to give more reliable predictions in complex flows than models based on the (isotropic) eddy viscosity concept.

Handwritten notes and a small table or form on the left margin. The notes include "Notes on file" and "H-1". The table has columns for "Codes" and "For".

Codes	For



### 3. Experimental Work - Circular-Sectioned 180° Bend

During the present contract year the construction and shake-down of the 180° bend apparatus has been completed, the heat-flux meters (which were at a prototype stage at the time of the last report) brought to their final stage of design development and a substantial series of experiments undertaken. Manuscripts have been prepared on both the design and functioning of the heat-flux meters and on the 180° bend test programme; these are included as Appendices 2 and 3 respectively.

As noted in last year's report, it did not appear feasible to provide a high-quality experiment with a uniform heat flux boundary condition. Accordingly, a uniform temperature rig was designed. Thus, the major instrumentation requirement was for an accurate heat-flux meter. The instrument which provided the basis for determining local values of Nusselt number in the U-bend is shown in Figure 6. A set of five such gauges set at 45° intervals around a section of straight pipe showed a reproducibility for any gauge within 2% in successive tests and a maximum variation among the five gauges of 5% (which is probably no more than the possible circumferential variation in Nu due to flow-field non-uniformities).

In the U-bend itself 25 such heat-flux meters were installed (five different circumferential angles at five stations) with a further five at a (movable) station downstream of the bend. They have proved mechanically robust and highly accurate; at a Reynolds number of  $1.1 \times 10^5$  deduced values of Nusselt number are estimated to be accurate within  $\pm 5\%$ . A mapping of both the heat-flux field and the associated temperature field within the air in the tube at the same stations was provided at a Reynolds number of about 60,000. This is close to that for which Azzola and Humphrey [4] have obtained laser-Doppler velocity measurements in an identically proportioned apparatus. Figure 7 shows the circumferential variation of Nusselt number measured at the six stations considered. By the 90° station (i.e. halfway around the U-bend) a 3:1 variation in Nu has developed between the outside and inside of the bend. There are two sources of this variation: it is due partly to the secondary flow depositing hot fluid on the inside of

the bend and partly to the augmentation of turbulence mixing near the outside of the bend and its damping near the inside that results from the different signs of the angular momentum gradient in the two cases. What initially seems curious is that six diameters downstream of the bend there is still a 2:1 variation in Nu despite the fact that the streamlines are now virtually straight and the secondary flow is very small. The reason turns out to be that the hot fluid that had accumulated on the inside of the bend further upstream simply stays in the same (circumferential) position depressing the rate of heat transfer.

In further work undertaken since the termination of the grant the corresponding distributions of Nusselt numbers at Reynolds numbers of  $1.1 \times 10^5$  and  $2.0 \times 10^4$  have been obtained; these data are also reported in Appendix 3. Future plans call for additional experiments with thin inlet boundary layers and cases of low Reynolds numbers ( $< 10^4$ ) where laminarization of the flow on the inside of the bend may occur.

#### 4. Computational Work

Last year's report described the toroidal-coordinate semi-elliptic procedure developed for analyzing flows in circular-sectioned bends. At that time it had been applied to laminar flows in  $180^\circ$  bends, ref. [5], and turbulent flow in  $90^\circ$  bends [6] employing, in the latter case, the standard  $k-\epsilon$  eddy-viscosity model in the main part of the flow and a mixing-length model in a thin annular ring adjacent to the pipe wall.

Subsequently, turbulent flow computations using precisely the same model were also made of the  $180^\circ$  bend flow being studied experimentally at UC Berkeley. The numerical calculations in fact preceded the experimental data, so when the latter became available there was some satisfaction at the encouraging degree of agreement. The manuscript on this work is included as Appendix 4. Figure 8, which is drawn from this paper, shows measured and computed profiles of the mean streamwise (primary) and circumferential (secondary) velocity at 11 stations and also the corresponding profile of the r.m.s. turbulent velocity profile.

The line along which the data are presented is the radial line bisecting the semi-circular cross section. While this turned out not to be a particularly interesting line so far as the primary velocity was concerned, the secondary profile shows an interesting reversal near the axis at  $135^\circ$ . The breakdown of the classical single cell that this reversal implies is clearly brought out in the computed secondary flow vectors and the corresponding streamwise velocity contours, Figure 9.

While the level of agreement obtained with the  $k \sim \epsilon$  model in circular-bend flows was satisfactory for many purposes, there was nevertheless room for improvement. Accordingly, much of the final year has been devoted to implementing a higher level turbulence model. While retaining the mixing-length model in the vicinity of the wall, in place of the  $k \sim \epsilon$  EVM we have incorporated an ASM version of the Gibson-Lauder [7] model for the Reynolds stresses (with minor adaptations to the model of pressure reflection from walls to accommodate the toroidal geometry) and for the heat fluxes the generalized gradient diffusion hypothesis:

$$-\overline{u_i \theta} = c_\theta \frac{k}{\epsilon} \overline{u_k u_i} \frac{\partial \theta}{\partial x_k}$$

An explanation of the nomenclature and further details are given in ref. [8] which appears as Appendix 5. The more elaborate model for the turbulent stresses brought in its train many difficulties in securing convergent behaviour. Very briefly, the practices that eventually proved most successful were:

- (i) the evaluation of the Reynolds stresses on a mesh staggered with respect to the velocity nodes as shown in Figure 10;
- (ii) the explicit evaluation of first the normal stresses then subsequently the shear stresses over any plane by essentially a Jacobi point-substitution approach. (Attempts at direct simultaneous solution of the stress matrix proved disastrous);

- (iii) the inclusion of parts of the stress terms in the momentum equations as effective viscosities in order to promote diagonal dominance of the difference equations and reduce the magnitude of the source terms;
- (iv) the treatment in the turbulence model of negative elements of the turbulent energy production rate as dissipation terms. (The somewhat arbitrary nature of this adjustment is mitigated by the fact that in the final converged solution this control is actually invoked at only a very small number of nodes. During progress to a converged field, however, the ASM scheme - unlike the eddy-viscosity model employed in our earlier work - can allow large negative generation to occur and entirely wreck what had seemed to be a smoothly converging solution).

Appendix 5 gives a more complete account of the above practices.

The code with the new model of turbulence incorporated has been applied to re-calculate the flow and heat transfer pattern in the 180° bend considered in the experimental part of the UCB-UMIST research. Extensive comparisons are drawn in ref. [8] which suggest some improvement in the flow field predictions results. Figure 11 shows the computed local Nusselt number distribution at several stations around the U-bend compared with the experimental results discussed in Section 2. We see that generally the augmentation of Nu on the outside of the bend and its damping on the inside is captured better by the ASM model than with the  $k \sim \epsilon$  EVM. However, at 90° and 135° the predicted level of Nusselt number on the outside of the bend is still moderately below the measured levels. Recently repeated experiments at the same Reynolds number suggest that levels of Nu near the outside of the bend measured in the first test (which are those shown in Figure 11) may be too high by 6-8%. Moreover, the neglect of density changes in the computations would, it is estimated, lead to an underestimate of Nu by some 3%. Thus, about one half the discrepancy between the ASM predictions and the data can be attributed to factors other than shortcomings in the turbulence

model.

##### 5. Achievements and Overall Conclusions

The research programme now concluded had set out to establish how well current three-dimensional flow solvers could predict heat transfer behaviour in a complex internal flow typical of convective heat-exchanger situations. In order to make the assessment, an extensive data base had to be acquired, for measurements of the required level of detail, including flow and heat transfer data for the same configurations, simply did not exist.

So far as that data base is concerned, we believe that, in conjunction with the flow field and turbulence data gathered by Professor Humphrey and his team at Berkeley, a satisfactory set of experimental results has been generated. The design of heat-flux meter developed in the experimental research may also be useful to others embarking on constant-wall-temperature experiments.

A more complicated picture is presented on the computational front. For the circular-sectioned bend, rather satisfactory agreement has been obtained especially with the algebraic stress model of turbulence. The agreement is sufficiently good that one could with confidence use computer modelling to optimize designs (excluding the low-Reynolds-number regime ( $Re < 1.5 \times 10^4$ ) which has not been explored in the present work).

For the square bend, a quite different picture emerges. While, with the adoption of PSL and the low-Re near-wall modelling, the first  $45^\circ$  of development is well accounted for with the  $k\sim\epsilon$  model, there remains a serious disagreement with the measured velocity profiles at  $90^\circ$  and, to a diminishing extent, stations downstream therefrom. Our computations have at least shown that numerical errors are not responsible for the difference and that the predicted flow pattern is highly sensitive to the form of the dissipation rate equation used.

Although the equations look less complicated for the square-

Although the equations look less complicated for the square- than the round-sectioned bend, the former is undoubtedly a much more complicated flow both physically and numerically. Work is continuing at UMIST on this flow sponsored by the NASA Lewis Laboratories and we shortly hope to be able to report fully-converged ASM results for this case. Until such predictions are available, it is hard to say whether the square-sectioned bend is just a difficult flow or whether it is a pathological case. As a tailpiece, Professor Humphrey (personal communication) has observed that the differences between observation and experiment could be explicable in terms of the flow being unsteady, "sloshing" back and forth about the plane of geometric symmetry.

#### Acknowledgements

The completion of this five-year programme of research under US ONR sponsorship has been possible only with outstanding technical cooperation at different levels by many individuals. First must be mentioned the multi-faceted help and stimulus provided by Professor J.A.C. Humphrey and his research group at the University of California, Berkeley (Dr. T.Y. Han, Dr. S.M. Chang and Dr. W.M. To), both in carrying out their complementary research programme and providing helpful input to ours. Professor J.W. Baughn of the University of California, Davis, who paid four visits to UMIST, made a major contribution to the whole experimental programme; his infectious enthusiasm has also rubbed off on the UMIST scientific and technical staff supporting the effort. Here special mention should be made of the contributions of Mr. D. Cooper who developed both the square- and circular-sectioned U-bends and Mr. R. Lever for his exceptional machining skills. These two won jointly the UMIST 1984 Award for Non-Academic Staff in recognition of their outstanding engineering skills in fabricating the circular-sectioned bend and the associated heat-flux meters. Our appreciation goes to all the technical staff, each of whom has made a contribution to the project. Our thanks especially go to Mr. A. Prunty who built the power control circuits for the square bend; Mr. D.W. Chadwick for help and stimulating discussion on the automatic control of the heat-flux meters; Mr. D.C. Jackson, Senior Experimental Officer at UMIST, for considerable help in the organization and performance of the tests; and Mr. W.H. Jackson who, as Workshop Superintendent, coordinated the efforts of his technical staff and arranged purchasing.

All the computations were performed on computing equipment at the University of Manchester Regional Computer Centre. Special thanks go to John Nicholson, local computer supervisor, for his efforts in trying to get the best from the system during a period of inadequate resource and malfunctioning hardware.

References

1. Johnson, R.W. "Turbulent convecting flow in a square duct with a 180° bend: An experimental and numerical study." PhD Thesis, Faculty of Technology, University of Manchester, 1984.
2. Iacovides, H. and Launder, B.E. J. Fluids Engrg. 106, 241, 1984.
3. Birch, N. "The calculation of 3D flow in curved ducts using Q385." Rep. TSG0161 Rolls-Royce Derby, 1984.
4. Azzola, J. and Humphrey, J.A.C. "Developing turbulent flow in a 180° curved pipe and its downstream tangent." Rep. LBL-17681 Lawrence Berkeley Laboratories, Materials Science and Molecular Research Div., LBL, 1984 (see also Proc. 2nd International Symposium on Applications of Laser Anemometry to Fluid Mechanics, Lisbon, Portugal, 1984).
5. Humphrey, J.A.C., Iacovides, H. and Launder, B.E. J. Fluid Mech. 154, 357, 1985.
6. Iacovides, H. and Launder, B.E. Proc. 1st UK National Heat Transfer Conf., I. Chem. E. Symp. Series 86, Paper 17.4, 1097, 1984.
7. Gibson, M.M. and Launder, B.E. J. Fluid Mech. 86, 491, 1978.
8. Iacovides, H. and Launder, B.E. Proc. 4th Conf. on Numerical Methods in Laminar and Turbulent Flow, Vol. 2, 1023, Pineridge Press, Swansea, 1985.

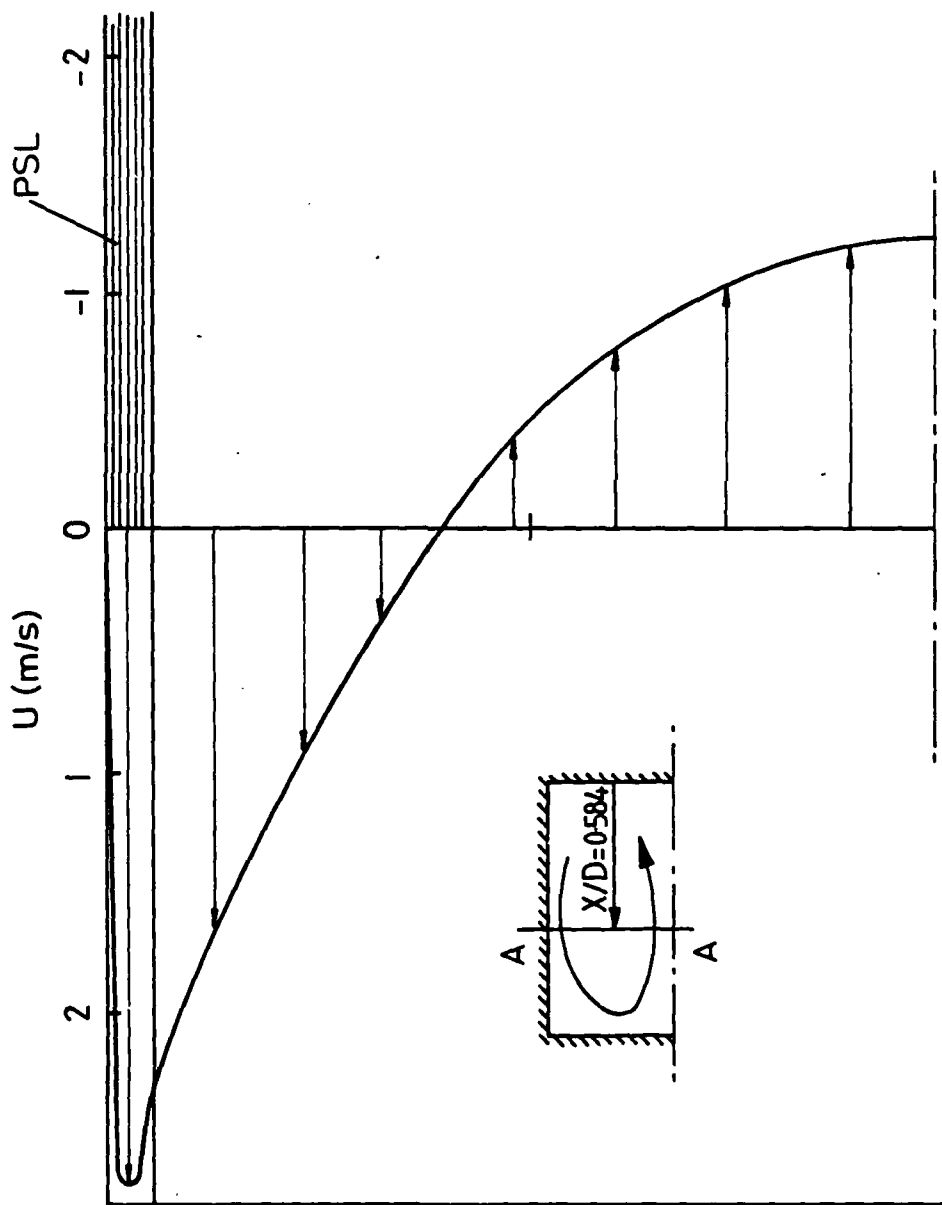


Figure 1 Computed profile of secondary velocity at 90° into square bend

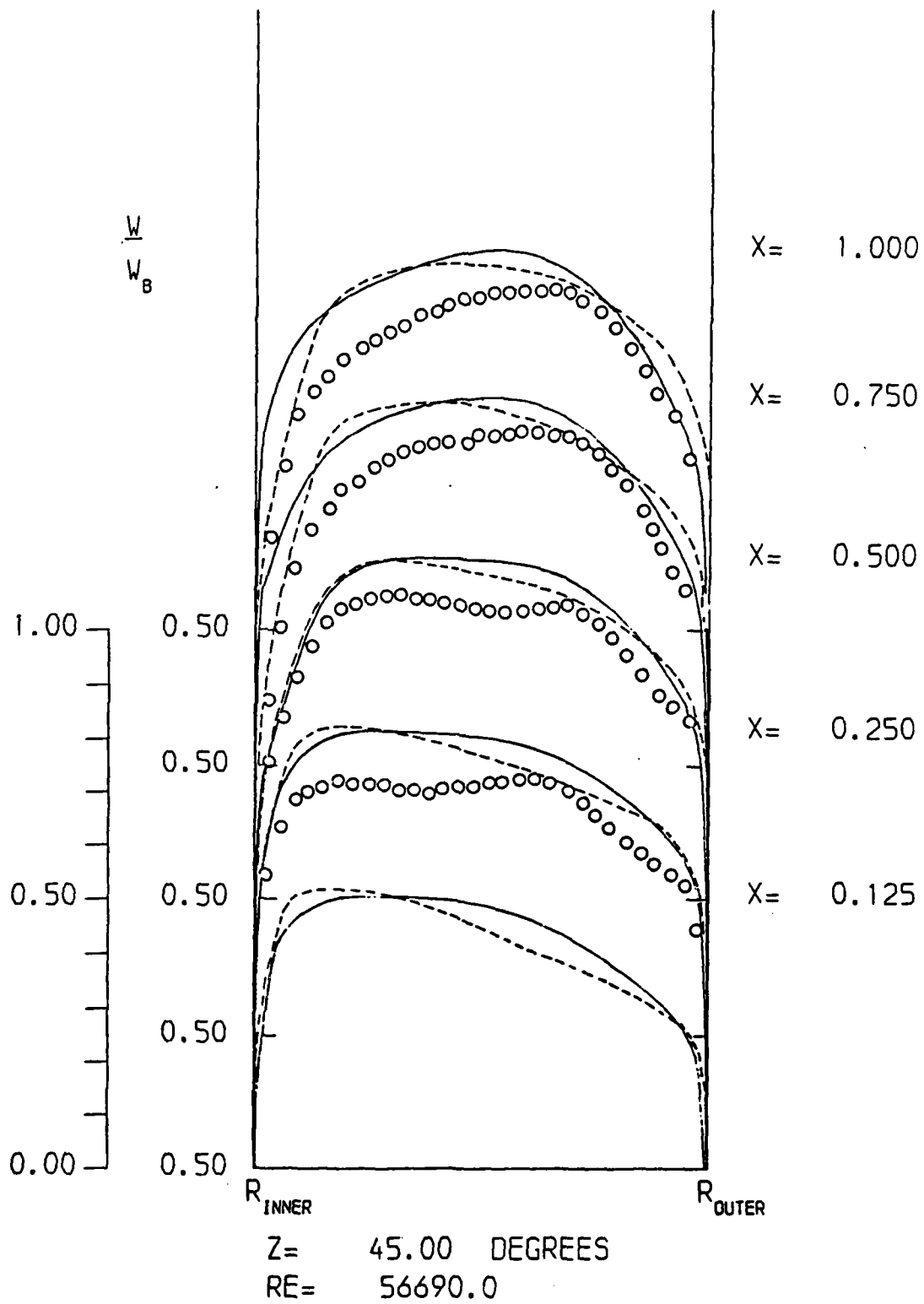


Figure 2 Effects of PSL on velocity profiles at  $45^\circ$

----- computations with wall functions [1]  
 \_\_\_\_\_ PSL computations, Choi

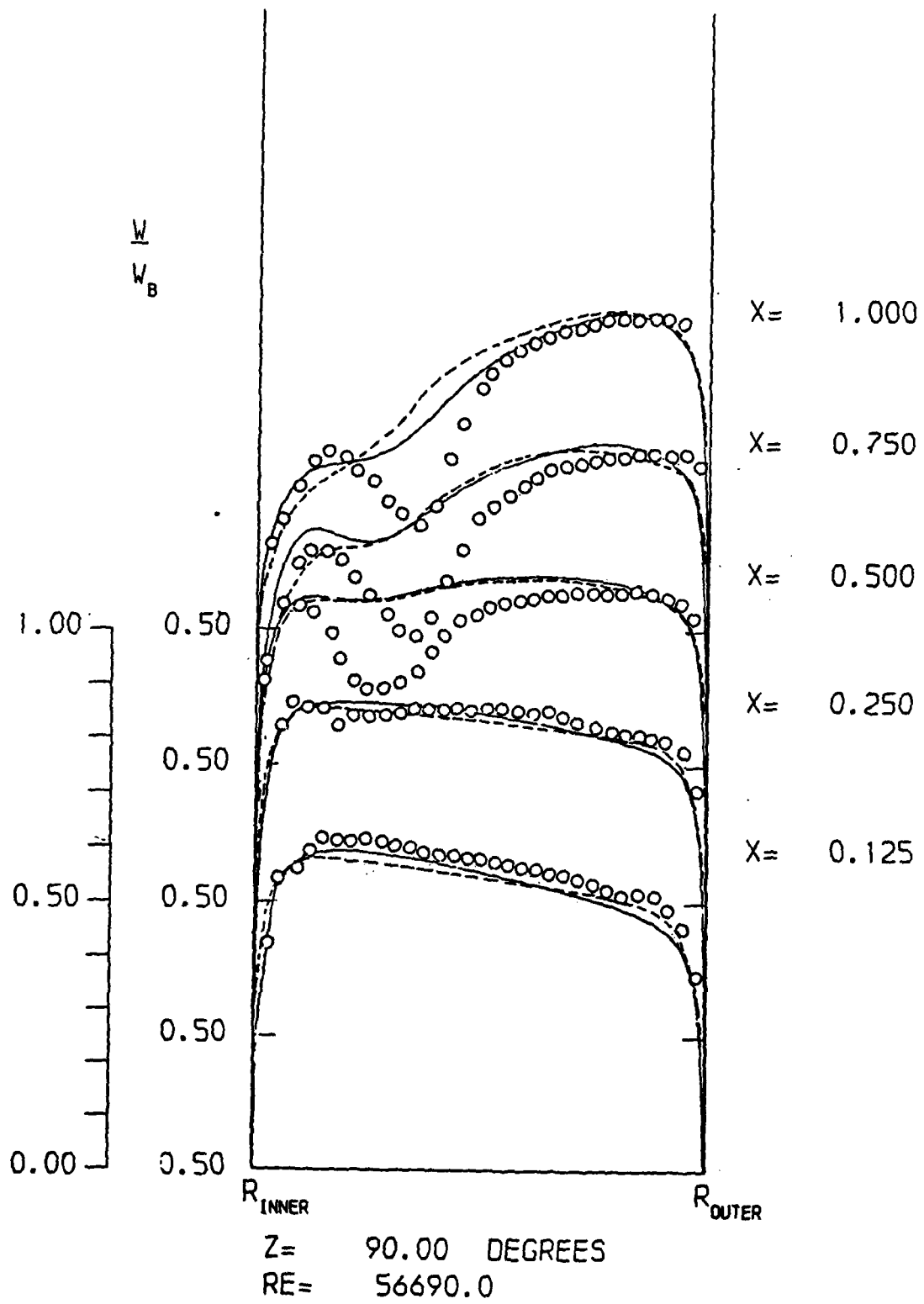


Figure 3 Effects of PSL on velocity profiles at  $90^\circ$

Key: as Figure 2

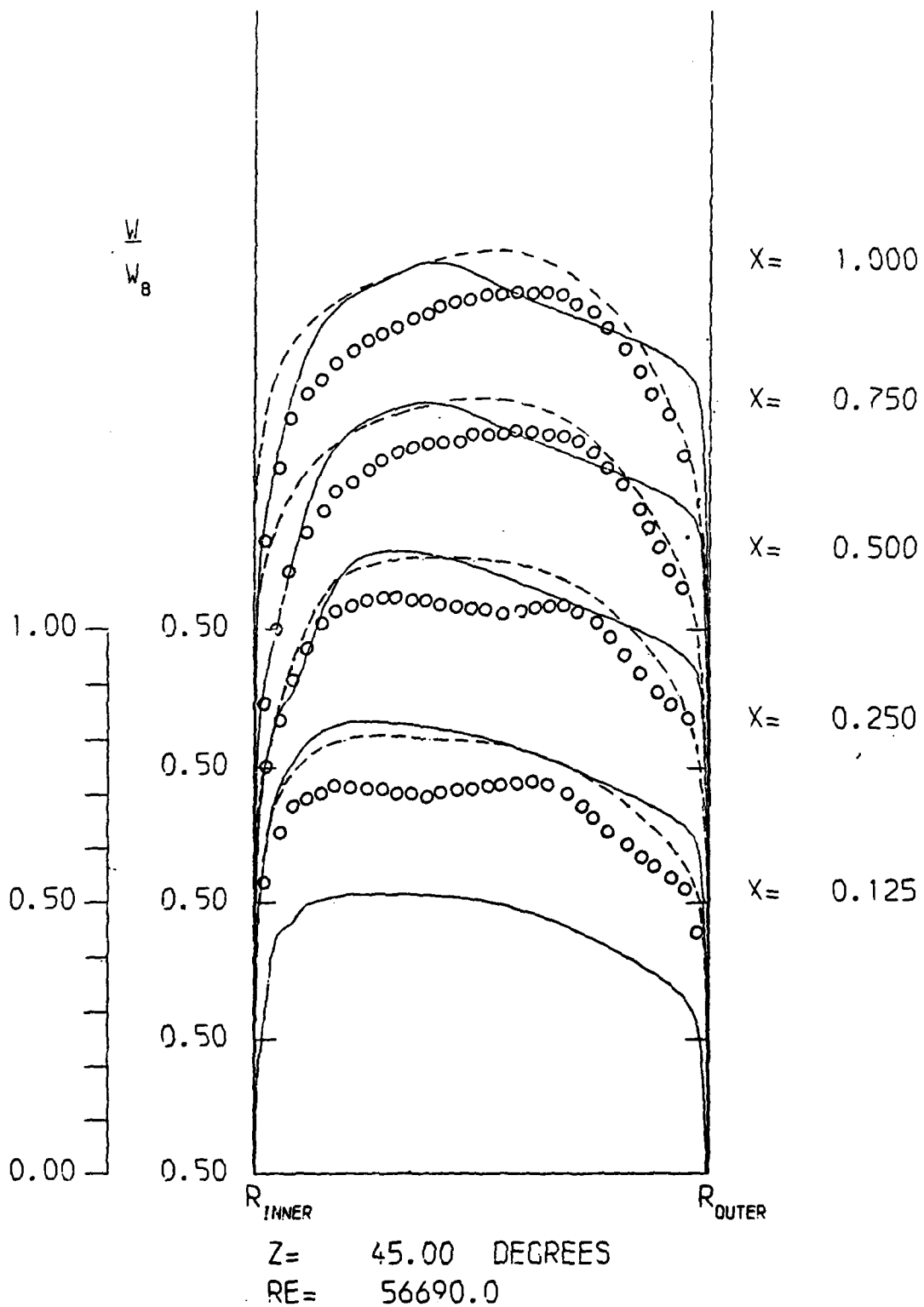


Figure 4 Effects of modifying  $\epsilon$  source on streamwise velocity profiles at  $45^\circ$

Modified source, eq(1) ———  
 Standard source - - - - -

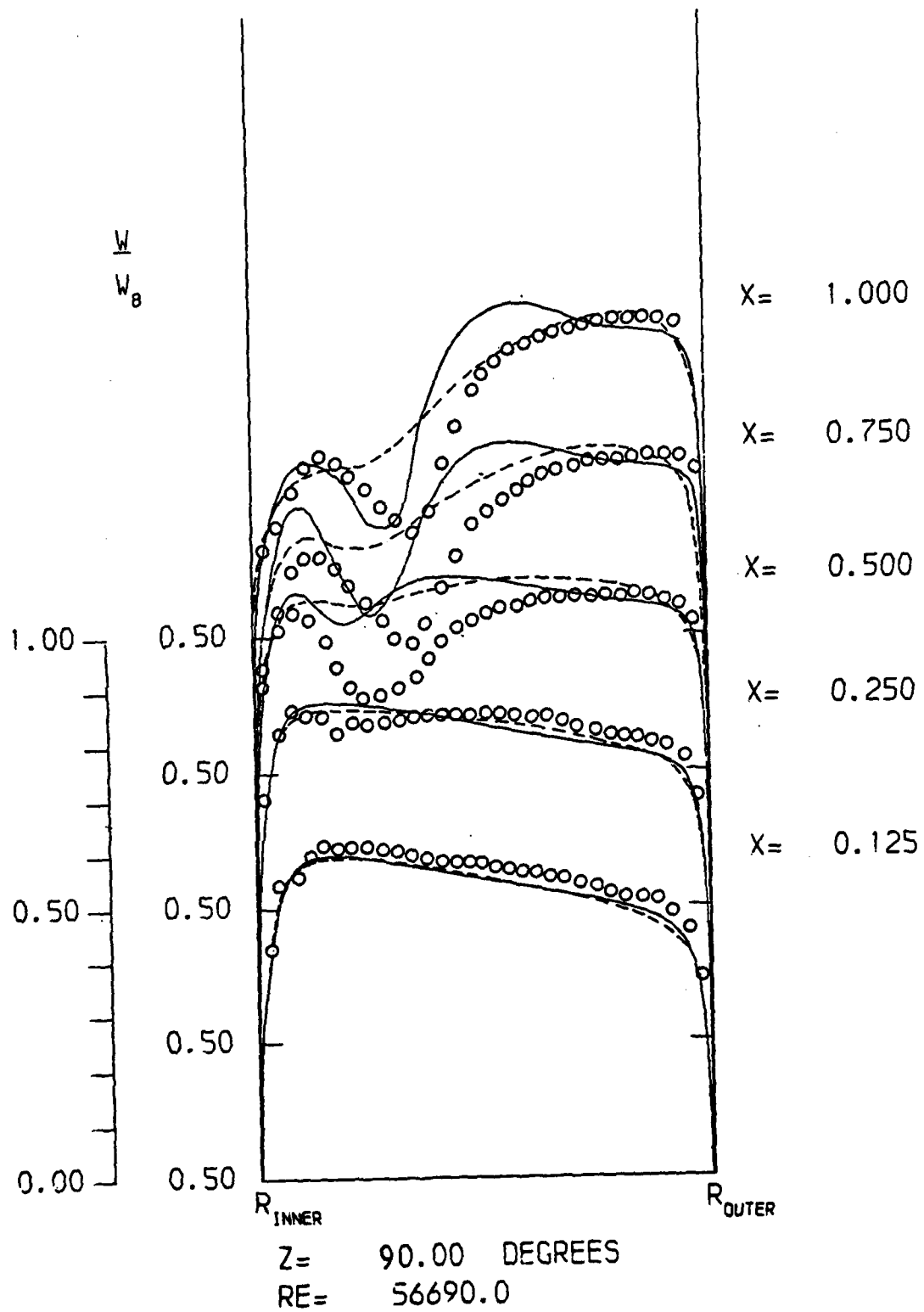


Figure 5 Effects of modifying  $\epsilon$  source on streamwise velocity profiles at  $90^\circ$

Key: as Figure 4

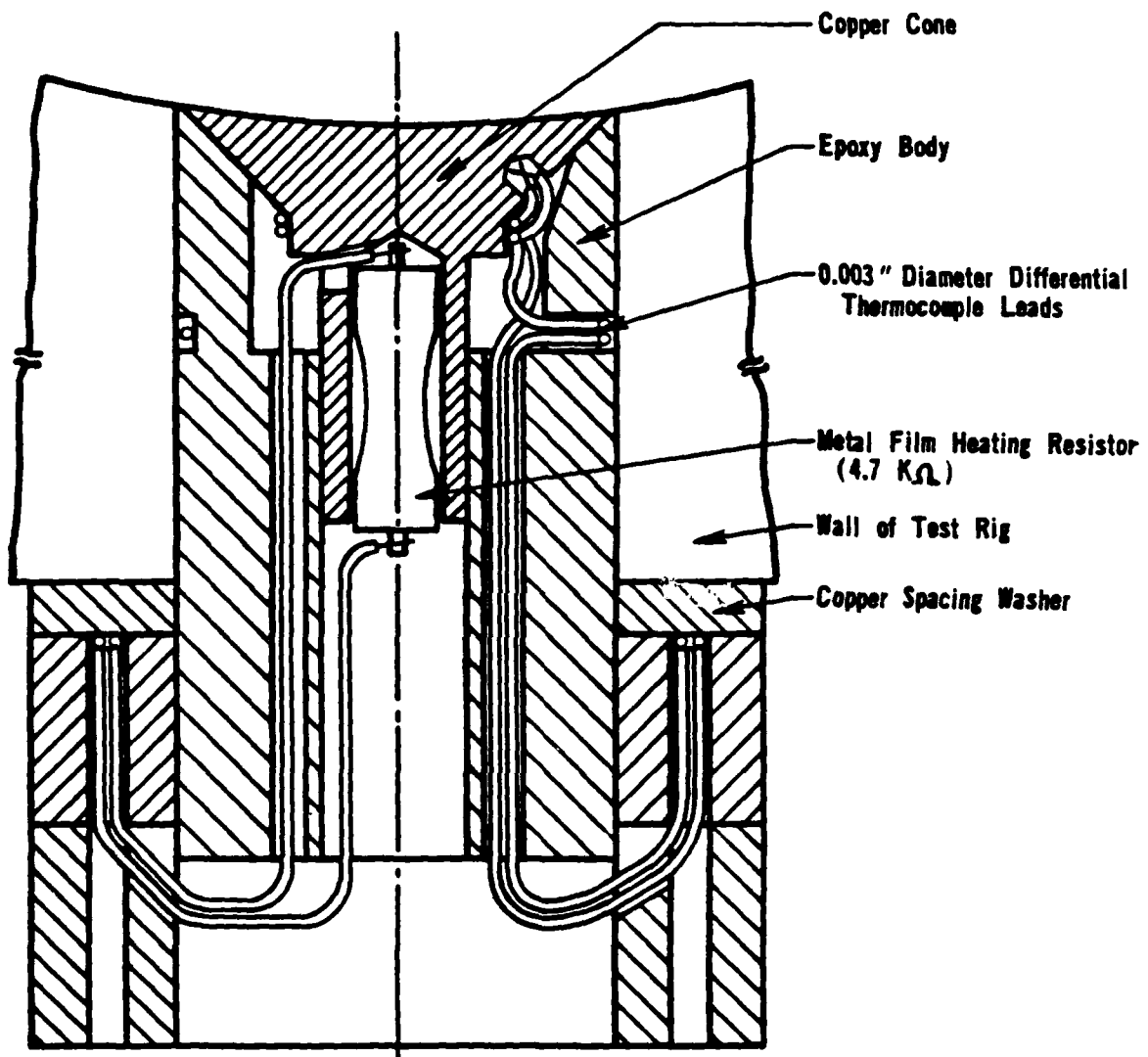


Figure 6 Cross-sectional view of heat-flux meter

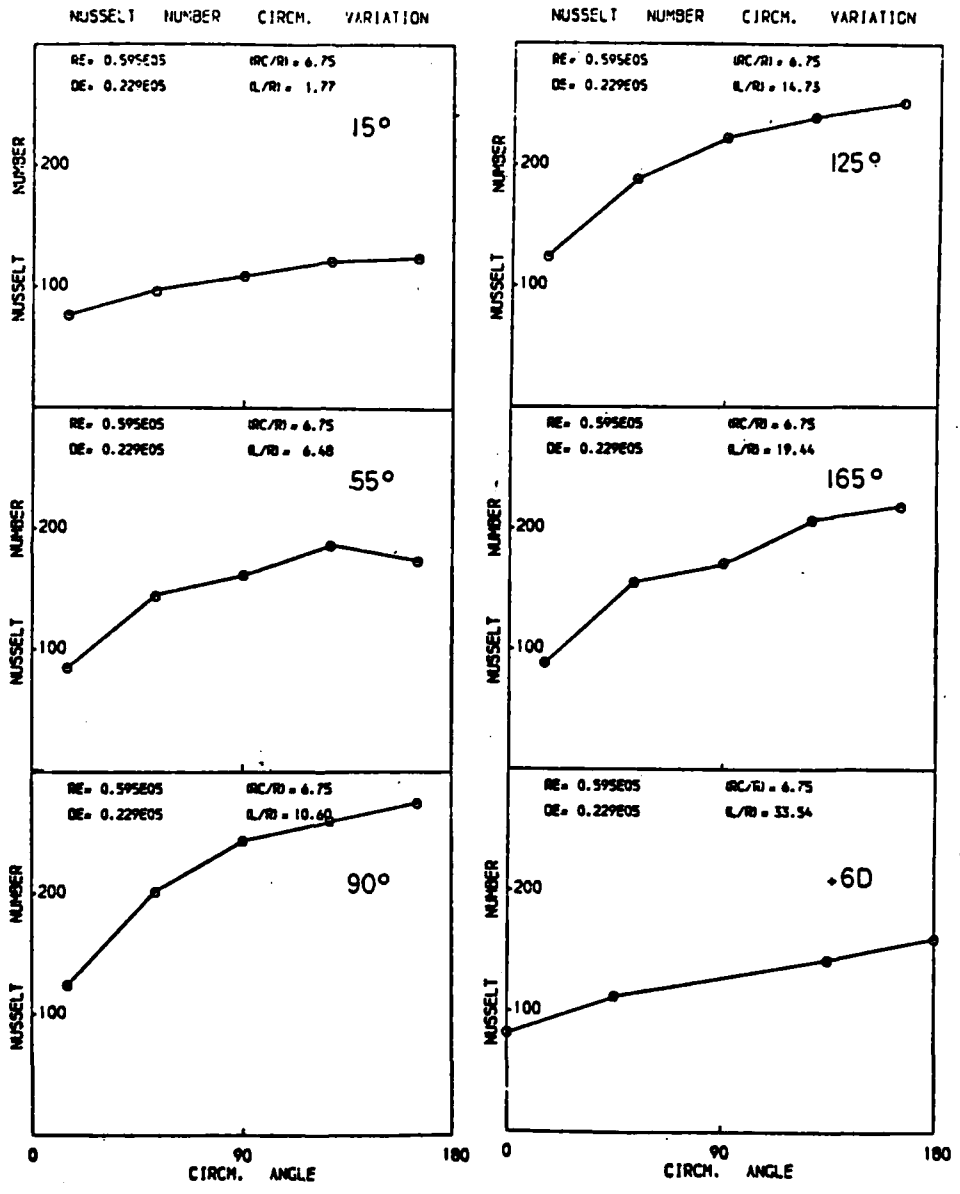


Figure 7 Measured circumferential variation of Nusselt number at six streamwise positions

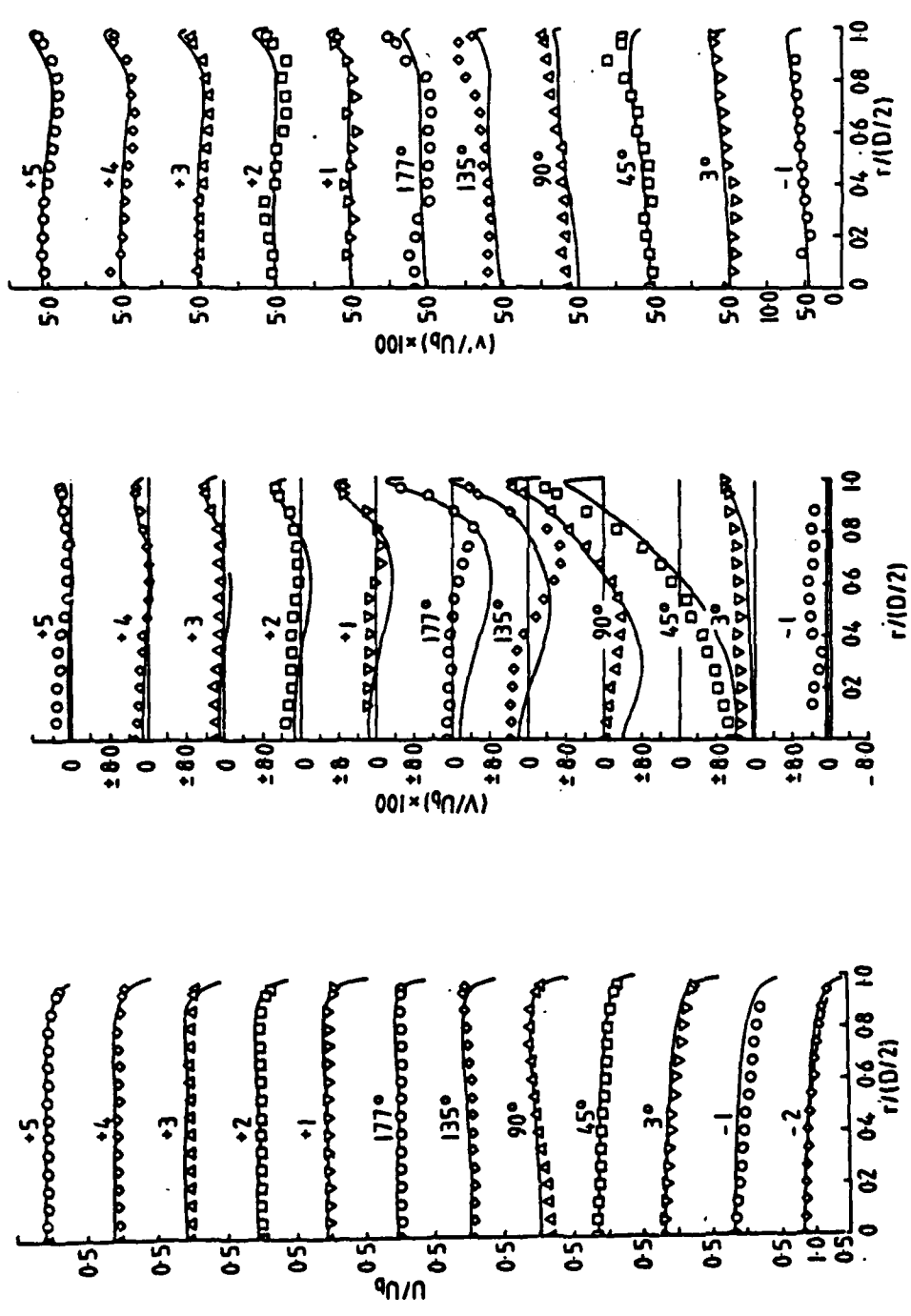
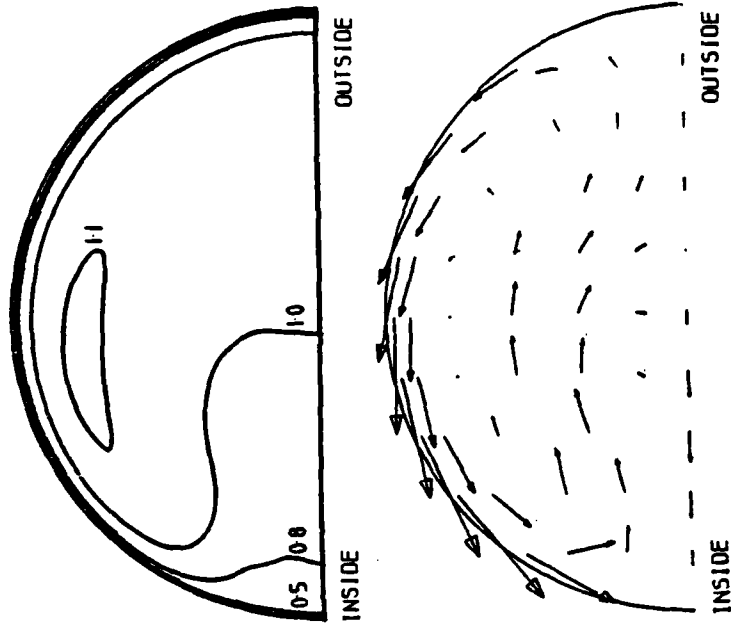
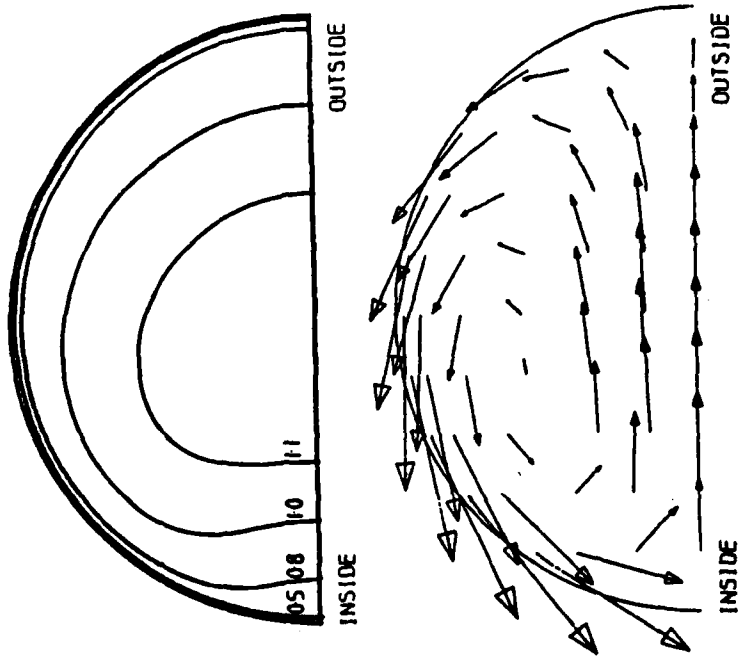


Figure 8 Measured and computed velocity profiles along radial line orthogonal to symmetry plane of 180° circular sectioned bend; k-ε EVM  
 U : streamwise velocity; V : circumferential velocity;  
 v' : rms circumferential turbulent velocity  
 (See Appendix 4 for complete comparison)



(L/R) = 15.91 ;  $\theta = 135^\circ$



(L/R) = 5.30 ;  $\theta = 45^\circ$

Figure 9 Cross-sectional distribution of velocity components at  $45^\circ$  and  $135^\circ$

Top : streamwise velocity contours

Bottom : secondary velocity vectors

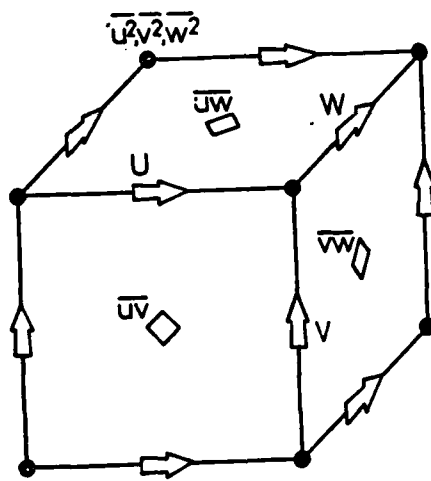


Figure 10 Staggered mesh for Reynolds stresses and mean velocities

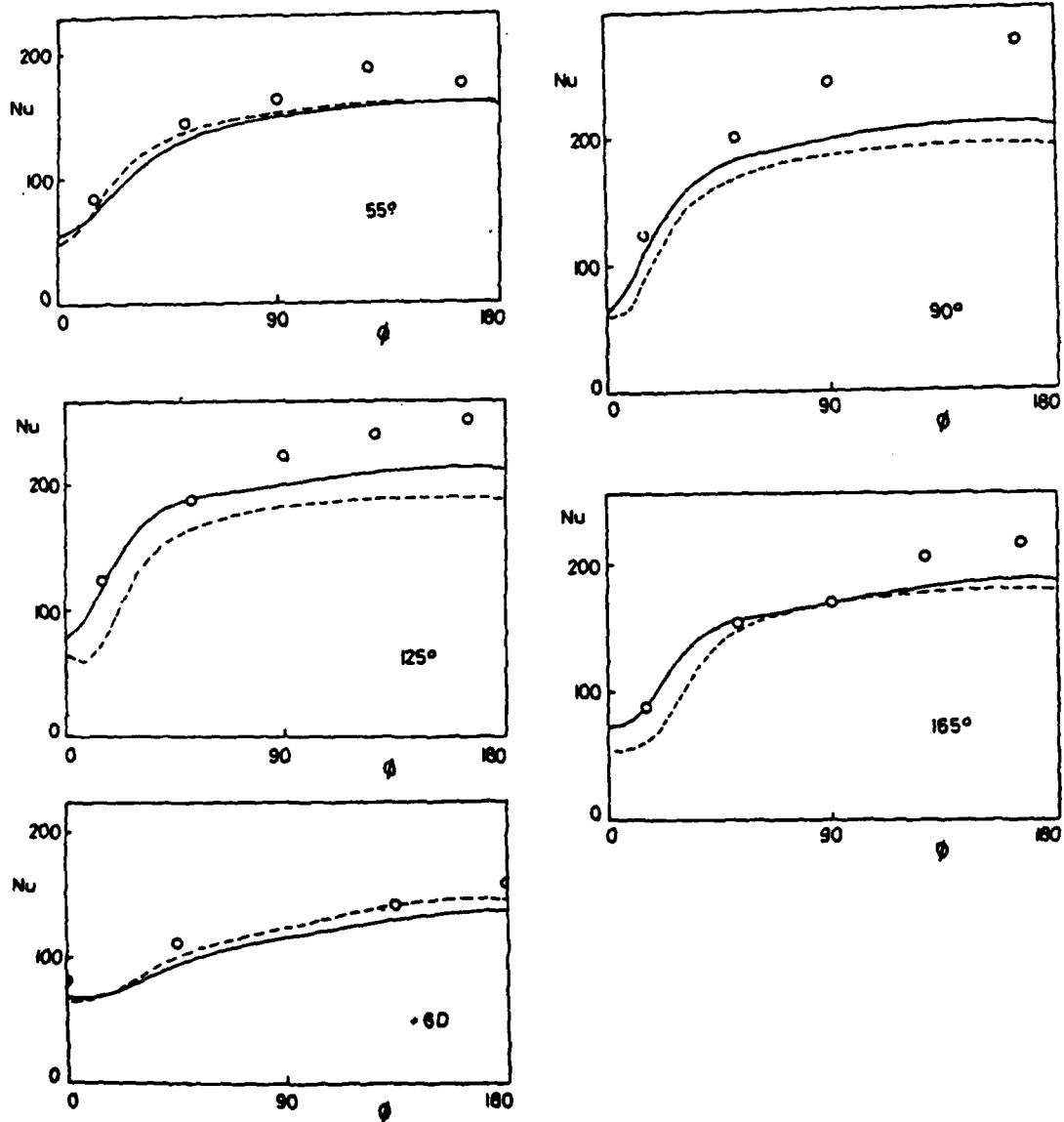


Figure 11 Predicted variation of Nusselt number around 180° bend

---  $k-\epsilon$  EVM  
 — ASM

APPENDICES

Publications and Theses arising from Project

1. R.W. Johnson and B.E. Launder "Discussion of 'On the calculation of turbulent heat transport downstream from an abrupt pipe expansion'", Numerical Heat Transfer 5, 493-496, 1982.
2. S.M. Chang, J.A.C. Humphrey, R.W. Johnson and B.E. Launder "Turbulent momentum and heat transport in flow through a 180° bend of square cross section." Proc. 4th Turbulent Shear Flows Symposium, University of Karlsruhe, pp.6.20-6.25, 1983.
3. R.W. Johnson "Turbulent convecting flow in a square duct with a 180° bend." PhD Thesis, Faculty of Technology, University of Manchester, 1984.
4. R.W. Johnson and B.E. Launder "Local heat transfer behaviour in turbulent flow around a 180° bend of square cross section." ASME Paper 85-GT-68, 30th International Gas Turbine Conference and Exhibit, Houston, 1985.
5. R.W. Johnson and B.E. Launder "Local Nusselt number and temperature field in turbulent flow through a heated square sectioned U-bend." Int. J. Heat and Fluid Flow 5, September 1985.
6. H. Iacovides and B.E. Launder "PSL - An economical approach to the numerical analysis of near-wall elliptic flows." ASME J. Fluids Engrg. 106, 245, 1984.
7. H. Iacovides and B.E. Launder "The computation of momentum and heat transport in turbulent flow around pipe bends." Proc. 1st UK National Heat Transfer Conference, Vol. 2, I. Chem. Engrs. Symp. Series 86, 1984.
8. J.A.C. Humphrey, H. Iacovides and B.E. Launder "Some numerical experiments on developing laminar flow in circular sectioned bends." J. Fluid Mech. 154, 357, 1985.
9. J. Azzola, J.A.C. Humphrey, H. Iacovides and B.E. Launder "Developing turbulent flow in a U-bend of circular cross section : Measurement and computation." Accepted for publication in ASME J. Fluids Engrg., 1986.
10. H. Iacovides and B.E. Launder "ASM predictions of turbulent momentum and heat transfer in coils and U-bends." Proc. 4th Int. Conf. on Numerical Methods in Laminar and Turbulent Flow, 1023-1045, Pineridge Press, Swansea, 1985.
11. J.W. Baughn, D. Cooper, H. Iacovides and D.C. Jackson "An instrument for the measurement of heat flux from a surface with uniform temperature." Submitted to Review of Scientific Instruments, August 1985.

12. J.W. Baughn, H. Iacovides, D.C. Jackson and B.E. Launder  
"Local heat transfer measurements in turbulent flow around  
a 180° pipe bend." Submitted to ASME 31st International  
Gas Turbine Conference, Dusseldorf, 1986.
13. H. Iacovides "Momentum and heat transport in flow through  
180° bends of circular cross section." PhD Thesis,  
Faculty of Technology, University of Manchester, 1985.

UNIVERSITY OF MANCHESTER INSTITUTE OF SCIENCE AND TECHNOLOGY

Department of Mechanical Engineering

AN INSTRUMENT FOR THE MEASUREMENT OF HEAT FLUX  
FROM A SURFACE WITH UNIFORM TEMPERATURE

by

J.W. Baughn\*, D. Cooper, H. Iacovides and D.C. Jackson

\* University of California, Davis

August 1985

TFD/85/4

## ABSTRACT

An instrument for the measurement of heat flux from a surface with a nearly uniform temperature is described. This instrument contains a thin film electrical resistance heater imbedded in a copper cone which is thermally isolated from the surrounding walls. A differential thermocouple between the copper cone and the wall is nulled such that the electrical power becomes a direct measure of the surface heat flux. This instrument is modular and can be flush mounted in an external surface or mounted in the wall of a duct. It provides high accuracy and has been used to measure the heat transfer coefficients inside a circular duct. For these measurements an uncertainty analysis is presented which shows that this instrument has an uncertainty of  $\pm 3.6$  percent for a convective heat flux of 342 W/sq. m. The major source of uncertainty was the surface area. With improvements in the surface area measurement the uncertainty would be approximately  $\pm 2$  percent.

## INTRODUCTION

In studies of convective and radiative heat transfer, it is necessary to determine both the wall temperature and the heat flux from a surface. If these measurements are to be useful, the thermal boundary conditions must be known. There are two common thermal boundary conditions. In the first boundary condition the surface heat flux is uniform. This is often accomplished by electrically heating the wall. In order to determine the heat transfer coefficient under this condition the temperature distribution is measured with local sensors. The other important and commonly used boundary condition is a uniform wall temperature. In this case the local heat flux is measured with a local heat flux gage.

Emrich (1), in a recent review of heat flux gages, suggests that local heat flux gage designs are based on three different conceptual methods of measuring heat flux: 1. the heat flux may set up a temperature gradient—the gradient method; 2. the heat flux may cause a temperature transient in a calorimeter—the transient method; 3. The heat flux may be balanced against a calibrated heat removal—the balance method. There are many different heat flux gage designs based on these conceptual methods (2, 3, and 4). Unfortunately, most of these designs do not provide a uniform wall temperature since they are based on methods 1 and 2 and require either a temperature gradient or temperature transient to provide the sensing input. For

example, the Gardon or Asymptotic (thin circular foil) heat flux meter uses the temperature difference between the center and edge of a surface mounted disc as the sensing input (5 and 6) which results in a temperature distribution on the surface (method 1-gradient). This gradient in the surface temperature may change (perturb) the surface heat flux from that which would occur in the absence of the sensor. This has been studied extensively for the case of convective heat transfer (6-9). Another type of heat flux gage using method 1, the wafer-type meter (10), senses the temperature gradient through a layer (wafer) on a surface as a measure of the heat flux. This changes the local surface temperature from what it would be in the absence of the sensor and thereby may change the local heat flux. Thermopile sensors (using differential thermocouples) may be fabricated with different geometries and be similar to either the asymptotic or wafer-type meters.

A heat flux gage which uses method 2 (transient) is the slug-type heat flux meter. The slug-type has a thermally isolated mass and measures its temperature response to determine the heat flux. This changing surface temperature boundary condition may also influence the local heat flux (7). Another example of the transient method (method 2) is the thin-film heat flux sensor which uses a surface temperature transient to infer the heat flux (11). These latter types of sensors are often used in shock tunnels with high temperatures and short flow periods. Under these

specialized conditions the small initial temperature rise of the surface may not significantly perturb the local heat flux.

As noted, each of the above instruments perturbs the surface temperature while measuring the surface heat flux which may in turn perturb the surface heat flux. In convective heat transfer, this perturbation may persist downstream of the sensor (e.g., during the development of a thermal boundary layer).

The instrument described in reference 12 (which is similar in concept to that used in reference 13) is based on method 3 (the balance method) and is designed to provide a nearly uniform surface temperature. In this heat flux gage a thermally isolated but highly conducting mass (e.g., a copper cone) is mounted in a wall and electrically heated to the surrounding surface temperature. The differential temperature between the mass and the wall is measured and the power is adjusted until this difference is reduced to zero (i.e., nulled) and the null electrical power is then used to infer the heat flux.

In this paper, an instrument which operates on the same principle as that of reference 12, but with several important improvements, is described. This new instrument is modular in design, making it far easier to fabricate. It uses a thin-film resistor heater not previously used in this type of sensor and unlike the earlier instrument designs

based on this method, it can also be installed and removed from a wall so as to measure the heat flux on an exterior or an interior surface (i. e. inside a duct).

#### DESIGN OF THE HEAT FLUX SENSOR

A sectional diagram of the heat flux sensor is shown in figure 1 and a photograph of the sensor and its components is shown in figure 2. The sensor is designed to fit into the wall of a test rig as shown in this figure. The face of the sensor (top of figure 1) can be inside a duct or on an outside surface. The main element of the sensor consists of a small copper cone with a cylindrical extension. This copper cone has an imbedded differential thermocouple to measure its temperature relative to the wall of the test rig and it has a heating resistor to heat the cone and balance the surface heat flux. The copper cone is cemented into an epoxy cylinder which has been drilled and machined to fit the cone. The epoxy cylinder fits into the wall of the test apparatus or surface of interest. This epoxy cylinder has an outside diameter of 12 mm and has a small groove machined around the outside circumference with a small access hole for the differential thermocouple leads (see figure 1).

The differential thermocouple consists of EP-EN-EP (Chromel-Constantan-Chromel) Teflon-covered wires (AWG No. 40: 0.076 mm/0.003 in. diameter) which provide an output of approximately 59 microvolts per degree C. The EP wire enters from the back of the instrument and is then wound

around the conical surface before it is imbedded in the side of the conical surface where it makes a junction with the EN wire. The EN wire continues the circuit and is also wound around the cone before it goes through the small hole in the epoxy cylinder and then around to the opposite side of the epoxy cylinder where a junction with the final EP wire is made. This final EP wire continues the circuit around inside the groove and enters the same small side hole and exits through the back side of the sensor. This arrangement considerably reduces conduction between the cone and outside surface along the wires. It also ensures good thermal contact between the outside junction and the wall since there is a large contact area. Silver loaded epoxy is loaded into the outer groove to further ensure that the outside junction region of the differential thermocouple is at the wall temperature. The differential thermocouple leads (EP,EP) go to a data logger where they are connected directly to an isothermal connecting block. This is shown in the wiring diagram of figure 3. In order to protect these delicate wires from mechanical damage and electrical interference, a copper screening braid is passed over the wires and anchored securely to the sensor cylinder with a silver steel pin. The data logger that is used to monitor the signal from the differential thermocouple has a resolution of 1.0 microvolt.

The heater which is inserted into the copper cone (cylindrical extension) is a high stability metal film heating resistor with a resistance of 4.7 Kohms and an outside diameter of 2.4 mm. The active resistance part of this resistor is a thin film on the surface of a ceramic rod. This has good thermal contact with the copper cone since the resistor is cemented into the interior of the cylindrical extension using silver loaded epoxy. The electrical connections to this resistor are made with Teflon coated constantan wire (AWG No. 40: 0.076 mm/0.003 inch diameter) and the ends are coated with epoxy to avoid electrical contact with the copper cone. Four wires (two on each end) are used to eliminate lead wire resistance effect (i. e., two wires carry the current and two wires are used for the voltage measurement). In order to minimize conduction losses along these wires, they are routed so that they first emerge from the sensor body directly under a copper spacer washer and in good thermal contact with it before being fed through a suitable hole to emerge from the rear of the sensor. These fine wires are then connected to four terminal posts secured on the back of the sensor where larger lead wires (0.56 mm/0.022 in.) are taken to the power supply and measurement instrumentation. The wiring diagram for the sensor given in figure 3 shows the power supply and measurement arrangement.

#### SENSOR OPERATION AND UNCERTAINTY ANALYSIS

Following the approach adopted by Kraabel (12) we begin with an energy balance equation for the copper cone of the heat flux sensor.

Heat Transfer Rate = Heat Transfer Rate + Heat Conduction  
into the Cone from surface from the Cone

$$\begin{array}{ccc} \text{(a)} & & \text{(b)} & & \text{(c)} \\ P_s & = & q_s & + & q_c \quad (1) \end{array}$$

The three terms in the above balance equation can be expressed individually as

$$\text{(a)} \quad P_s = E_{RH} I_{RH} + I_{RH}^2 R_{LW} = \frac{E_{RS}}{R_{RS}} \left( E_{RH} + \frac{E_{RS} R_{LW}}{R_{RS}} \right) \quad (2)$$

$$\text{(b)} \quad q_s = q_s'' A_s \quad (3)$$

$$\text{(c)} \quad q_c = C_e (T_s - T_w) \quad (4)$$

The sensor electrical input power is put in terms of the sensor voltage, shunt voltage and resistance, and a lead wire resistance. The lead wire resistance is only that portion of the lead wire in which the ohmic heating is transferred by conduction to the sensor cone. It is negligible in this case since it is much smaller than the heater resistance of 4.7 Kohms. It is included here for the uncertainty analysis.

The parameter  $C_e$  is the overall thermal conductance between the copper cone of the sensor and the surrounding wall. Its value can be determined experimentally by insulating the surface face of the sensor and applying power to the heater resistor. This has been done and the results are shown in figure 4. The linearity of these results suggests that under these conditions the losses from the copper cone are primarily conduction and that the use of  $C_e$  is an appropriate model. The value of  $C_e$  can be found from the slope of this curve and is 25.7 mW/K.

Equations 1-4 can be combined to obtain an expression for the heat flux in terms of the various measurands.

$$q_s'' = \frac{1}{A_s} \left[ \frac{E_{RS}}{R_{RS}} \left( E_{RH} + \frac{E_{RS}}{R_{RS}} \cdot R_{ew} \right) - C_e (T_s - T_w) \right] \quad (5)$$

This expression can be used to determine the individual contributions of each measurand and the total uncertainty in the measured heat flux. Following standard procedure (see reference 2) the uncertainty due to each individual measurand is given by

$$\delta q_{s,i}'' = \frac{\partial q_s''}{\partial x_i} \delta x_i \quad (6)$$

where  $x_i$  is the particular measurand and  $\delta x_i$  is the uncertainty in that measurand. The total uncertainty is then given by

$$\delta q_s'' = \sqrt{\sum_{i=1}^n [\delta q_{s,i}']^2} \quad (7)$$

The estimated uncertainties in each measurand, their individual contribution, and the total uncertainty is shown in Table I for one set of measurements in the application described below. These estimates are based on 20:1 odds. For a measurement of 342 W/ sq. m. the uncertainty was found to be +/-3.6 percent. The major source of uncertainty was the surface area. With improvements in the surface area measurement the uncertainty would be approximately +/-2 percent.

#### APPLICATION AND MEASUREMENT

Although this sensor can be applied to many interesting convective heat transfer measurements, it was developed specifically to study convective heat transfer in pipes with bends (i.e., a curved circular duct). In this application, the face of the sensor is machined with curvature in two planes, which is not possible with most other heat flux sensors.

In order to test the performance of the sensor, it was first used to measure heat flux rates in a straight pipe with fully developed turbulent flow and with a uniform wall temperature. This case was selected because it has been extensively studied and established correlations exist for the heat transfer under these conditions.

The test section consisted of an externally heated thick walled aluminum pipe with an internal diameter of 7.6 cm (3.0 in.). Five sensors were installed in the pipe at equally spaced positions around the top half circumference at a position approximately 42 diameters downstream in the heated section. The velocity and temperature profiles at this position were determined with a traverse probe. This provided a measurement of the local bulk temperature. The flow rate was determined using an orifice plate (constructed according to British Standard 1042) located far downstream of the test position. To ensure fully developed flow conditions, there was an additional 36 diameters of unheated pipe upstream of the heated section.

After the axisymmetry of the velocity and temperature fields in the pipe are established, a series of three tests were made at three different Reynolds numbers. The heat flux and corresponding Nusselt number was then calculated for each sensor as shown in Table II. The Nusselt number is given by

$$Nu = \frac{hD}{k} = \frac{q_s'' D}{(T_s - T_B) k} \quad (8)$$

Note that the agreement between the different individual sensors is extremely close for a given Reynolds number. These results are plotted in figure 6 and compared to the correlation recommended by Petukhov (see Kays and Crawford, reference 14) in the form

$$Nu = \frac{Re Pr (C_1/2)}{1.07 + 12.7 (Pr^{2/3} - 1) \sqrt{C_1/2}} \quad (9)$$

where

$$\frac{f}{2} = (2.236 \ln Re - 4.639)^{-2} \quad (10)$$

In order to determine if the variation in measurements at different circumferential positions was caused by variations in the individual heat flux sensors, their positions were interchanged several times. It was found that readings by different sensors at the same positions and test conditions varied by less than 3% which is within the estimated uncertainty. It was concluded that most of the variation in the readings was due to variations in the actual local heat flux caused by slight variations in the local wall temperature.

The time response of the sensor was investigated for this application by applying a step change in the heater voltage during a measurement. The resulting transient response of the differential thermocouple voltage can then be used to determine the time constant for the sensor under these conditions. The results of a particular measurement are shown in figure 7. The time constant under these conditions was found to be 43 seconds. This relatively long time constant makes it easy to null the instrument and is not limiting on the application of the sensor in most heat transfer investigations since steady conditions for most experiments take much longer times.

## CONCLUSIONS

A new design for a balance type heat flux sensor has been described. The primary advantage of this design over earlier sensors is its modular characteristic and ability to be inserted into a wall to study either exterior or interior heat transfer. It also uses a thin film resistor heating element not used in earlier designs. Unlike earlier sensors of this type, it can and has been fabricated in quantities. Tests with different individual sensors under the same test conditions show that the sensors produce repeatable results within the estimated uncertainty of the measurements.

**ACKNOWLEDGEMENT:** The authors gratefully acknowledge the support of the U.S. Office of Naval Research (Power Program) through grant N00014-83-G-0021 under the direction of Professor B. E. Launder at UMIST. This collaborative effort was also made possible in part by the U.S.A. National Science Foundation grant MEA-84-41626

**NOTE:** Authors are listed in alphabetical order.

## REFERENCES

1. Emrich, R. J. "Methods of Experimental Physics, Vol 18B Fluid Dynamics," Chapter 7-Heat Transfer Gages by W. Paul Thompson, pp 663-685, Academic Press 1981.
2. Holman, J. P., "Experimental Methods for Engineers," Fourth Edition, McGraw Hill, 1984.
3. Doebelin, E. O., "Measurement Systems: Application and Design," McGraw Hill, 1975.
4. Eckert, E. R. G., and Goldstein, R. J., "Measurements in Heat Transfer," Second Edition, McGraw Hill, 1976.
5. Hornbaker, D. R., and Rall, D. L., "Thermal Perturbations Caused by Heat Flux Transducers and Their Effect on the Accuracy of Heating Rate Measurements," ISA Transactions, p.100, April 1963.
6. Gardon, R., "An Instrument for the Measurement of Intense Thermal Radiation," Review of Scientific Instruments, Vol. 24, No. 5, 1953, pp. 366-370.
7. Gardon, R., "A Transducer for the Measurement of Heat Flow Rate," ASME Transactions, 1960, pp. 396-398.
8. Hager, N. E., Jr., "Thin Foil Heat Meter," Review of Scientific Instruments, November 1965.
9. Malone, E. W., "Design and Calibration of Thin-Foil Heat Flux Sensors," ISA Transactions, Vol. 7, No.3, pp. 175-180.
10. Streigl, S. A., and Diller, T. E., "The effect of Entrainment Temperature on Jet Impingement Heat Transfer," ASME Journal of Heat Transfer, Vol 106, 1984, pp. 27-33.
11. Cook, W. J., "Determination of Heat Transfer Rates from Transient Surface Temperature Measurement," AIAA Journal, Vol. 8, No. 7, pp. 1366-1368.
12. Kraebel, J. S., Baughn, J. W., and McKillop, A. A. "An Instrument for the Measurement of Heat Flux from a Surface with Uniform Temperature," ASME Journal of Heat Transfer, Vol 102, PP576-578, August 1980
13. Achenbach, E., "Total and Local Heat Transfer from a Smooth Circular Cylinder in Cross-Flow at High Reynolds Number," Int. J. Heat Mass Transfer., Vol. 18, pp. 1387-1396.
14. Kays, W. M., and Crawford, M. E., Convective Heat and Mass Transfer, McGraw Hill, 1980, pg 243.

NOMENCLATURE

$A_s$	sensor face area ( $m^2$ )
$C_e$	sensor thermal conductance ( $W/^\circ C$ )
$C_f$	friction coefficient
$E_{RH}$	heater resistor voltage (V)
$E_{RS}$	shunt resistor voltage (V)
$E_\Delta$	differential thermocouple voltage ( $\mu V$ )
$I_{RS}$	shunt resistor current ( $\Omega$ )
$I_{RH}$	heater resistor current ( $\Omega$ )
$K$	fluid thermal conductivity ( $W/m^\circ C$ )
$Nu$	Nusselt number
$Pr$	Prandtl number
$P_s$	sensor power (W)
$q_c$	conduction heat rate (W)
$q_s$	sensor surface heat rate (W)
$q_s''$	sensor heat flux ( $W/m^2$ )
$R_{RS}$	shunt resistance ( $\Omega$ )
$R_H$	heater resistance ( $\Omega$ )
$Re$	Reynolds number
$R_{lw}$	lead wire resistance ( $\Omega$ )
$T_B$	fluid bulk temperature ( $^\circ C$ )
$T_s$	sensor temperature ( $^\circ C$ )
$T_w$	wall temperature ( $^\circ C$ )
$X_i$	independent variable

TABLE I

$x_i$	Value of $x_i$	$\delta x_i$	$\frac{\partial q_s^n}{\partial x_i} \delta x_i$ (W/m <sup>2</sup> )	$\frac{1}{q_s^n} \frac{\partial q_s^n}{\partial x_i}$ (%)
$E_{RS}$	1.3V	0.005V	1.33	0.37
$E_{RH}$	13.00V	0.05V	1.33	0.37
$R_H$	4700 $\Omega$	1.0 $\Omega$	.73	0.21
$R_{2W}$	11.9 $\Omega$	1.0 $\Omega$	.073	.02
$A_S$	105 mm <sup>2</sup>	3.5 mm <sup>2</sup>	11.42	3.33
$T_W - T_S$	0°K	.017°K	4.15	1.21

TABLE II  
 NUSSELT NUMBER MEASUREMENTS WITH  
 HEAT FLUX SENSORS

RE	NU <sub>1</sub>	NU <sub>2</sub>	NU <sub>3</sub>	NU <sub>4</sub>	NU <sub>5</sub>
33,700	75.33	73.31	74.43	70.60	71.45
58,600	121.6	122.1	125.8	116.8	118.2
87,500	165.5	162.5	—	159.6	162.1

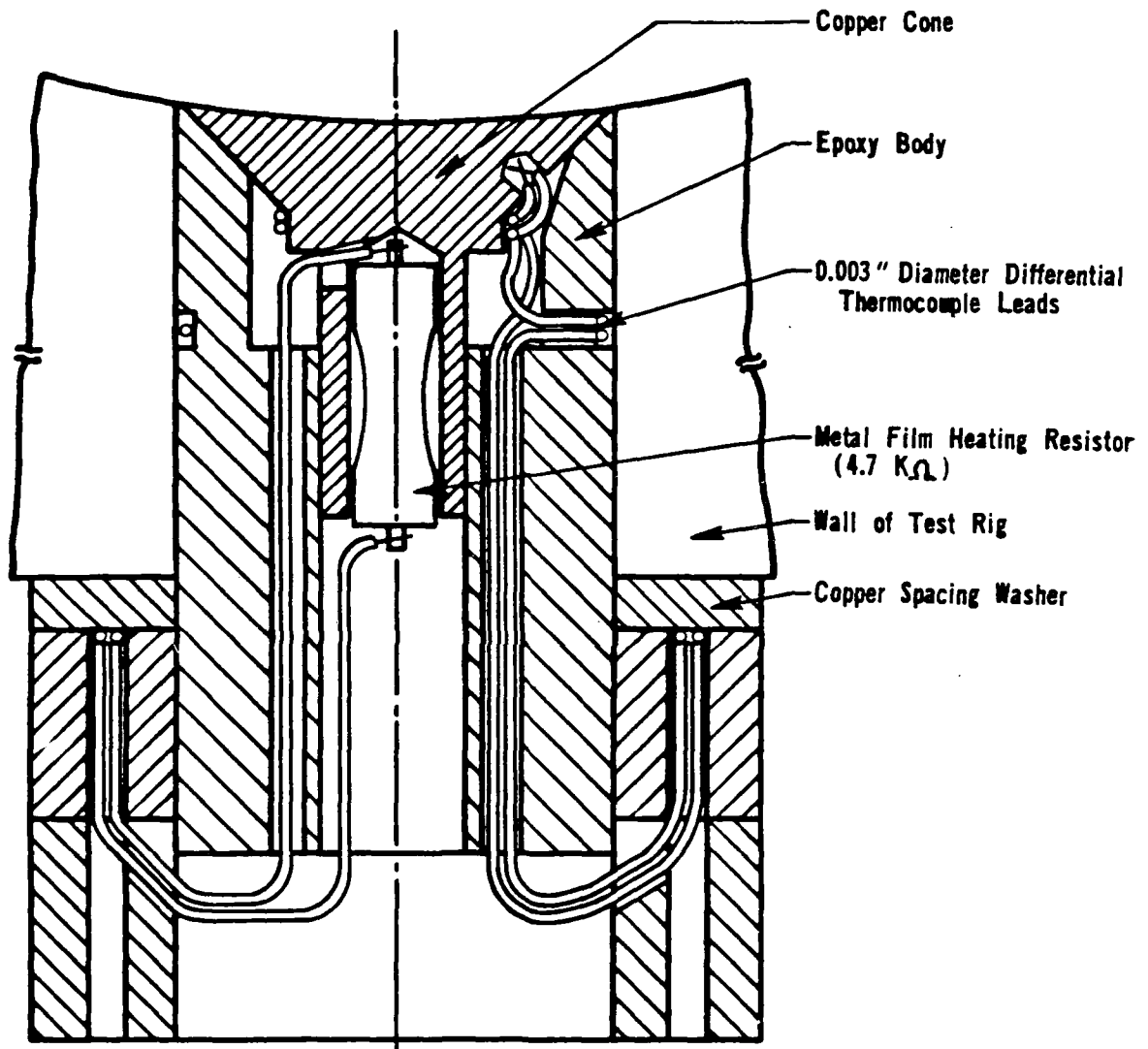


Figure 1 - Sectional Diagram of the Heat Flux Sensor

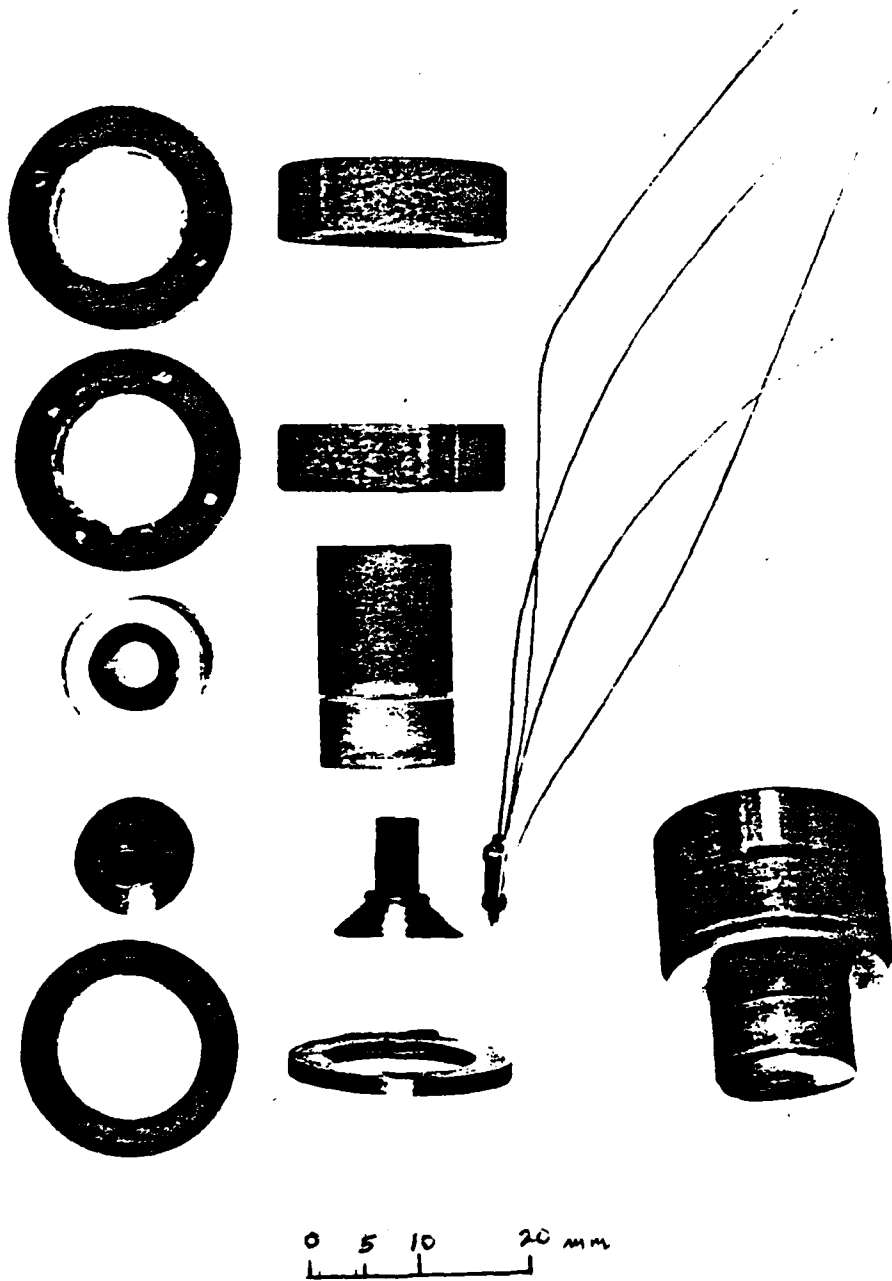


Figure 2 - Photograph of the Sensor and Components

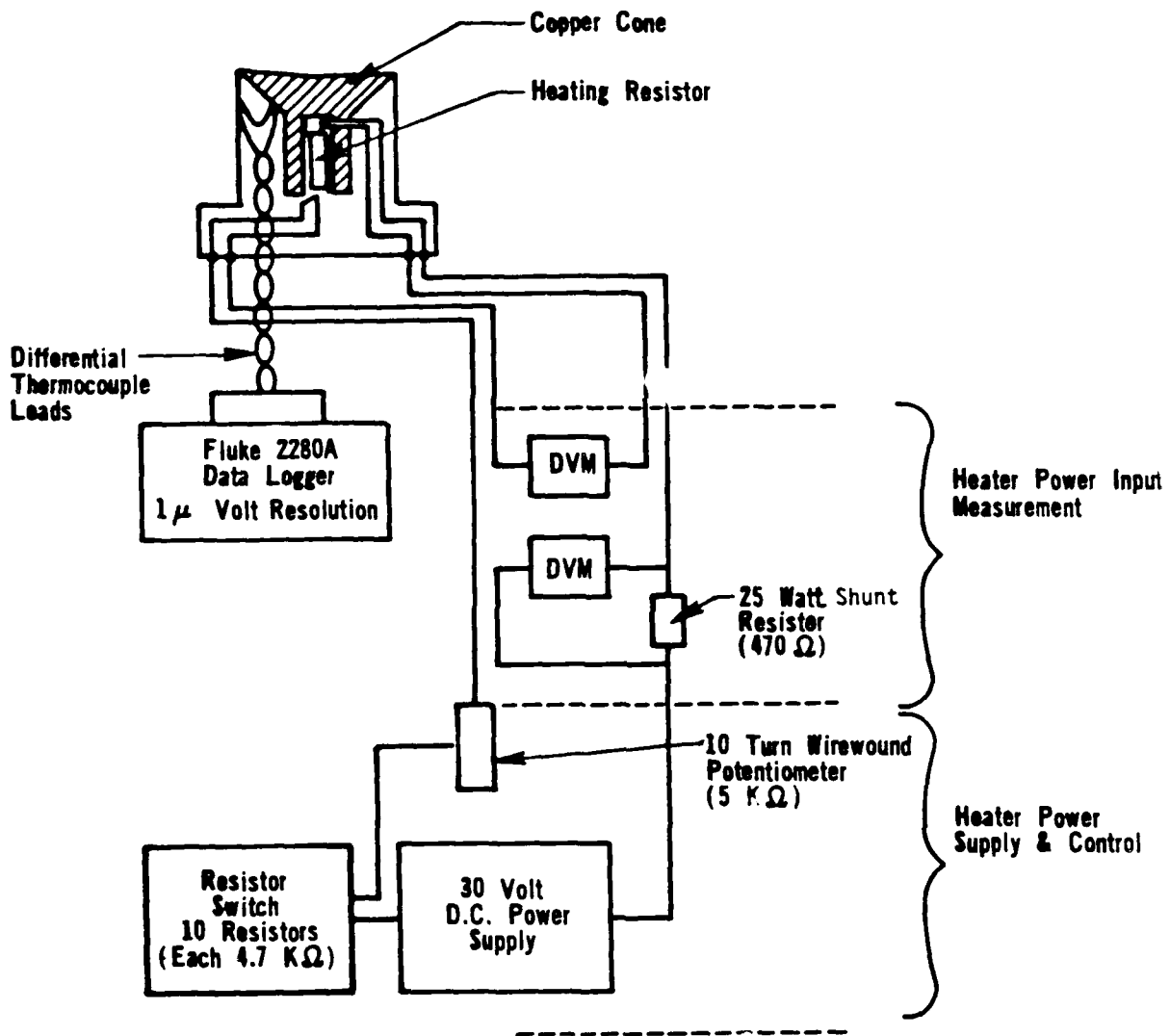


Figure 3 - Instrumentation and Wiring Diagram

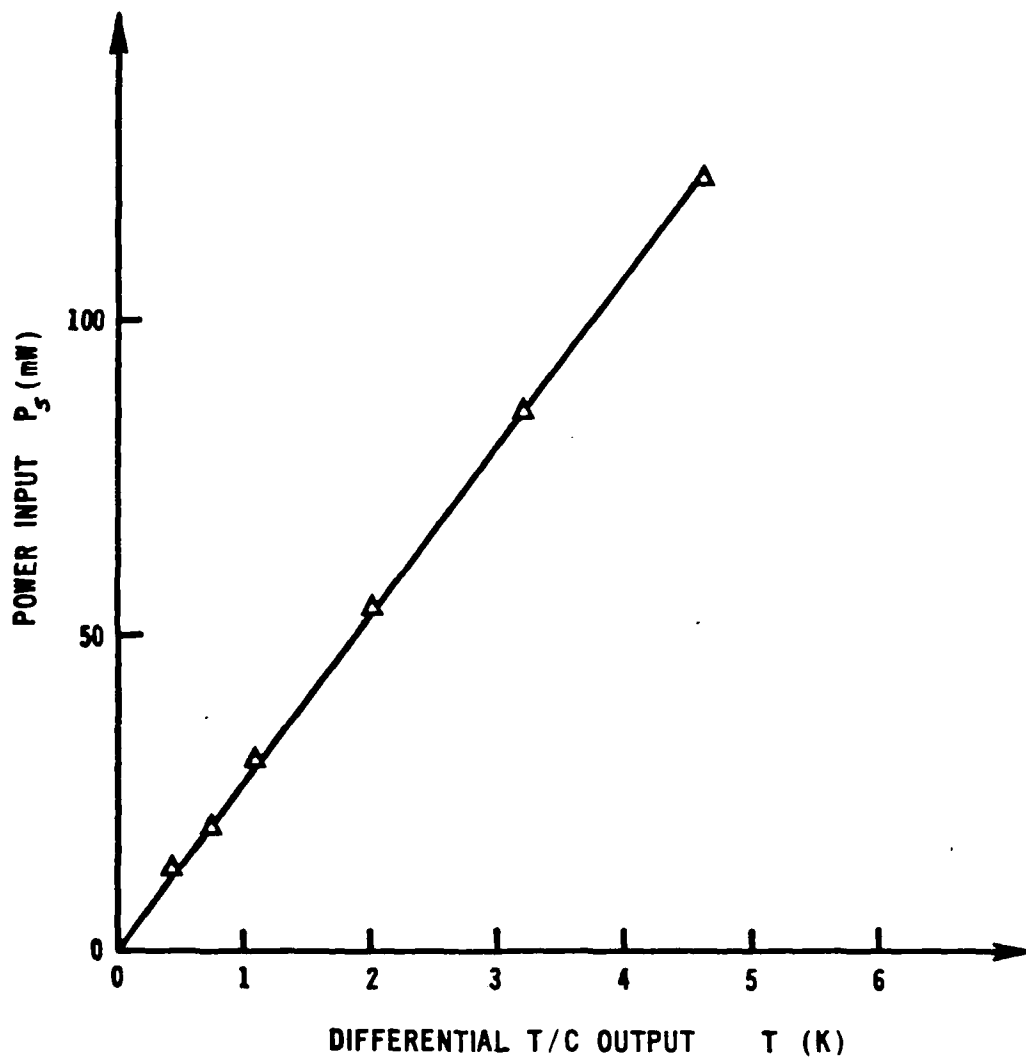


Figure 4 - Effect of Heater Power on the Differential Thermocouple Voltage During an Insulated Test

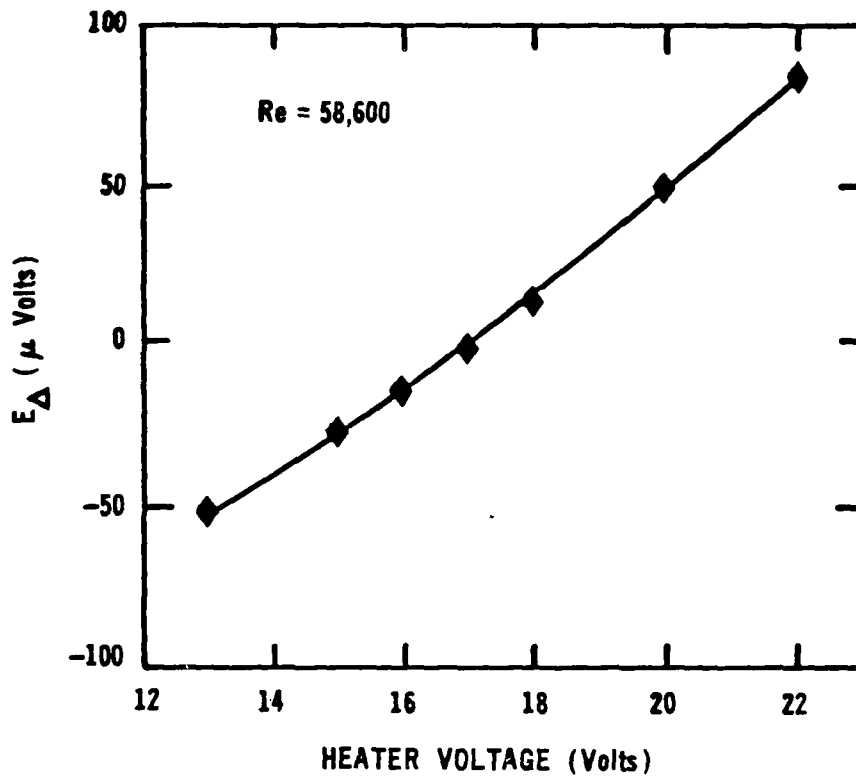


Figure 5 - Effect of Heater Voltage on the Differential Thermocouple Voltage During a Heat Duct Experiment

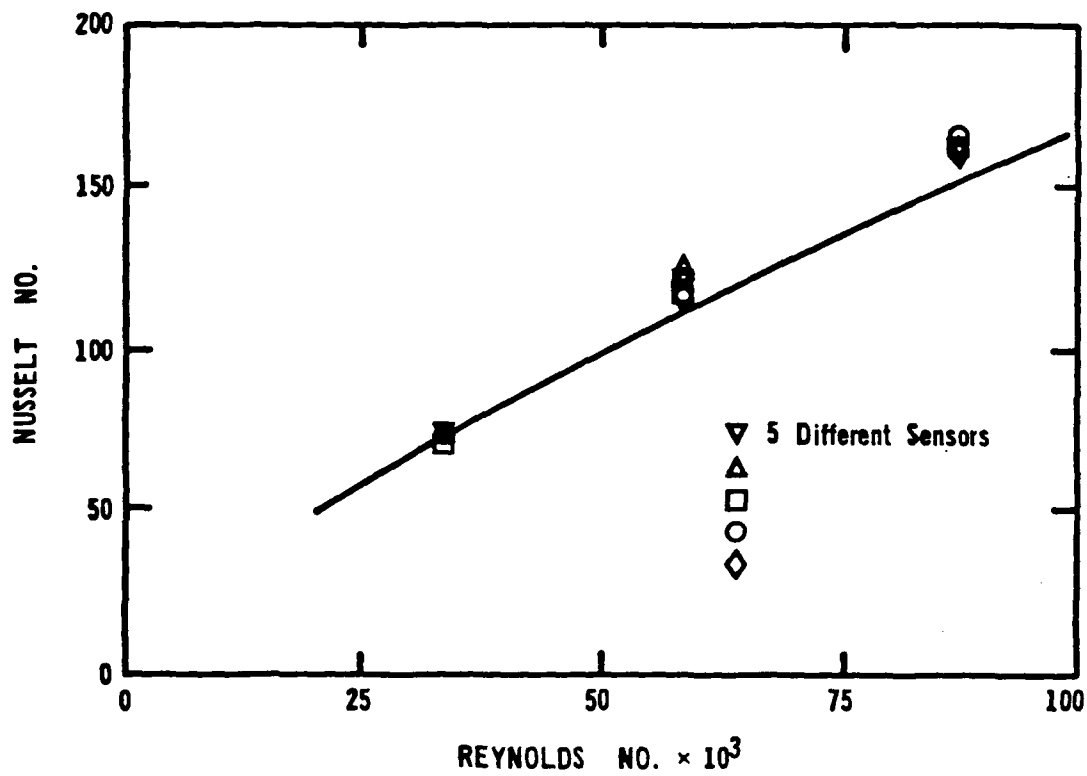


Figure 6 - Nusselt Number Results in a Heated Duct Experiment

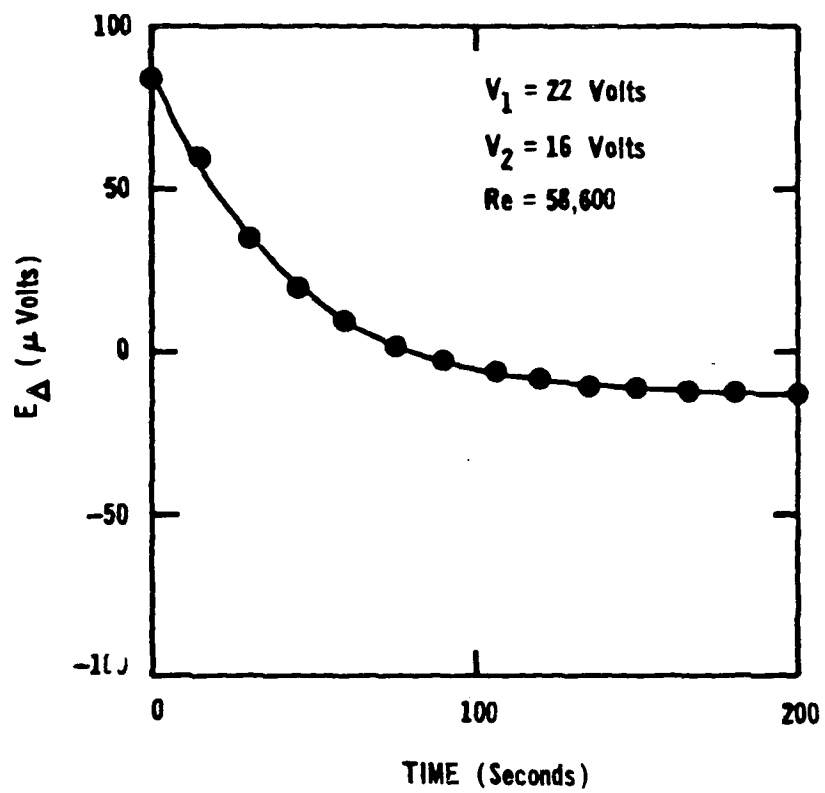


Figure 7 - Response of the Differential Thermocouple Voltage to a Step Heater Voltage Change During a Heated Duct Experiment

Local Heat Transfer Measurements in Turbulent Flow  
around a 180° Pipe Bend

by

J.W. Baughn\*, H. Iacovides, D.C. Jackson and B.E. Launder

UMIST

Abstract

The paper reports extensive convective heat transfer data for turbulent flow of air around a U-bend with a ratio of bend radius:pipe diameter of 3.375:1. Experiments cover Reynolds numbers from  $2 \times 10^4$  -  $1.1 \times 10^5$ . Measurements of local heat transfer coefficient are made at six stations and at five circumferential positions at each station. At  $Re = 6 \times 10^4$  a detailed mapping of the temperature field within the air is made at the same stations. The experiment duplicates the flow configuration for which Azzola and Humphrey [3] have recently reported laser-Doppler measurements of the mean and turbulent velocity field.

The measurements show a strong augmentation on the outside of the bend and relatively low levels on the inside associated with the combined effects of secondary flow and the amplification/suppression of turbulent mixing by streamline curvature. The peak level of Nu occurs half way around the bend at which position the heat transfer coefficient on the outside is about three times that on the inside. Another feature of interest is that a strongly non-uniform Nu persists six diameters downstream of the bend even though secondary flow and streamline curvature are negligible there. At entry to the bend there are signs of partial laminarization on the inside of the bend, an effect that is more pronounced at lower Reynolds numbers.

---

\* Mechanical Engineering Department, University of California, Davis

## 1. Introduction

Turbulent flow in a pipe bend is fundamental to many engineering components in the thermal power area, especially those associated with convective heat transport. As two examples may be mentioned the liquid side of a shell-and-tube heat exchanger and the interior cooling passages of turbine blades. The flow geometry is moreover sufficiently basic that - even for laminar flow - it has been the subject of numerous experimental, analytical and numerical studies.

In the turbulent flow regime the extensive pitot tube explorations by Rowe [1] of the approach to its fully developed state of flow in a gently curved U-bend threw considerable light on the markedly different flow structure at different positions in the bend. More recently two LDA explorations have helped provide more extensive mappings of the flow structure. Enayet et al [2] measured the distribution of streamwise mean and rms fluctuating velocity along several lines traversing the duct cross section at five stations within and downstream of a  $90^\circ$  bend with mean bend radius 2.8 times the pipe diameter. The mean velocity profiles showed clearly the piling up of low momentum fluid on the inside of the bend by the secondary flow. This low momentum fluid was further retarded by the adverse pressure gradient the flow on the inside encountered as it passed from the curved bend to the straight exit tangent. The study by Azzola and Humphrey [3] obtained measurements of the mean and rms values of both the streamwise and the circumferential (secondary) components along the diametral line at right angles to the duct's plane of symmetry. The data were obtained for two turbulent Reynolds numbers ( $Re_d = 5.74 \times 10^4$  and  $1.1 \times 10^5$ ) and at a total of 12 stations including five, at one-diameter intervals, immediately downstream of the bend. Their measurements of the secondary flow, summarized in Figure 4 and discussed more fully in Section 3, show in quantitative detail a number of the qualitative inferences drawn by Rowe [1], including the reversal of the secondary flow in the centre of the pipe by  $135^\circ$  into the bend.

No correspondingly detailed sets of data for heat transfer in circular-sectioned pipe bends are available. Local heat-transfer

coefficients for turbulent, nominally fully-developed flow have been reported by Seban and McLaughlin [4]. Their experiments, carried out over a range of Reynolds number, showed mean levels of heat-transfer coefficient some 50% above those for a straight tube and of the order of 2:1, the levels diminishing monotonically from the outside to the inside of the bend. Qualitatively this behaviour is to be expected: the secondary flow continually removes hot fluid\* from the outside of the bend and transports it to the inside. There is a further contributor to the circumferential non-uniformity. Streamline curvature will tend either to dampen or augment turbulent mixing depending on whether the mean angular momentum increases or decreases with radius (here referenced to the origin of the streamline, not the pipe centre). Bradshaw [5]. This effect reduces thermal mixing on the inside of the bend and increases it on the outside, i.e. its effect on the heat transfer coefficients in the same sense as that of the secondary flow.

The aim of the experimental work presented in this paper has been to provide detailed information about the convective heat transfer coefficient and thermal field in a developing flow around a bend, a more complicated and more important situation from a practical standpoint than fully-developed flow. Because of the desirability of having flow-field data as well (since convection by the secondary flow and modifications to the fluctuating velocity are the agencies determining the level of heat transfer coefficient), the experiment has been designed to replicate the geometry and boundary conditions of the 180°-bend experiments of Azzola and Humphrey [3]. Together, those experiments and the present ones provide the corresponding mapping for the circular tube that the recent experiments by Chang, Humphrey and Modavi [6] and Johnson and Launder [7] have reported for the square-sectioned U-bend.

---

\* assuming a heated tube wall

## 2. Apparatus, Instrumentation and Experimental Procedure

The test section, shown in Figure 1, consisted of a 76mm diameter circular-sectioned U-bend with inlet and exit tangents each 50 diameters long, 25 of which were instrumented for heating (see Figure 1). A short perspex spacer was interposed between the flanges separating the heated and unheated halves of the inlet/exit tangents to keep heat conduction to the unheated sections to unimportant levels. The apparatus was designed to provide a nearly uniform wall-temperature boundary condition, the tangent tubing being made from sections of thick-walled drawn aluminium tubing while the 180° bend itself was machined in two symmetrical halves from solid aluminium blocks. The mean radius of the bend was 6.75 times the pipe radius. The sections of the inlet and outlet tangents, each 0.95m in length, were flanged and spigoted at their ends to facilitate their connection together without mismatch at the pipe wall; for the same reason the upper and lower halves of the 180° bend were also spigoted.

The flow entered the test section via a 16:1 area contraction. The flow in the inlet tangent was rather sensitive to the flaring of the bellmouth and some of the earlier tests were taken without the contraction as this led to a more symmetrical velocity distribution. Later tests, with a re-designed bellmouth in place, achieved a further improvement in symmetry. Air was drawn through the rig by a 10 HP blower which provided a maximum test section Reynolds number of  $1.1 \times 10^5$ . Flow rates were monitored by an orifice plate located in a separate section leading to the blower; the plate itself and associated pipework conformed with BS1042.

Thermal measurements were made at five stations in the bend (15°, 55°, 90°, 125° and 165°) and at six diameters downstream. The data comprised local heat transfer rates measured at five circumferential positions in the top half of the bend. These were measured by heat-flux gauges developed at UMIST from an earlier design of Kraabel, Baughn and McKillop [8] and described in detail in Baughn et al [9]. Briefly, the copper cone providing the heating surface, with a small resistor embedded at its centre, was enveloped by a cylindrical body of low thermal conductivity epoxy

(Figure 2b). The unit was flush mounted with the surface of the pipe bend. Heat input to the resistor was adjusted until the cone temperature was brought to that of the surrounding pipe (to within  $0.015^{\circ}\text{C}$ ). Accurate measurement of the current supply to the resistor and the voltage applied across it enabled the heat flux through the exposed area of the sensor to be calculated. Prior to their use in the present study, the gauges were extensively tested in a straight pipe [9].

At one Reynolds number temperature, distributions within the air stream were made by means of a thermocouple rake consisting of seven PTFE insulated chromel-alumel thermocouples of 0.2mm diameter, Figure 2c. These were held by a tufnol (low thermal conductivity) support bar curved to match the radius of the pipe, thus allowing all seven thermocouples to record temperatures close to the wall. The rake was traversed vertically covering the lower half of the bend. Because of the time-consuming nature of this mapping, other tests merely recorded - with a single thermocouple - the temperature at the bend centre. Unlike the rake, the single probe could be inserted and removed through the stem access hole without disassembling the bend.

The heat supply to the bend itself and to the inlet and exit tangents was provided by self-adhesive heat tape (Clayborn Labs. Inc.) affixed to the outside of the bend with approximately 12mm spacing between adjacent tracks. The tape on the straight sections was wound helically while for the bend section twenty single tracks running axially were applied to the upper and lower halves of the bend. The electrical connections allowed the heating current to twenty tracks on the outer half of the bend (10 each from the upper and lower halves) to be controlled separately from the twenty on the inside. A two-dimensional finite-difference heat-conduction analysis indicated that at the inside surface of the tube temperature variations arising from the discrete heating on the outside amounted to no more than 2% of the temperature difference between the wall and ambient values. There was found to be a larger variation in wall temperature in the streamwise direction ( $\sim 7\%$ ) arising from changes in both the bulk temperature and the velocity field as the air passes around the bend. This variation was of course taken into account in

evaluating the Nusselt number data presented in Section 3.

Before the test programme began, the apparatus was checked for leaks by sealing off the pipework and pressurizing the rig. Thereafter velocity profiles were taken at two diameters upstream of the bend to establish that the flow was acceptably symmetric and to provide well-defined entry conditions. Figure 3 shows the mean and rms axial velocity profiles for both vertical and horizontal traverses; the horizontal traverse already shows a shift of the airflow towards the inside of the bend induced by the upstream effects of the bend on the pressure field. To verify that the cold-rig flow-field data (obtained by the Berkeley group) would be representative of flow conditions in the heated duct, the mean profile was measured again with a pitot tube with the duct both heated and unheated. No significant differences in the profile were noted with the pipe wall temperature  $20^{\circ}\text{C}$  above that of the entering fluid both showing complete agreement with the cold-flow profile obtained by the hot wire.

The heat transfer measurements were taken at three nominal Reynolds numbers:  $2 \times 10^4$ ,  $6 \times 10^4$  and  $11 \times 10^4$ . The two higher Reynolds numbers correspond closely with those for which the velocity field has been mapped by Azzola and Humphrey [3]. In our work the greatest attention has been given to the middle Reynolds number. Data have been obtained with the nominal wall temperature  $10^{\circ}\text{C}$  and  $20^{\circ}\text{C}$  above that of the air at inlet. Iacovides [10] has provided a detailed analysis of experimental uncertainties. Based on this we estimate that the Nusselt number data are accurate to within  $\pm 4\%$  at the highest Reynolds number with  $20^{\circ}\text{C}$  overhear (where uncertainties are least) and to within  $\pm 10\%$  for a  $10^{\circ}\text{C}$  overhear at  $\text{Re} = 2 \times 10^4$  (where uncertainties are greatest).

### 3. Presentation and Discussion of Results

First we re-examine the mean velocity field data of Azzola and Humphrey [3] summarized in Figure 4 to provide a background for presenting the thermal measurements. The velocities were taken along the vertical diametral line perpendicular to the plane of geometric symmetry. Fully-developed pipe flow at entry leads

to a rapid development of secondary velocities which, by  $45^\circ$  into the bend, reach a peak value of about 30% of the bulk streamwise velocity, the maximum occurring very close to the wall. The secondary motion carries slow moving fluid near the pipe wall to the inside of the bend; correspondingly faster moving fluid close to the symmetry plane migrates towards the outside of the bend giving the classical single-cell vortex. By  $90^\circ$  into the bend, the convection of fluid by the secondary motion shifts the peak in streamwise velocity near the pipe wall with a minimum at the pipe centre. Because of this inversion the radial pressure gradient now acts to drive fluid near the pipe centre to the inside of the bend ( $135^\circ$ ) and this reverse stirring makes the streamwise velocity virtually uniform along the measurement line ( $177^\circ$  to four diameters downstream).

Figure 5 provides the corresponding temperature mapping obtained in the present explorations at a nominal bulk Reynolds number of  $6 \times 10^4$  and for the tube wall heated  $\approx 20^\circ\text{C}$  above ambient. The variation of  $(T_w - T)/(T_w - T_i)$  along seven vertical lines is shown; the centre line is the same as that on which the velocity profiles of Figure 4 were obtained. Here  $T_w$  is the wall temperature,  $T$  the local air temperature and  $T_i$  the air temperature at inlet to the pipe. At  $15^\circ$  into the bend the temperature field differs little from that found in a straight pipe: along each traverse line the normalized temperature rises monotonically from the wall to the symmetry plane while along the symmetry plane itself the temperature is nearly symmetric with respect to the pipe centre.

A sharply different picture has developed by  $55^\circ$ . Along the two traverse lines closest to the inside of the bend, a deep trough in normalized temperature appears in the vicinity of the symmetry plane associated with hot air from the immediate proximity of the bend wall being lifted away from the surface and carried towards the pipe centre by the secondary flow. Along the third line there is only a weak dip in normalized temperature at this station and none at all along the fourth (the diametral line): this is because at these locations the secondary motion has brought fluid at only a slightly different temperature than that originally occupying that position. Over the outer half of

pipe a reverse picture emerges: here the secondary flow "imports" faster moving, cooler fluid (i.e. with larger normalized temperatures).

The temperature field at  $90^\circ$  is very much a continuation of the developments seen at  $55^\circ$ . There is now a marked dip in temperature along the centre traverse line, a feature which matches the dip in streamwise velocity noted above in Figure 4. The profiles at  $125^\circ$  and  $165^\circ$ , like the corresponding velocity profiles, now show little variation along the traverse lines though there remains a significant rise in (normalized) temperature from the inside to the outside of the bend. By six diameters downstream of the bend the re-establishment of new thermal boundary layers on the pipe wall is evident.

The overall picture that emerges from the temperature-field data is one that is fully compatible with the Azzola-Humphrey velocity measurements. Indeed, because the present measurements provide a view of the temperature field over the whole cross section, they allow a fuller, more quantifiable impression than could be gained from the flow-field data alone.

The measured heat-transfer coefficients, expressed in terms of Nusselt number, are presented in Figure 6. It is emphasized that in the definition of  $Nu$  the temperature difference is that between the local wall value and the air temperature at the centre of the tube. This basis was adopted because the bulk mean temperature at any station could not be determined with great precision since the experiments were with a (nearly) uniform wall temperature. Figure 6 relates to precisely the test conditions for which the interior temperature profiles were obtained - indeed, the rake was still in place, pushed down as far as possible while the measured heat fluxes were obtained around the top half of the duct. Perhaps the first thing to notice is that even by  $15^\circ$  an appreciable circumferential variation of heat flux has developed. Much stronger circumferential variations are found as one proceeds around the bend, a development due partly to the secondary flow (the 'impingement' of cool fluid on the outer wall will obviously raise heat transfer rates) and partly to the modifications to the turbulent mixing, augmentation occurring on

the concave surface and damping on the inside of the bend. The maximum mean level of  $Nu$  occurs at  $90^\circ$ . The variation from the inside to the outside of the bend is also largest there: extrapolation to  $0^\circ$  suggests an outer-to-inner variation of 3:1. The mean level and the circumferential variation of Nusselt number falls gradually over the second half of the bend due to decay of secondary flow (see Figure 4b). Even six diameters downstream, however, there is still a 2:1 variation in  $Nu$  between (what had been) the inside and outside of the bend. The reason for this seems to be that due to the virtual disappearance of the secondary flow the hottest fluid, which during passage around the bend accumulated on the inside, simply stays there (Figure 5f) until eventually the (relatively) slow process of turbulent diffusion restores axial symmetry to the temperature field. Evidently, however, this occurs only far downstream of the region examined in the present experiments.

More extensive heat-flux measurements in the bend itself were made in which just the centreline temperature was measured; in this way the risk of affecting the surface heat flux pattern with the thermocouple rake was avoided. Figure 7 shows the distributions of Nusselt number for nearly the same Reynolds number as Figure 6 for two temperature differences:  $20^\circ\text{C}$  (as in Figure 6) and  $10^\circ\text{C}$ . In a few positions the heat-flux gauge went 'open circuit' during the test, which is why data points are occasionally missing. The variation is very similar to that shown in Figure 6, though on the whole the levels are lower by, on average, 5%. For the test in which data with the temperature difference was reduced to  $10^\circ\text{C}$  the levels of  $Nu$  lie on average 8% below those for a  $20^\circ\text{C}$  temperature difference. Two earlier tests, in which just the heat transfer rates were measured, also showed the same effect, i.e. the heat fluxes divided by the temperature difference at inlet was 8-10% less at the lower heating rate.

The decrease in density associated with heating could be expected to raise the Nusselt number in a curved pipe by two mechanisms. Firstly, the secondary flow driving force is raised since the lowest density fluid is also the slowest moving. Secondly, there will be some tendency for cooler (denser) turbulent eddies to centrifuge to large radii thus promoting

mixing on the outside of the bend (though dampening it on the inside). Neither mechanism looks powerful enough to have a significant effect, however, when such small density differences are involved. We note, moreover, that at a Reynolds number of  $1.1 \times 10^5$ , for which results are shown in Figure 8, there are no significant differences between the  $20^\circ\text{C}$  and  $10^\circ\text{C}$  experiments. Now, at this higher Reynolds number precision is greater because heat input rates are greater and heat losses of smaller significance. Our view is thus that the apparent sensitivity to  $\Delta T$ , shown in the data at  $Re = 5.8 \times 10^4$ , is probably not a real effect. The values obtained with the larger temperature difference are thus preferred.

Finally, Figure 9 shows the results of consolidating data for three Reynolds numbers - the two for which data are shown above and for 20,000. In all cases the measured Nusselt number is divided by  $Re^{0.8}$  for the test in question. While the data for the three tests broadly collapse together, there is evidently a diminution in the ratio of outer:inner heat transfer coefficient as the Reynolds number is raised, due mainly to a marked increase in Nusselt number on the inside of the bend - or, conversely, a sharp fall as  $Re$  is lowered. The indication seems to be that the diminished turbulent mixing near the inner wall is causing the viscous sublayer to become thicker at the lowest Reynolds number causing a substantial increase in thermal resistance. This is qualitatively similar to the effects found in other boundary layer flows subject to damping of turbulence. Indeed, for flows in coils it is known (see, for example, Sreenivasan and Strykowski [11]) that at Reynolds numbers below  $10^4$  the flow on the inside of the bend may become laminar even though turbulent flow is maintained on the outside.

#### Concluding Remarks

A detailed mapping has been provided of the thermal field in turbulent flow around a circular-sectioned U-bend for conditions corresponding to those for which Azzola and Humphrey have reported velocity field data. Together, the two experiments give a comprehensive documentation of the processes of convective heat

transport in a complex but well-defined three-dimensional turbulent flow. It is hoped that they will provide a searching test case for the three-dimensional flow computation procedures that are now becoming widely available for industrial design purposes.

Among the most striking results to emerge were:

- the large circumferential variation of heat transfer coefficient that developed by only  $15^\circ$  into the bend: nearly a 2:1 ratio for  $Re = 2 \times 10^4$ ;
- the attainment of maximum mean heat transfer coefficient at  $90^\circ$  into the bend at which station the maximum circumferential variation was also recorded (nearly 4:1 for  $Re = 2 \times 10^4$ );
- the persistence of strong circumferential non-uniformities in Nusselt number six diameters downstream of the bend.

#### Acknowledgements

The research has been sponsored by the U.S. Office of Naval Research (Power Program) through Grant N00014-83-G-0021 for which we express our gratitude and thanks. Special recognition must go to two UMIST technician staff: Mr. D. Cooper provided outstanding assistance in the design of the heat-flux meters, in constructing the apparatus and in providing support during test runs. Mr. R. Lever brought his remarkable machining skills to bear in fabricating the  $180^\circ$ -bend test section and many other precision-machined items in the test rig. Our thanks go also to Mrs. L.J. Ball who prepared the camera-ready manuscript with her usual and appreciated care.

Authors are listed alphabetically.

#### References

1. Rowe, M. J. Fluid Mech. 43, 771, 1970.
2. Enayet, M.M., Gibson, M.M., Taylor, A.M.K.P. and Yianneskis, M. Int. J. Heat and Fluid Flow 3, 211, 1982.
3. Azzola, J. and Humphrey, J.A.C. "Developing turbulent flow in a  $180^\circ$  curved pipe and its downstream tangent." Report LBL-17681, Lawrence Berkeley Laboratory, Univ. California,

1984. [See also Proc. 2nd Int. Conf. on Laser Anemometry, Lisbon, 1984].

4. Seban, R.A. and McLaughlin, E.F. Int. J. Heat Mass Transfer 6, 387, 1963.
5. Bradshaw, P. Agardograph 169, 1973.
6. Chang, S.M., Humphrey, J.A.C. and Modavi, A. Physico-Chemical Hydrodynamics 4, 243, 1983.
7. Johnson, R.W. and Launder, B.E. Int. J. Heat and Fluid Flow 6 (in press), 1985.
8. Kraabel, J.S., Baughn, J.W. and McKillop, A.A. ASME J. Heat Transfer 102, 576, 1980.
9. Baughn, J.W., Cooper, D., Iacovides, H. and Jackson, D.C. "An instrument for the measurement of heat flux from a surface with uniform temperature." Submitted to Rev. Scientific Inst., 1985.
10. Iacovides, H. PhD Thesis, University of Manchester Faculty of Technology, 1985.
11. Sreenivasan, K.R. and Strykowski, P.J. "Stabilization effects in flow through helically coiled pipes." Dept. Mechanical Engineering, Yale University, 1984.

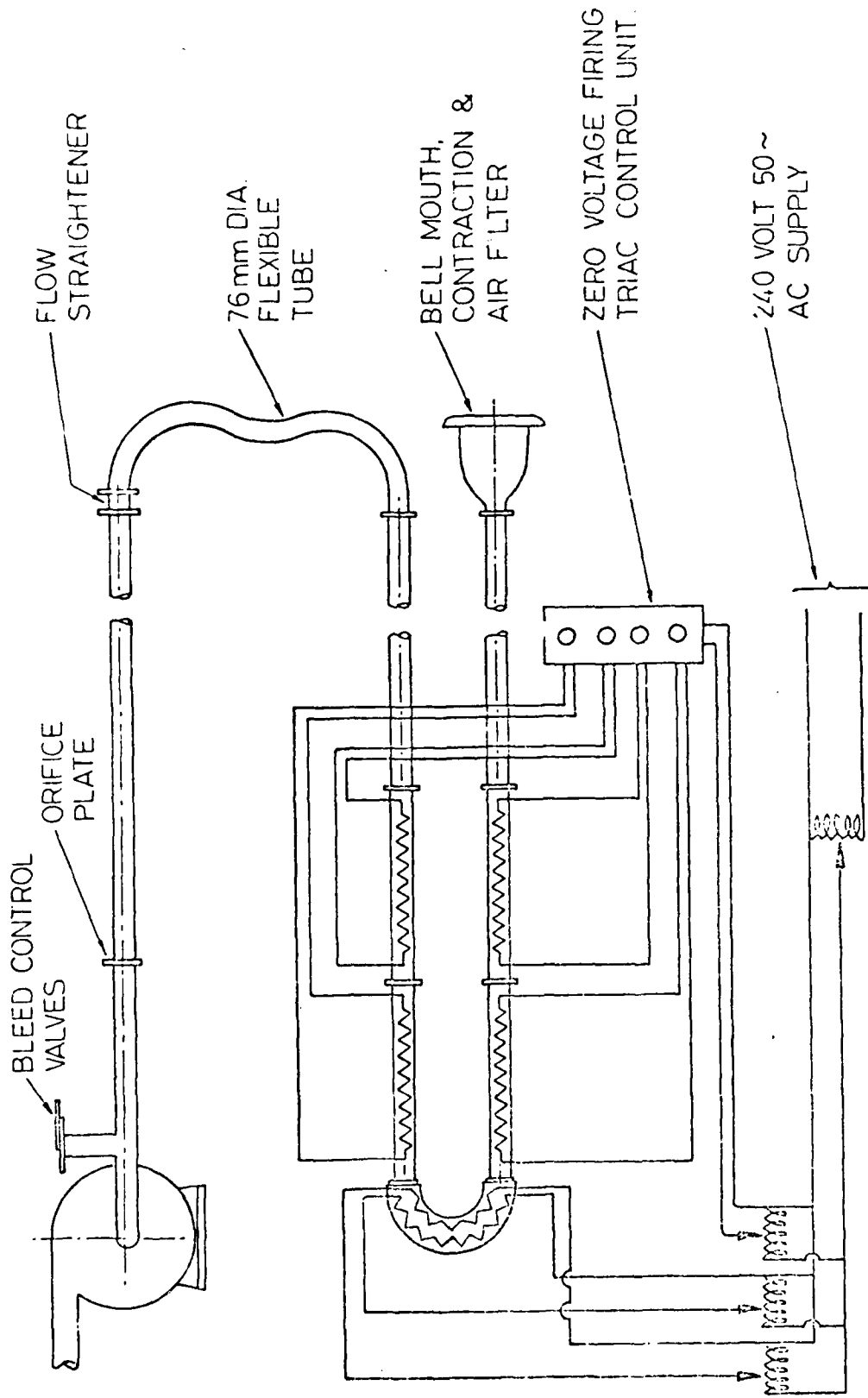


DIAGRAM SHOWING PIPEWORK AND HEATING ARRANGEMENTS FOR 180° BEND

Fig. 1 Schematic view of test section

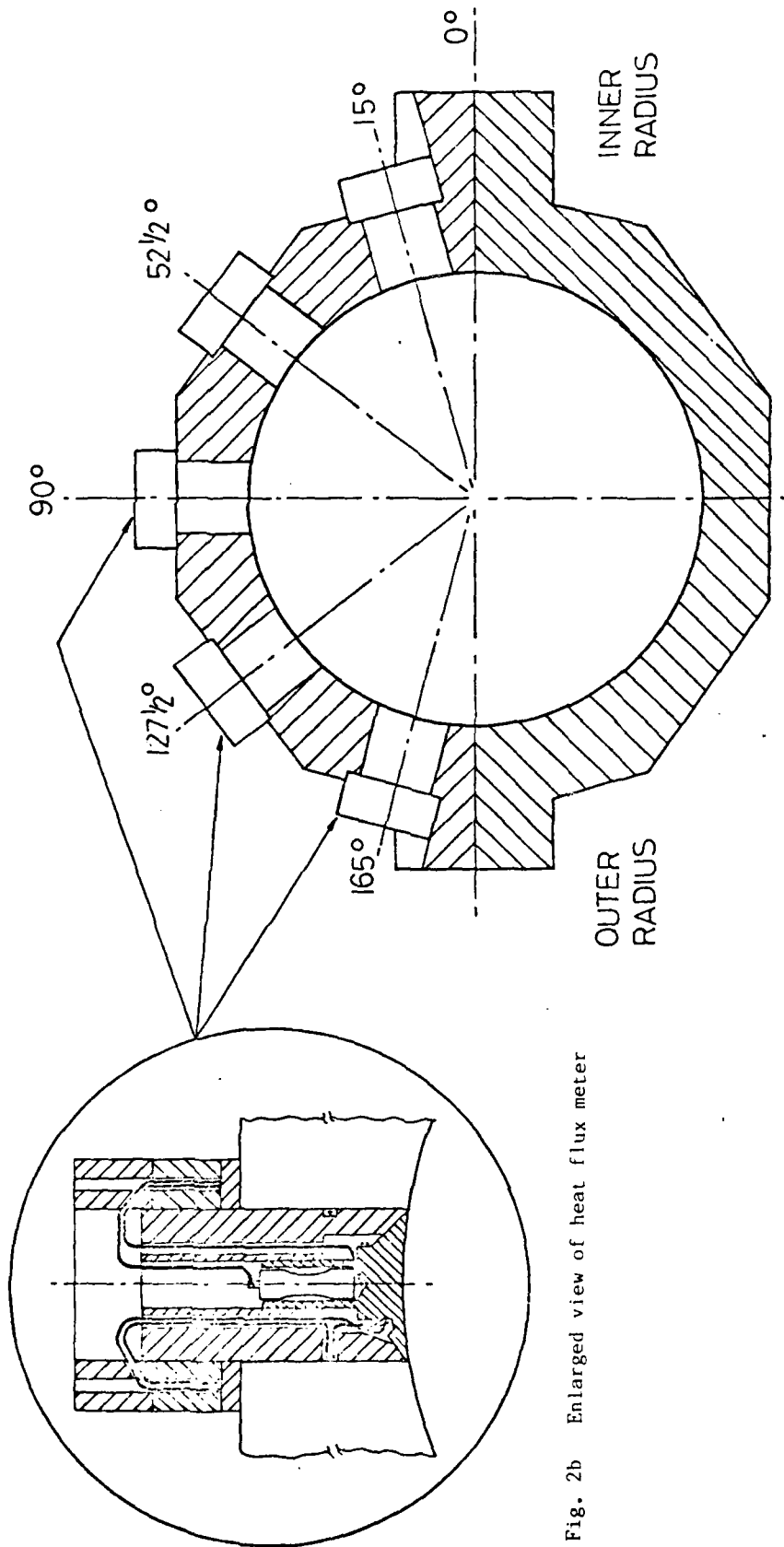


Fig. 2b Enlarged view of heat flux meter

Fig. 2a Cross section of U bend

CROSS SECTION THROUGH 180° BEND MEASURING SECTION

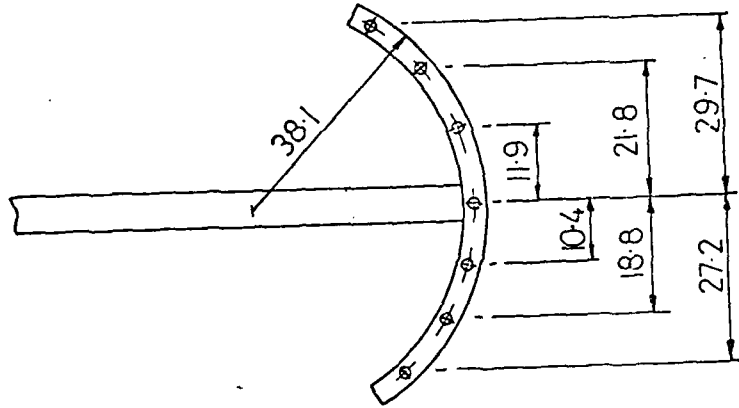
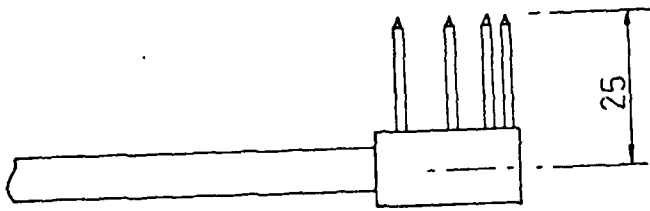


Fig. 2c Thermocouple rake

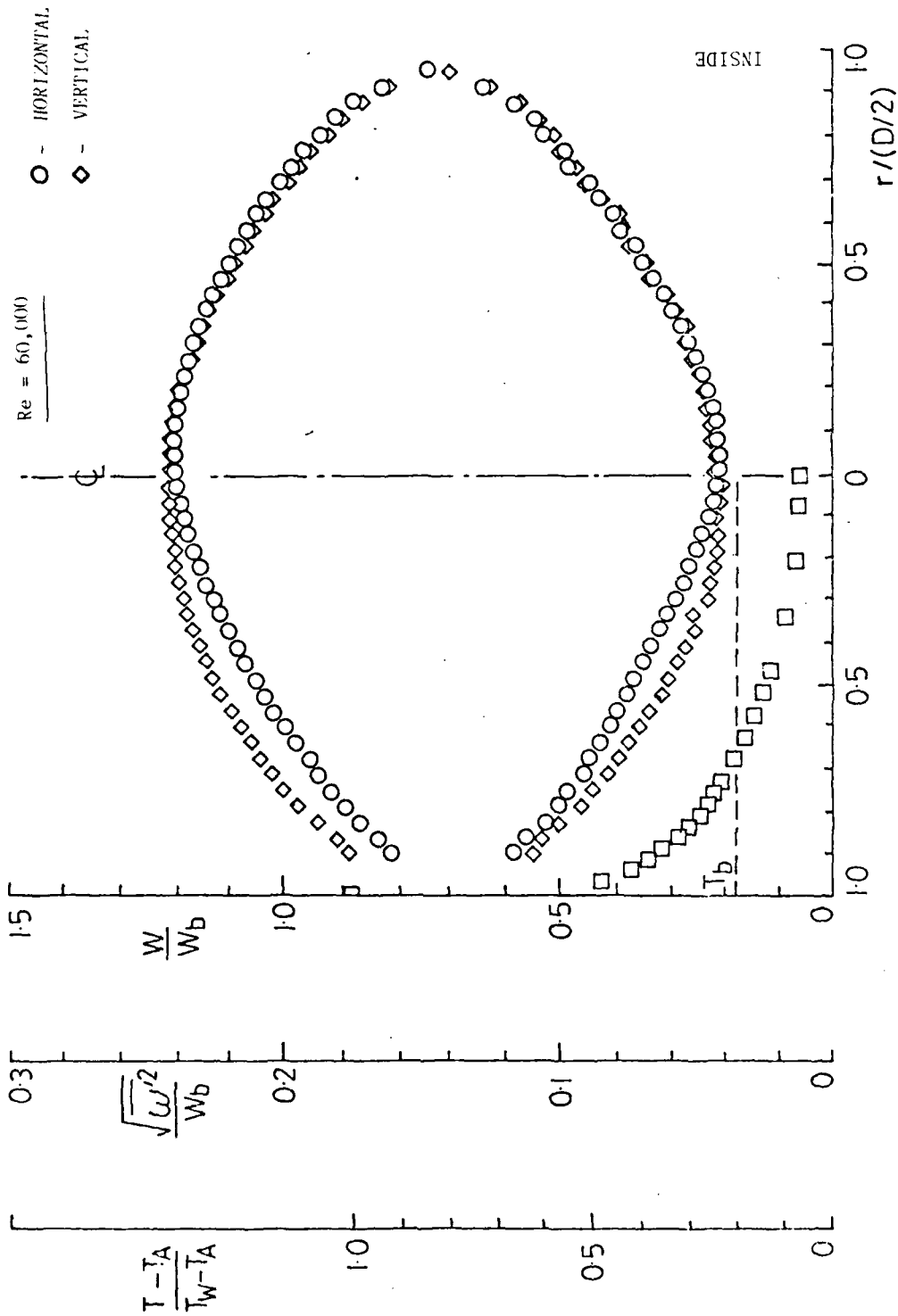
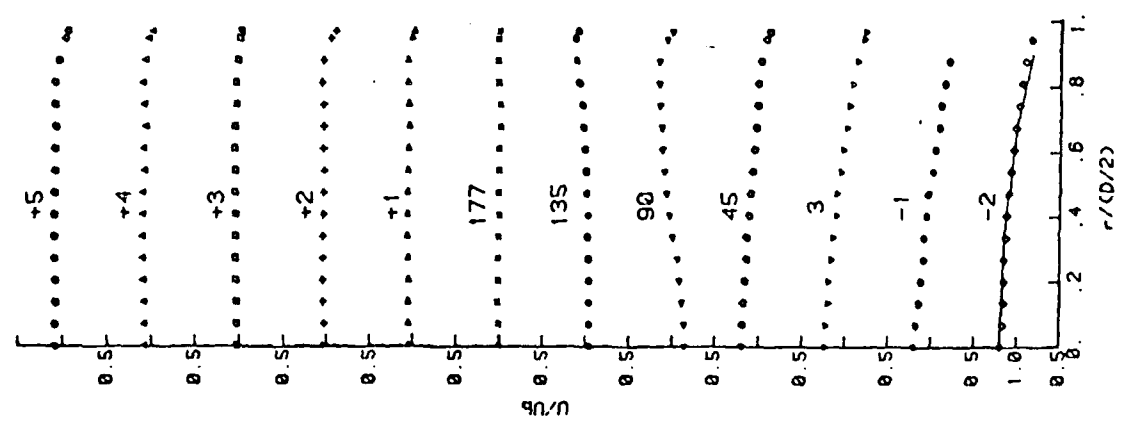


Fig. 3 Velocity and temperature profiles 2 diameters upstream of bend



Re = 57,400

Fig. 4a

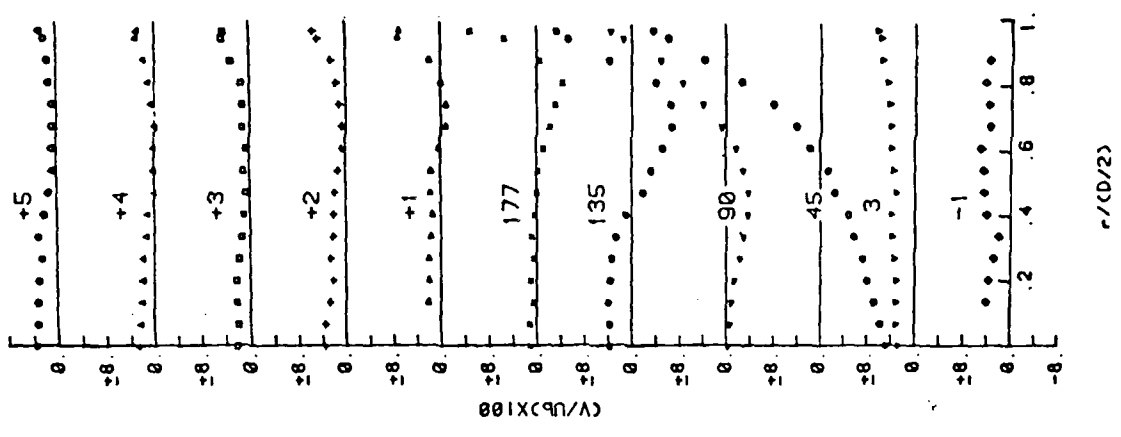


Fig. 4b

Fig. 4 Streamwise and circumferential mean velocity profiles along radius perpendicular to symmetry plane

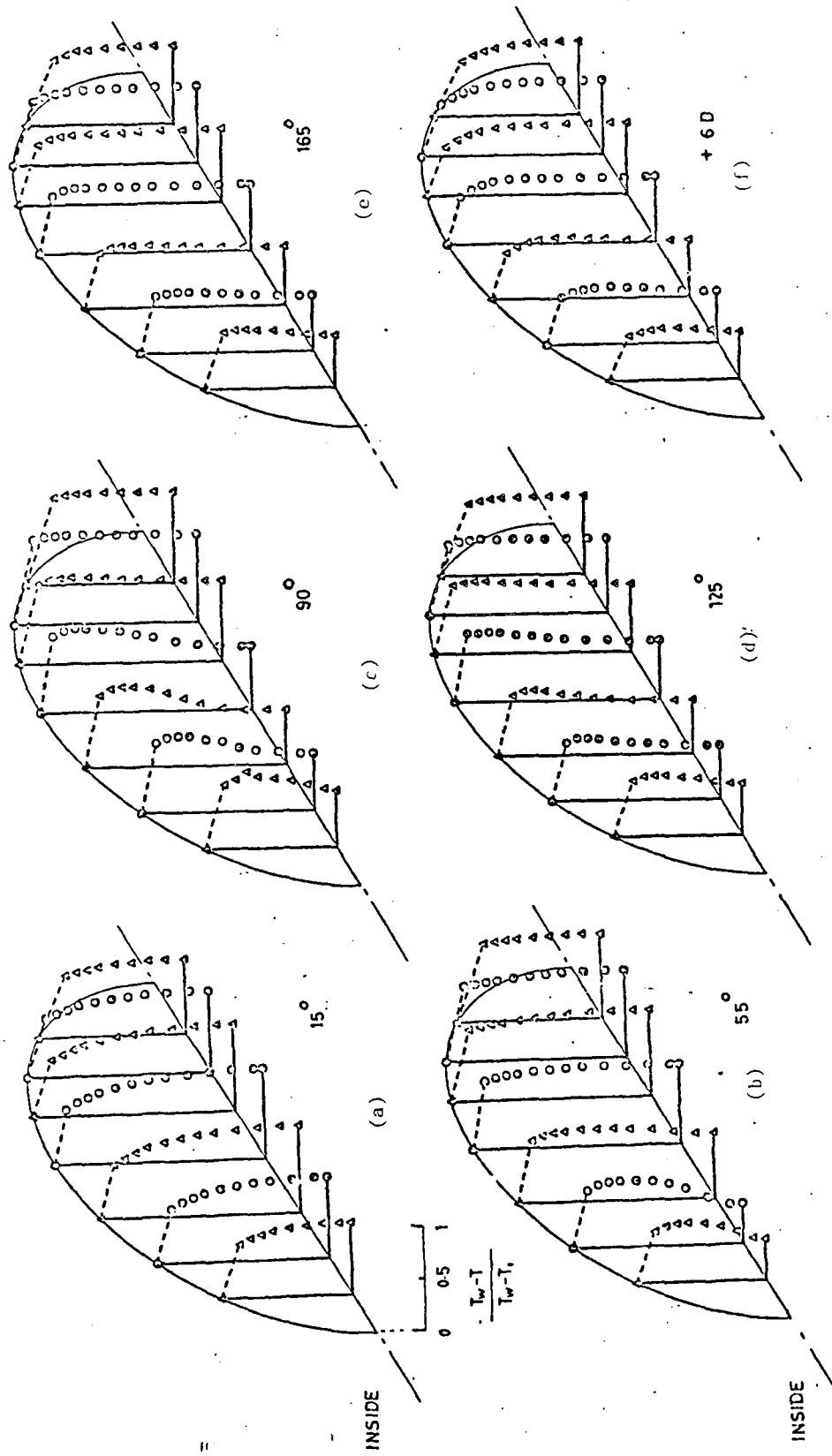


Fig. 5 Normalized temperature profiles in U bend

Re = 60,000  $\Delta T = 20^\circ\text{C}$

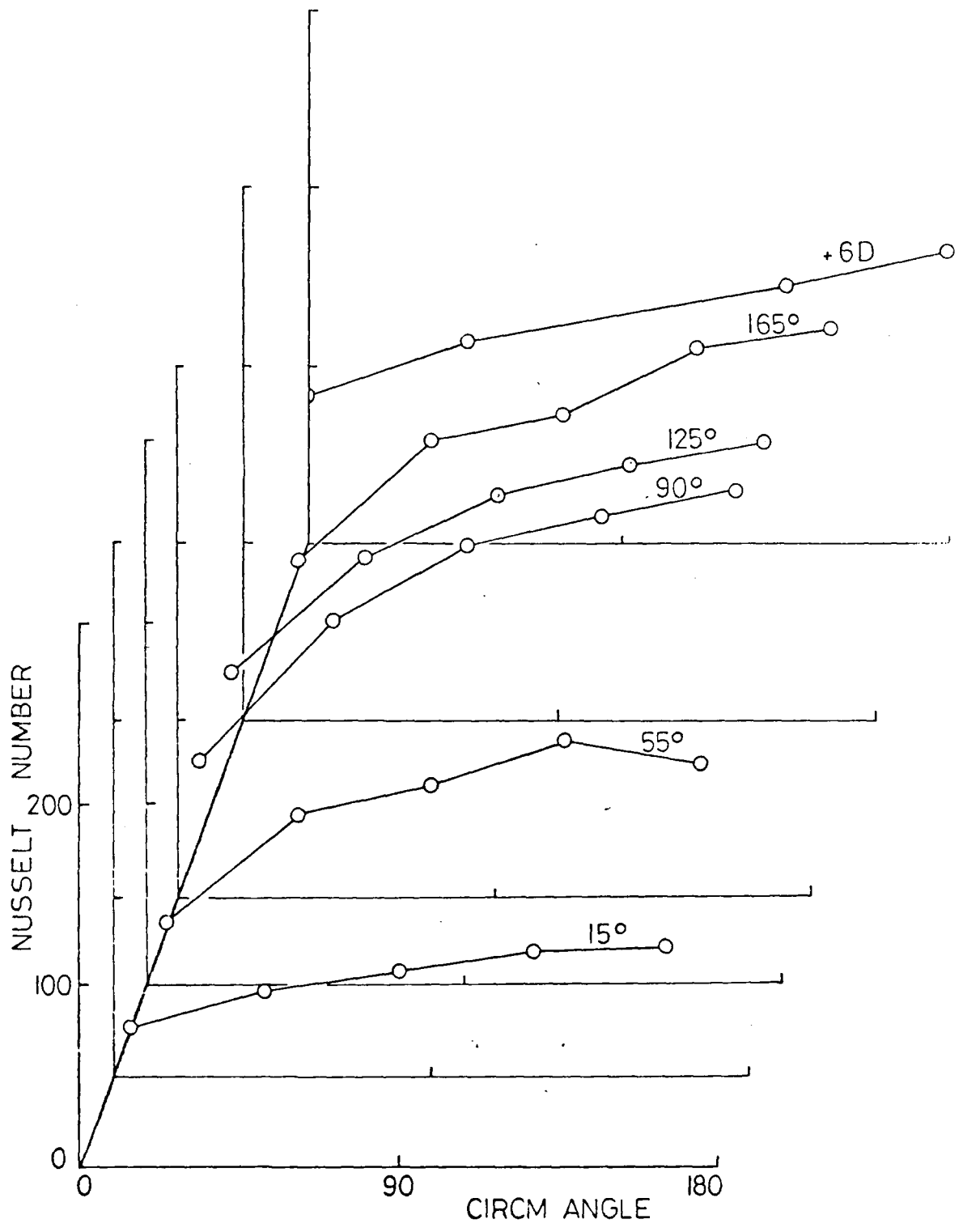


Fig. 6 Circumferential distribution of Nusselt number at six stations in and downstream of U bend

$\Delta T \approx 20^{\circ}\text{C}$  ;  $Re \approx 6 \times 10^4$  ; thermocouple rake in duct

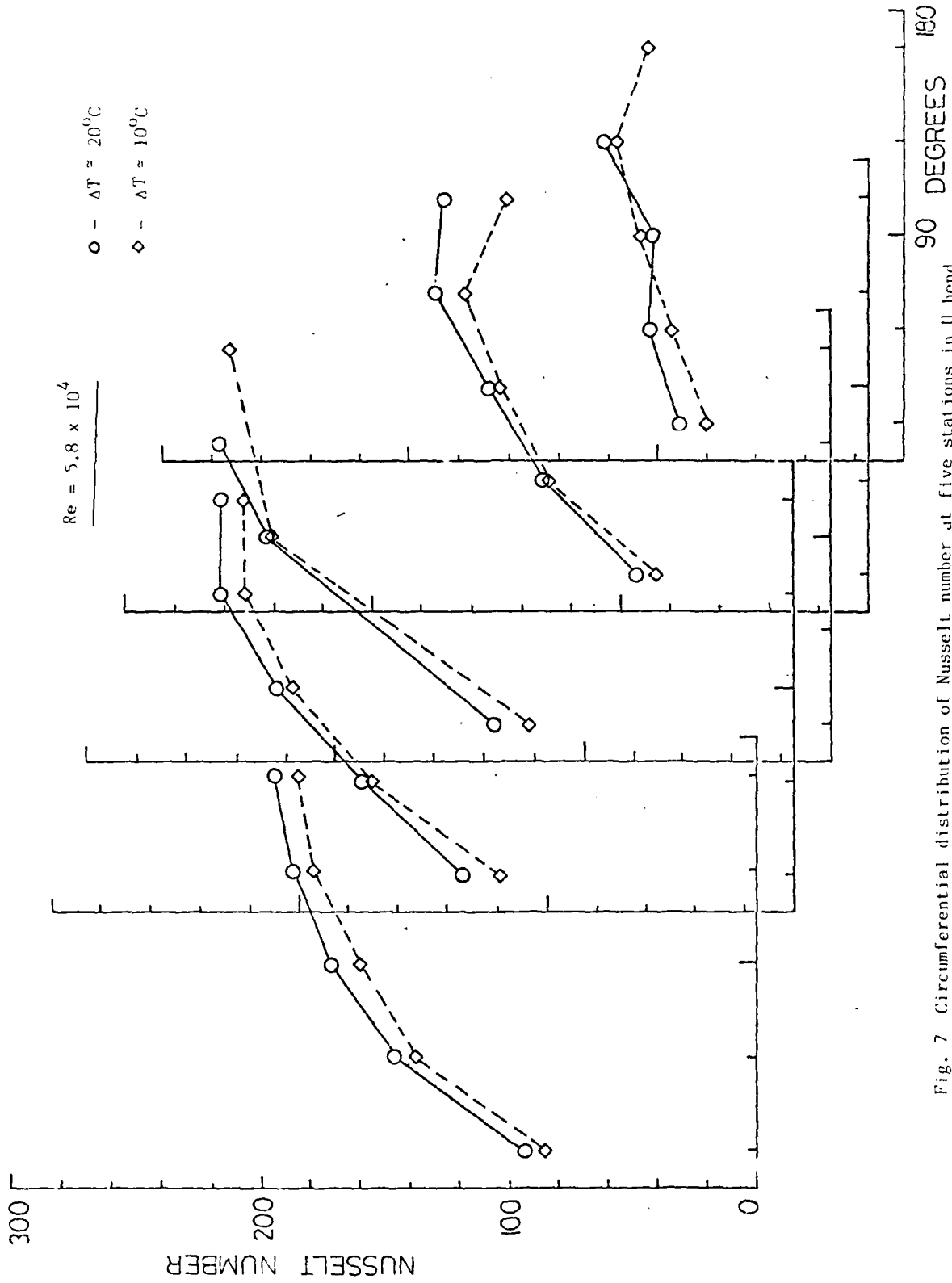


Fig. 7 Circumferential distribution of Nusselt number at five stations in U bend

$Re = 1.1 \times 10^5$

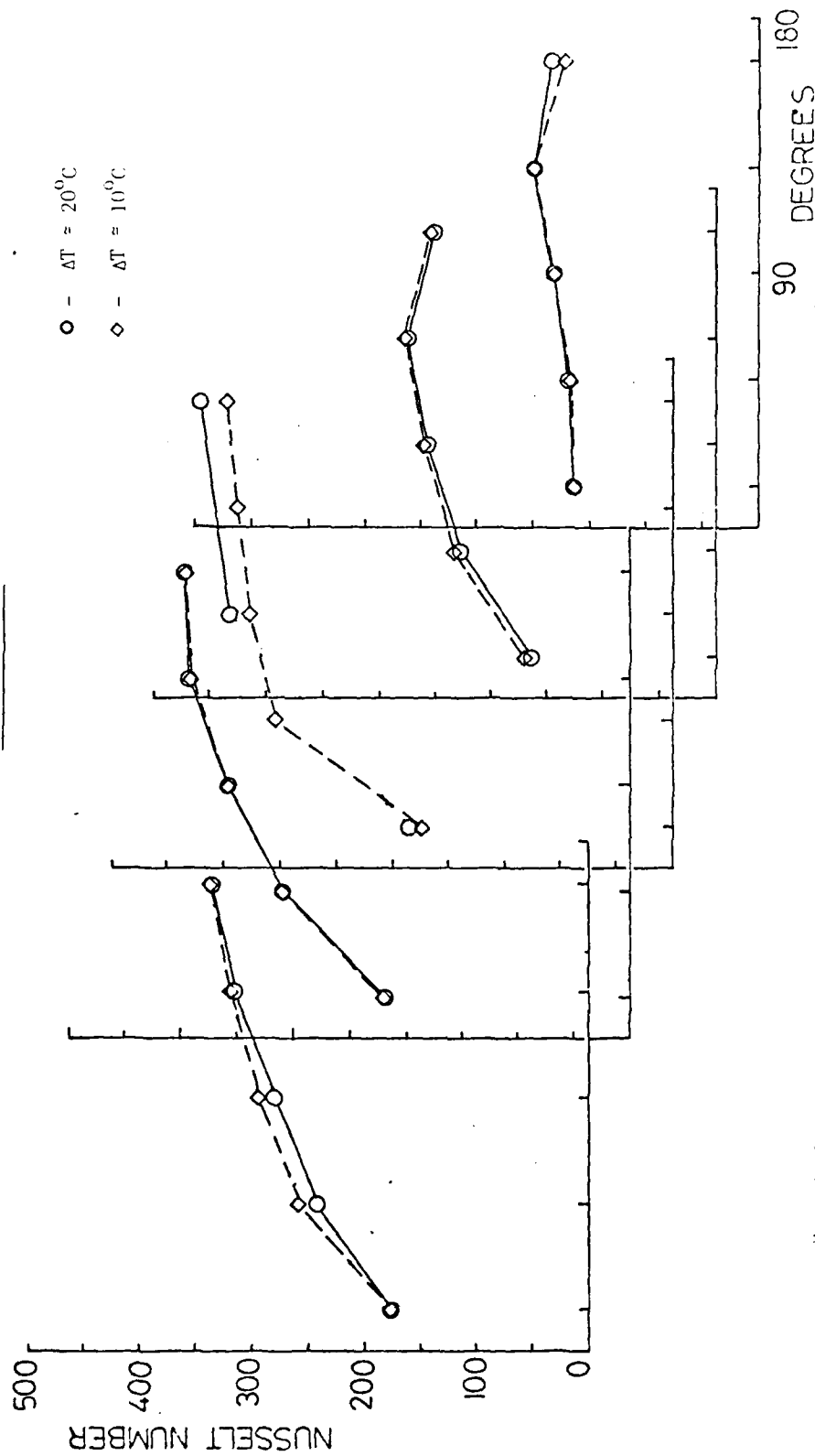


Fig. 8 Circumferential distribution of Nusselt number at five stations in U bend

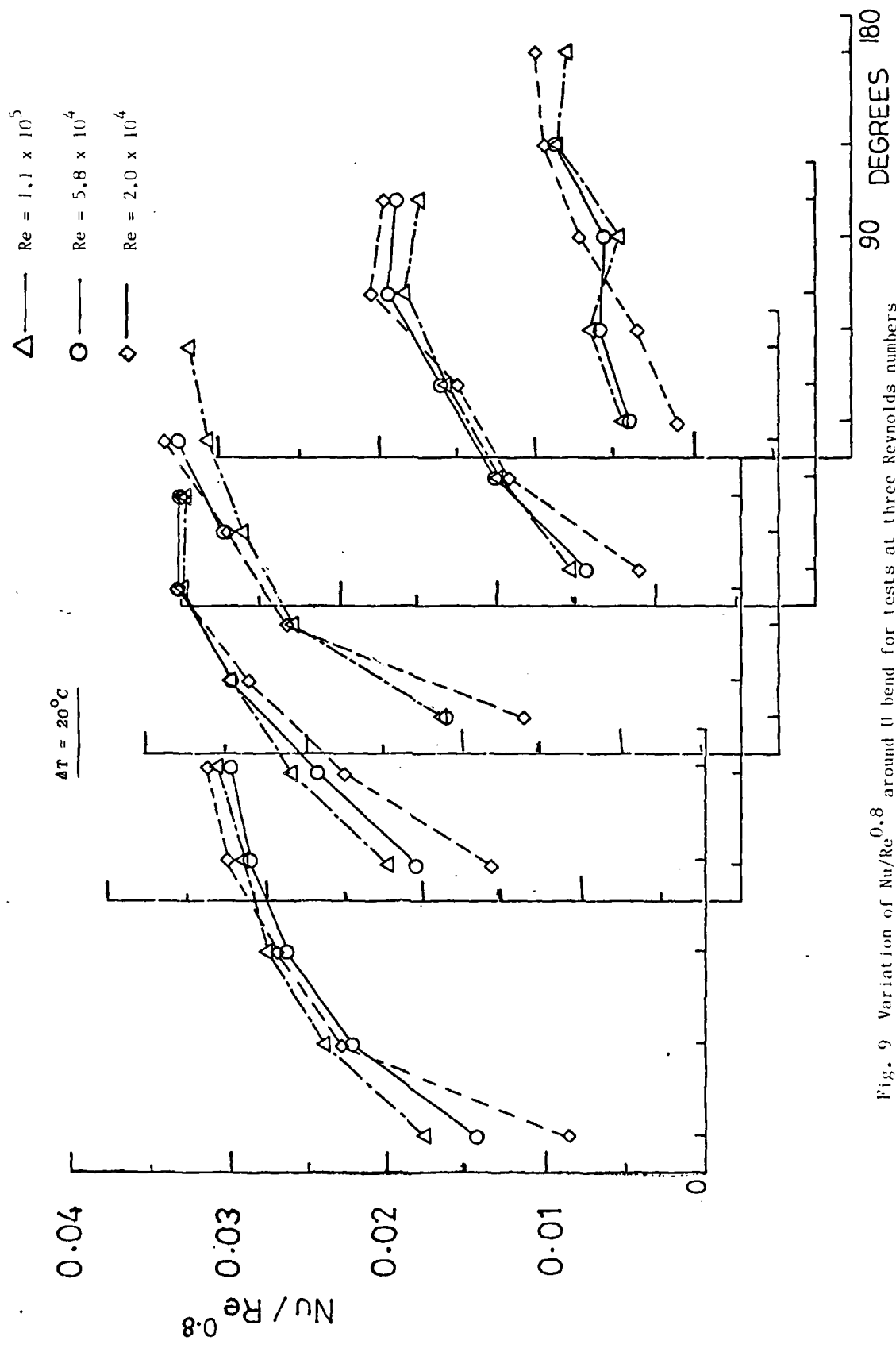


Fig. 9 Variation of  $Nu/Re^{0.8}$  around U bend for tests at three Reynolds numbers

DEVELOPING TURBULENT FLOW IN A U-BEND OF CIRCULAR  
CROSS-SECTION: MEASUREMENT AND COMPUTATION

by

J. Azzola<sup>1</sup>, J.A.C. Humphrey<sup>1</sup>,  
H. Iacovides<sup>2</sup> and B.E. Launder<sup>2</sup>

Report No. FM-85-3

Mechanical Engineering Department  
University of California, Berkeley

Accepted for publication in the  
Journal of Fluids Engineering, ASME

<sup>1</sup>  
Department of Mechanical Engineering, University of California, Berkeley,  
California, USA (Member of ASME)

<sup>2</sup>  
Department of Mechanical Engineering, UMIST, Manchester, UK, (Member of ASME)

Disc:Humphrey#7  
DTF16  
Loris

## ABSTRACT

Laser-Doppler measurements of the longitudinal and circumferential velocity components are reported for developing turbulent flow in a strongly curved 180° pipe and its downstream tangent. In the bend, the mean longitudinal velocity component changes little after  $\theta = 90^\circ$ , but the circumferential component never achieves a fully-developed state. Similar behavior is observed in the normal stresses, with large levels of flow anisotropy arising everywhere in the bend and downstream tangent. Between  $\theta = 90^\circ$  and  $X/D = 5$ , the circumferential velocity profiles display reversals of the secondary flow which are essentially independent of the Reynolds number.

Predictions of the flow development are presented based on a "semi-elliptic" truncation of the Reynolds equations in the main part of the flow with the standard  $k-\epsilon$  effective viscosity model used to approximate the turbulent stress field. In the immediate vicinity of the wall a simpler treatment, PSL, is adopted that allows the inclusion of the very fine mesh needed to resolve the viscous sublayer without excessive computer storage. The calculated behavior displays reasonably good agreement with the measurements in the bend, including the secondary flow reversals. Downstream of the bend, however, the rate of recovery of the flow is too slow, which points to the same weakness in the turbulence model as found in the recovery region of the flow over a backward-facing step.

## NOMENCLATURE

D	pipe diameter
De ( $\equiv Re(D/Rc)^{1/2}$ )	Dean number
k	turbulent kinetic energy
r	radial (cross-stream) coordinate
Rc	curved pipe radius of curvature
Re ( $\equiv DU_b/\nu$ )	Reynolds number
$u'$ ( $\equiv \sqrt{u^2}$ )	rms of the longitudinal velocity fluctuations
$u^2$	longitudinal component of normal stress
U	longitudinal component of mean velocity
$U_b$	bulk average velocity through the pipe
$v'$ ( $\equiv \sqrt{v^2}$ )	rms of the circumferential velocity fluctuations
$v^2$	circumferential component of normal stress
w	turbulent shear stress in r, $\phi$ plane
V	circumferential component of mean velocity
W	radial component of mean velocity
X	longitudinal (streamwise) coordinate in a straight pipe section

Greek Letters

$\epsilon$	dissipation of turbulent kinetic energy
$\theta$	longitudinal (streamwise) coordinate in a curved pipe section
$\nu$	fluid kinematic viscosity
$\phi$	circumferential (cross-stream) coordinate

## 1. INTRODUCTION

### 1.1 The Problem of Interest and Earlier Work

Over the last ten years, approximately, a substantial amount of experimental information has been obtained for developing turbulent flows in curved ducts of rectangular cross-section [1-7]. Detailed measurements in these important flow configurations, in particular of the secondary motions and complex turbulent characteristics which they induce, have been made possible by the non-intrusive laser-Doppler velocimetry technique. In contrast, turbulent flow-field measurements in curved pipes appear to be relatively sparse [8]. This is surprising given the practical importance of the curved pipe configuration. The lack of detailed data is partly explained by the greater difficulties associated with optical alignment through transparent curved surfaces.

The dominant influence of the flat walls on the secondary motion induced in rectangular ducts precludes the use of data obtained in these configurations to interpret accurately the characteristics of flow developing in curved pipes. For example, Cuming [9] shows analytically that, for equal radius of curvature to diameter ratio and dimensionless streamwise pressure drop, the ratio of the relative intensity of the secondary flow in a duct of square cross-section to that in a pipe of circular cross-section is 2.47 at the center line location. This result is strictly valid only for fully developed laminar flow. Comparisons between present results and corresponding measurements by Chang, et al. [5] in a curved duct of square cross-section with similar developing turbulent flow characteristics show that the secondary motion ratio can be considerably larger than 2.47, depending on the streamwise location. This point has been quantified and discussed in [10].

Among the early measurements of secondary turbulent flow patterns developing in and downstream of curved pipes are the total pressure and yaw results obtained by Rowe [11] in a  $180^\circ$  bend and the attached downstream tangent. In Rowe's experiment  $R_c/D = 12$  and  $Re = 2.36 \times 10^5$ , where  $R_c$  is the bend mean radius of curvature,  $D$  its diameter and  $Re$  is the Reynolds number based on the bulk fluid velocity. An upstream tangent of length  $X/D = 69$  was used to provide a fully developed axisymmetric turbulent velocity profile at the bend inlet plane. Among Rowe's findings were that: secondary flow is most intense at about  $\theta = 30^\circ$ , as of which point the total pressure gradient induces a streamwise component of vorticity opposite in sense of rotation to the streamwise vorticity produced at the start of the bend; the curved flow is essentially fully developed past  $\theta = 90^\circ$ ; there is evidence of local reversal in the secondary flow direction along the bend symmetry plane between  $\theta = 90^\circ$  and  $X/D = 5$ .

Because of the nature of the variables measured in Rowe's study, and because of the influence of the mechanical probes used in the flow, an accurate determination of the fully developed flow streamwise location was not possible. (A combination of weak secondary motions, undetected by the yawmeter, with unchanging relatively large total pressure measurements, would certainly have given the impression of fully developed flow.) Due to experimental uncertainty, Rowe was not able to define precisely the magnitude and extent of secondary flow reversal in the vicinity of the bend symmetry plane. Although valuable for helping to understand the behavior of the mean flow, particularly in relation to inviscid effects, the pressure and yaw contours obtained by Rowe shed no light on the turbulent characteristics of the flow.

Enayet, et al. [12] have investigated developing turbulent flow in a 90° curved pipe with  $R_c/D = 2.8$  and  $Re = 43,000$ . Relatively thin boundary layers were induced at the bend inlet plane by means of a smooth contraction. The mean longitudinal (streamwise) velocity component and the corresponding turbulence intensity were measured using a laser-Doppler velocimeter. This information was supplemented by wall-pressure measurements. The relatively flat inlet velocity profile and small value of  $R_c/D$  in [12] enhanced streamwise acceleration of the flow at the inner radius wall relative to the outer wall. As a result, throughout the bend and up to  $X/D = 6$  in the downstream tangent, the maximum in the streamwise velocity component remained between the bend center line and the inner radius wall. This finding contrasts strongly with Rowe's observation that the maximum was always located between the bend center line and the outer radius wall. Because the Dean numbers of these two flows are very similar, being  $De = Re (D/R_c)^{1/2} \approx 6.8 \times 10^4$  in Rowe's bend and  $2.6 \times 10^4$  in the bend of Enayet, et al., the difference in the maximum velocity location must be due to the different inlet flow boundary layer thicknesses. A similar finding has been reported in [3] for the flow through a curved duct of square cross section.

The problem of numerical simulation of developing flow in curved pipes has been the subject of considerable research effort for the past twenty years. The extensive literature on laminar flow has been recently reviewed in [8,13]. The first serious attempt to compute turbulent flow was reported by Patankar et al. [14] who applied their three-dimensional parabolic (non-iterative) procedure to simulate Rowe's experiment. The parabolic approximation enforces, at any station, the same streamwise pressure over the whole cross section. In view of the relatively large radius ratio for the case in question, such a numerical

approximation was satisfactory over much of the bend. At the inlet to and exit from the bend, however, the sign of the pressure gradient is in fact different on the inside and outside of the bend and the adjustments to the flow that this causes cannot be mimicked by a parabolic solver.

Although for laminar flow several workers have discretized the full elliptic form of the equations of motion [15,16], provided there is no flow reversal in the streamwise direction, a semi-elliptic treatment [17] is more attractive as only the pressure field then requires storing over the solution domain. The approach was applied by its originators [17] to flow in a rectangular-sectioned bend. Recently two of the authors [18] have applied a procedure of the same type to predict turbulent flow in coils and in the 90° bend of [12]. For the former case only heat-transfer data were available for comparison; these indicated that the predictions correctly reproduced the monotonic increase in local Nusselt number from the inside to the outside of the bend, though the inner-to-outer variation was only about 60% of that measured. Agreement with the streamwise velocity profiles of [12] was broadly satisfactory, though the boundary layer development on the inside of the bend did not proceed as far towards separation as the experiment showed, nor was the rate of recovery downstream as fast. There was, moreover, some uncertainty on the degree of difficulty provided by this test case as the boundary layers were rather thin and the pressure disturbance so large that inviscid effects would have dominated over much of the flow.

#### 1.2 The Present Contribution

The above brief review has identified substantial deficiencies in our knowledge of the physics of turbulent flow through curved pipes and of the relaxation processes undergone by fluid passing from a curved to a straight pipe

section. A full understanding will require many experiments with different ratios of bend to pipe radii and different flow conditions at entry. In comparison with [18], we have selected a somewhat larger bend radius,  $180^\circ$  rather than  $90^\circ$  of turning, and a fully-developed flow at the bend entry plane. All these differences are designed to make the resultant flow pattern in the bend more strongly dependent on the turbulent stress field. Downstream of the bend, the turbulent stresses provide the only substantial agency for restoring the flow towards that associated with a straight pipe. The initial stages of this restoration have been documented at one diameter intervals.

Finally, in order to gain an impression of how successful or otherwise the widely used  $k-\epsilon$  eddy viscosity model is in predicting this flow's behaviour, the solving scheme developed in [18] has provided the basis for a numerical simulation.

## 2. THE EXPERIMENT

### 2.1 Flow System and Instrumentation

The experimental system was composed of: a water rig (described in detail in [5]), of which the most important component was the flow test section; a DISA 55X modular series laser-Doppler velocimeter and its associated electronic instrumentation; and a PDP 11/34 Digital Equipment Corporation minicomputer.

The basic components of the flow test section are shown schematically in Fig. 1. They comprised two straight pipes and a  $180^\circ$  curved pipe, constructed from transparent plexiglass. The pipe cross-section was circular throughout with a  $4.45 \text{ cm} \pm 0.02 \text{ cm}$  inner diameter ( $D$ ). The ratio of bend mean radius of curvature to pipe diameter was  $R_c/D = 3.375$ . Both tangents were of length  $X = 54.7 D$ , being respectively attached to the  $0^\circ$  (inlet) and  $180^\circ$  (outlet) planes of the bend by means of flanges. Special care was taken to avoid possible

mismatches between the component cross-sections that otherwise might disturb the flow. A stainless steel (20 mesh) screen and a 3.5 cm long flow straightening honeycomb section were placed upstream of the entrance tangent. They were held in place by a thin circular plexiglass plate. The plate was 3.175 mm thick and had 85 holes of 3.175 mm diameter arranged in a rectangular array spaced 4.495 mm on the centers in each direction. The purpose of the screen-honeycomb-plate combination was to make uniform the cross-stream plane distribution of the flow and accelerate its streamwise development.

The curved pipe section was constructed by fitting together two symmetrical half sections of plexiglass, each respectively machined on one of the two flat faces to contain the shape of a semicircular open channel. This method of construction ensured that when matched at the common symmetry plane the cross-section of the resulting curved pipe was accurately circular. When assembled, the curved pipe section had flat outer surfaces of thickness  $d = 1.48 \pm 0.02$  cm (see Fig. 1). The straight pipe sections had a circumferentially uniform wall thickness of  $0.32 \pm 0.02$  cm. The entire test section was supported horizontally by a metal frame with the bend symmetry plane parallel to the floor.

The test section was part of a closed loop through which water was made to flow by gravity from a constant head tank. From this tank the flow passed through the test section, and then into a large sump tank from where it was pumped back to the constant head tank. Flow to the head tank was controlled by a gate valve and measured using a venturi meter connected to a differential mercury manometer. The possibility of propagating disturbances through the test section was eliminated by avoiding the use of valves, sharp bends and metering devices in the test section flow loop. Flow to and from the test section tangents was channeled through 2 in (5.08 cm) i.d. gently bent tygon tube pieces. Baffles and screens located in the constant head tank served to dampen

the swirling motion of the flow leaving the tank. Residual swirl and weak secondary motions induced by the mild curvature of the tygon tube upstream of the test section were eliminated by the flow straightening section.

Measurements of the mean flow and turbulence characteristics were made using a DISA 55X modular series laser-Doppler velocimeter in backscatter mode. The system has already been described in full detail in reference [5]. A 2-watt Lexel Argon-Ion water-cooled laser was used as the light source. The laser and velocimeter optics were mounted to the top of a thick aluminum table which was itself firmly bolted to an x, y, z traversing mechanism. The traversing mechanism could displace the table top  $\pm 7.5$  cm in 5  $\mu$ m increments along any of the coordinate axes by means of three linearly encoded stepping motors monitored by the PDP 11/34 minicomputer. The minicomputer functioned as the central data acquisition and reduction controller of data validated and measured by a DISA 55L96 Doppler signal processor or "counter." Directional ambiguity in the circumferential (or tangential) velocity component was resolved by means of a Bragg cell combined with electronic downmixing.

## 2.2 Experimental Methodology

Prior to an experimental run, water was allowed to flow through the rig until it was purged of air bubbles and had attained a steady thermal state corresponding to about 20°C. Experiments were performed for two values of the bulk average velocity corresponding to  $U_b = 1.29 \pm 0.03$  m/s and  $U_b = 2.47 \pm 0.04$  m/s, respectively. During the course of an experimental run the fluid temperature rose from 18°C to 22°C, approximately. Values for the Reynolds numbers of these two flows, based on physical properties of water at 20°C, are  $Re = 57,400$  and  $110,000$ , respectively. The associated Dean numbers are  $De = 31,300$  and  $59,900$ .

The velocimeter optical probe volume was formed by the intersection of two 514.5 nm (green) light beams with a half-angle in air of  $3.28^\circ$ . The measurement volume characteristics were: a diameter of 0.1 mm, a length of 1.6 mm, and a fringe spacing of  $4.50 \mu\text{m}$  with about 18 fringes contained in the optical probe. In reality spatial filtering and threshold settings on the counter reduced the dimensions of the optical probe. The probe volume was positioned by fine control of the motorized traversing table. The details of the optical alignment procedure are provided in [10]. Cornstarch particles ranging in size from 1 to  $10 \mu\text{m}$  were added to the flow so that validated particle data rates of 1 kHz were achieved.

With a reference position established, usually on the outer surface of the test section, the computer software was activated which controlled the signal acquisition and data processing. An initial check on flow symmetry was performed at  $X/D = -2$  in the upstream tangent. Measurements of the streamwise velocity component and its normal stress at this station (half profiles are shown in Figs. 2 and 3) are in good agreement with the data of Laufer [19]. Measurements of the circumferential velocity component (not plotted) showed that it was everywhere less than  $\sim 1.5\%$  of the bulk average velocity at this station. Calculations of  $U_b$ , obtained by integrating the measured velocity distributions at  $X/D = -2$ , yielded values in good agreement (to within  $\sim 3\%$ ) with the values obtained from the venturi meter pressure drop readings.

Following the symmetry and mass flow confirmations, all subsequent measurements were restricted to vertical (radial) scans in the surface  $\phi = \pi/2$  in the symmetrical upper half of the test section. Scans were made at  $X/D = -2, -1, 1, 2, 3, 4$  and  $5$  in the straight pipes and  $\theta = 3^\circ, 45^\circ, 90^\circ, 135^\circ$ , and  $177^\circ$  in the bend. At each of these stations 15 radial positions were probed, starting at the centerline and moving in increments of  $1.5 \text{ mm}$  toward the wall, with a 16th

position fixed at 0.7 mm from the inside pipe wall. At each measurement point the mean velocity and normal stress were statistically determined from populations of 1 to 3 samples consisting of 1,000 individual measurements each. More than 90% of all the measurements consisted of at least 2 samples per point. Each individual measurement was required to satisfy the counter 5/8 validation comparison to within a preset tolerance of 6%. At every validation of a Doppler burst a "data ready" signal was issued by the counter to a logic conversion circuit. This circuit then sent a triggering pulse to the computer parallel line interface module which was checked for data availability by a software loop approximately every 20  $\mu$ s.

Although the velocimeter is capable of two-component measurements, curvature of the test section surfaces precluded dual-channel operation. Values for the streamwise component of the mean and fluctuating velocities,  $U$  and  $u'$ , were derived from measurements obtained with the probe volume fringes aligned normal to the longitudinal coordinate direction. Values for the circumferential components,  $V$  and  $v'$ , were obtained through a rotation of the optics by  $90^\circ$ , thus placing the fringes normal to the circumferential component direction.

Because of the large positive magnitudes of the streamwise velocity component, frequency shifting was unnecessary for measurements of this component. By contrast, the circumferential velocity component exhibited low magnitudes, with signs both positive and negative. To resolve this directional ambiguity, a net frequency shift of 500 kHz was imposed using a DISA 55N10 Bragg cell combined with electronic downmixing.

### 2.3 Measurement Error

Error sources affecting the accuracy (systematic error) and precision (random error) of laser-Doppler measurements have been discussed in [20-22]. In

this study the most serious potential systematic errors were attributed to probe volume positioning, velocity gradient broadening and velocity bias, respectively. The main sources of random error affecting the precision of the measurements were due to: a) statistical sampling uncertainty (due to the finite size of sample populations); and b) uncertainty in the determination of the normalizing bulk average velocity,  $U_b$ . Estimates of the first uncertainty were derived from the measurements themselves. For both mean velocity components, this uncertainty was always less than  $\pm 2-3\%$  (rms error), while for the turbulence intensities it was always less than  $\pm 2-5\%$ . The error in  $U_b$  was  $\pm 2\%$  and arose principally from uncertainties in the manometer pressure readings.

The initial probe volume location uncertainty was estimated to be half the effective probe volume length, or  $\pm 0.5$  mm approximately. This error is altered as the beams traverse the pipe because of changes in index of refraction (at the air/plexiglass and plexiglass/water interfaces) and wall curvature effects. To calculate the actual probe volume location, and to estimate the uncertainty in this location, it is necessary to know the relevant trigonometric relations. These are derived in [10]. The relations depend on the velocity component of interest and on the shape of the surfaces at the measurement station in question. In regions of surface curvature, both the probe volume location and the half angle between the beams in water depend non-linearly on the probe volume virtual radial location (the location in air). Calculations of the error incurred in  $\gamma$ , the half angle of the beams in water, due to a  $\pm 0.5$  mm positioning error in the initial probe volume location showed that this source of inaccuracy was negligible. Similarly, calculations showed that the initial positioning uncertainty was only significant very near the pipe walls, in regions with steep field gradients. Thus, estimates of the maximum (absolute) systematic errors in the measurements obtained nearest the walls gave:  $\sim 4\%$  for

$U/U_b$ ;  $\sim 10\%$  for  $u'/U_b$ ;  $\sim 15\%$  for  $V/U_b$ , and  $\sim 10\%$  for  $v'/U_b$ . In the bulk of the flow all these errors were significantly less than  $\sim 2\%$ .

Velocity gradient broadening has been analyzed by Melling [23] who proposed a simple method for estimating its magnitude. For the conditions of this study, gradient broadening in the measurements was estimated to be less than 1% everywhere in the flow.

Various weighting methods have been proposed to correct for the velocity bias effect [21,22], but none of these is entirely satisfactory. They all involve assumptions regarding the statistical distribution of particles in the flow. In addition, the corrections can be influenced by the problem of "incomplete-signal bias." The use of the weighting scheme proposed by McLaughlin and Tiederman [24], in which the particle residence time is taken to be inversely proportional to the modulus of the measured velocity, was investigated in this study. For the longitudinal velocity component, differences between weighted and unweighted data sets were relatively small (less than 1%). For the circumferential component the differences were much larger, with the weighted data giving a less realistic (overdamped) picture of the flow field. The reason for this is attributed to an overcorrection in the weighting scheme which, for the circumferential component, amounts to a disproportionate weighting of slow moving particles. This occurs as a consequence of taking the particle residence time as  $t_{res} \sim V^{-1}$  instead of  $t_{res} \sim (U^2 + V^2 + W^2)^{-1/2}$ . The latter, more accurate, weighting could not be performed with the present single component measurement system.

For turbulence intensities less than 10% Drain [21] shows that velocity bias corrections of the mean and r.m.s. velocities should not amount to more than  $\sim 2\%$ . In this study the measured turbulence intensities never exceed  $\sim 12\%$ . As a result, plots of the unweighted data only are presented here. Listings of both weighted and unweighted measurements are provided in [10].

### 3. THE COMPUTATIONAL METHOD

The numerical procedure developed by the authors to predict laminar or turbulent flow in pipe bends has been described in [13,18]. Here, therefore, we simply summarize its main features.

The method is based on a semi-elliptic discretization of the Reynolds equations expressed in toroidal coordinates in which the three components of velocity and the static pressure form the set of dependent variables. Following the methodology of the TEACH family of computer programs, [25], a finite-volume approach to forming the difference equations is adopted with a staggered mesh for the different dependent variables. The quadratic upstream weighted approximation is adopted for convective transport, [26], while a modified version of Patankar's SIMPLER algorithm [27] is used to secure a pressure field in compliance with the continuity equation.

Although in a shear flow as complex as this one might well expect to have to adopt some non-equilibrium, non-isotropic model of turbulence to secure close agreement with experiment, the (relative) computational simplicity of using isotropic effective diffusion coefficients persuaded us that in this study the turbulent stresses should be obtained by the standard  $k-\epsilon$  model [18,28]. However, in place of the wall functions that usually provide a link between near-wall velocities and shear stresses and supply effective boundary conditions for the turbulence energy ( $k$ ) and its viscous dissipation ( $\epsilon$ ), a fine mesh has been incorporated to cover the viscous sublayer and "buffer" regions. In this sub-region we have for simplicity adopted the mixing-length hypothesis using van Driest's [29] damping function. Of course, to resolve accurately the very rapid variation of effective transport coefficients across this near-wall sublayer a fine mesh is required. In order that this requirement should not impose a

substantial core penalty, the variation of pressure across the sublayer was obtained by radial equilibrium (instead of by continuity); the technique, known as PSL, is described in [30].

Computations were made over the semi-circular cross section bounded by the plane of symmetry passing through the center of the pipe and the bend center. Starting inlet profiles were obtained by computing the development of the flow in a straight pipe over a distance of 53 diameters. The downstream profiles of the dependent variables were then used as the inlet profiles for the computation of the U-bend flow at a position 2 diameters upstream of the bend. The mesh comprised 28 radial and 24 uniformly-spaced circumferential nodes mapping the semi-circular section and 160 streamwise planes. This mesh density has been found from our previous work to give essentially grid independent results<sup>1</sup> when used with the third-order accurate quadratic upstream approximation for convection. The computations extended a total of 8 diameters into the tangent downstream of the bend where, at the exit plane, zero-streamwise gradient constraints were applied to all variables. Successive streamwise passes over the domain were made until momentum and mass residuals summed over all planes were below 1% of the entering momentum and mass flow rates. Convergence required about 6 hours cp time on a Cyber 205 (with an unvectorized code) though in practice only very small changes resulted over the second half of the computation.

\*\*\*\*\*

<sup>1</sup>For example, in [18] an increase in the number of radial nodes from 28 to 40 altered the predicted level of Nusselt number by less than 1%.

#### 4. RESULTS AND DISCUSSION

Measurements of the longitudinal ( $U/U_b$ ) and circumferential ( $V/U_b$ ) velocity components and their respective turbulence intensities ( $u'/U_b$ ,  $v'/U_b$ ) are shown in Figs. 2-3. Only the data at the lower Reynolds number ( $Re = 57,400$ ) are here included. Except for relatively small differences, the dimensionless profiles show that flow development is essentially the same at  $Re = 110,000$  [10]. This is an important point since all the calculations reported here were performed for  $Re = 65,000$  (with  $Rc/D = 3.375$ ). Tabulations of the measurements are available in [10].

The  $U$  and  $u'$  component measurements at  $X/D = -2$  show good agreement with the developed flow measurements obtained by Laufer [19] in a straight pipe. At  $X/D = -2$  the  $V$  component is less than (+)  $0.015 U_b$  (not plotted). However, at  $X/D = -1$  and  $\theta = 3^\circ$ , the  $V$  component is  $\sim (+) 0.04 U_b$ . With reference to the coordinate system in Fig. 1, this implies that the inlet flow is gradually (but only slightly) accelerated towards the inner radius of the pipe, a result expected from potential flow theory and previously observed by others.

In the first half of the bend ( $\theta = 3^\circ$  to  $90^\circ$ ), the  $U$ -profiles show the core of the streamwise flow losing speed while the flow near the wall accelerates.  $V$ -profiles at corresponding stations reveal the development of a strong secondary flow. This secondary flow is induced by the transverse pressure gradient set up between the outer ( $r_o$ ) and inner ( $r_i$ ) wall regions of the bend. In the pipe center, it works to overcome and reverse the sense of the cross-stream motion in the inlet flow. Near the wall the original sense of cross-stream motion is preserved and intensified, with  $(V/U_b)_{\max} \sim 0.30$  at  $\theta = 45^\circ$ . Nevertheless, the levels of secondary flow found in the present study are lower than those obtained in a square sectioned duct for equivalent curvature ratio and entering flow conditions [5].

Between  $\theta = 45^\circ$  and  $135^\circ$  the V-profiles reveal a striking feature of the flow. In the fluid core,  $r/(D/2) < 0.5$ , the cross-stream flow undergoes a second reversal in its sense of motion and is redirected towards the pipe inner radius. As a result, a region of negative cross-stream flow (directed from  $r_i$  towards  $r_o$ ) is trapped between the core and the wall; for example,  $V/U_b \sim -0.06$  at  $\theta = 135^\circ$ . Between  $\theta = 135^\circ$  in the bend and  $X/D = 5$  in the downstream tangent, the region of negative cross-stream flow gradually disappears. Notwithstanding, an imprint of its presence remains in all the subsequent V-profiles.

The occurrence of a second cross-stream flow reversal past  $\theta = 90^\circ$  in the bend supports the concept proposed by Rowe [11], that each symmetrical half section of the bend develops two counter-rotating vortical structures. The more intense of the two, located between the pipe wall and the core of the flow, preserves the sense of cross-stream motion induced by the transverse pressure gradient at the start of the bend. The smaller, weaker, structure is mainly confined to the core and is attributed to the formation of a transverse pressure gradient opposite in sign to that at the start of the bend.

The present mean flow measurements place on a firm quantitative basis the interpretation by Rowe of his total pressure and yaw measurements. However, in contrast to Rowe's results, the V-profiles provided here show that fully developed mean flow conditions are not established in the present bend.

The computed distribution of longitudinal velocity shown in Fig. 2 actually mirrors very closely the measured development. Only at  $90^\circ$  is there a discernible difference between the two, the experiments indicating a larger dip in velocity at the axis. This measure of agreement, while encouraging, at least partly reflects that the mean velocity profile along this  $\phi = \pi/2$  surface does not offer a particularly sensitive test. This is not the case with the second-

dary flow shown in Fig. 2. The computations do not reproduce as strong an increase in the  $V$  velocity component, directed towards the inside of the bend, as the data at  $X/D = -1$  and  $\theta = 3^\circ$ . However they do predict very well the strong, single-cell secondary flow that develops by  $45^\circ$ . They also capture broadly the way the "return" flow near the mid-plane is brought to a halt and reverses by  $135^\circ$ . Interestingly, the computations suggest that the sign of the secondary velocity on the symmetry plane reverses yet again at  $177^\circ$  and at one diameter downstream. While the measurements at  $177^\circ$  still show marginally positive  $V$  for small  $r$ , the sign of the acceleration is evidently correct. The differing development of the secondary flow at different radial positions is brought out in Fig. 4 which shows the progress of  $V/U$  on the  $\pi/2$  surface at  $2r/D = 0.75$  and at the pipe axis. The flow reversals exhibited by the measurements are generally well captured by the numerical computation, at least within the bend itself.

A more complete picture of the computed flow development in the U-bend is provided in Fig. 5 which shows both the secondary flow vectors in the cross-sectional plane and the streamwise flow contours. The modifications that the former bring to the latter are readily discernible. Particularly interesting are the  $90^\circ$  and  $135^\circ$  contours where the maximum streamwise velocity is displaced off axis (as in the experiment, Fig. 2), and those at  $177^\circ$  where the contours  $U/U_b = 0.8$  and  $1.0$  show clearly the effect of the reversal of the secondary flow on the mid-plane. In Fig. 5,  $R$  and  $L$  are respectively the bend radius of curvature and length of the pipe "centerline" measured from the inlet plane.

Downstream of the bend the computations do not mimic the steady cross-stream movement of fluid towards the side of the pipe corresponding with the inside of the bend (Fig. 3). This reflects a significantly too slow recovery of the computed streamwise velocity from the strong adverse pressure gradient that

the fluid on the inside of the bend encounters at the bend exit. Computations for the 90° bend of Enayet [18] with precisely the same model show a similar too slow recovery. It is also relevant to mention that several groups adopting the same (or a very similar) turbulence model to compute the flow downstream of the reattachment point behind a backward-facing step for the 1981 Stanford Conference also found a too sluggish recovery [31]. The behaviour here predicted thus seems an endemic feature of the model that needs to be removed.

In flow through a straight pipe, the circumferential normal stress is approximately equal to the arithmetic mean of the other two components. Accordingly, on Fig. 3, showing the measured distribution of  $v'$ , have been added the profiles of  $\sqrt{2k/3}$  using the  $k$ -levels generated by the computations. As expected, at the inlet there is close agreement between computation and measurement. There is, moreover, reasonably close agreement between the two over the whole flow domain. We note, however, that measured levels of  $v'$  are rather higher than those computed near the wall between 45° and 177°. This difference, we believe, arises mainly from the direct generation of  $\overline{v^2}$  by the strongly sheared secondary flow (i.e., large  $\partial v/\partial r$ ); although generation of  $k$  by this agency also appears in the turbulence energy transport equation, it is a less important process there. At 90° and 135° the computed levels of  $\sqrt{2k/3}$  are lower than the measured levels of  $v'$  over the whole radius by amounts ranging from 1 to 30%. It seems likely that at these positions the computed energy dissipation rate,  $\epsilon$ , has become too large, preventing the rise in fluctuating velocity levels that the experimental values indicate. The experimental values of  $v'$  decrease markedly beyond the bend exit, and the subsequent downstream development shows remarkable agreement between the computations and the measurements.

Plots of the ratio  $v'/u'$ , a measure of turbulent flow anisotropy, are given in [10]. The results suggest that, between  $X/D = -1$  and  $\theta = 90^\circ$ , near the outer

radius wall, the term  $-\overline{vw} \partial V / \partial r$  contributes strongly to the generation of  $\overline{v^2}$ . Beyond  $\theta = 90^\circ$  this contribution decreases, allowing dissipation and redistribution mechanisms to reduce the level of  $\overline{v^2}$  near the wall, as observed.

#### 5. CONCLUDING REMARKS

This study places on a firm quantitative basis some of Rowe's [11] qualitative interpretations of the behaviour of turbulent flow through a  $180^\circ$  curved pipe. Specifically, the existence of two cross stream flow reversals has been confirmed both experimentally and by the numerical simulations. The results support the notion of an additional (symmetrical) pair of counter-rotating vortical structures embedded in the core of the flow within the curved pipe. The levels of secondary flow are on the whole lower than in the corresponding square duct flow [5]. This underlines the dominant effect of the flat walls in the curved square duct in driving the secondary motion. No cross-stream flow reversals were measured in the latter case, which further indicates how different are the structures in what superficially appear to be two very similar flows.

The rms level of velocity fluctuations is substantially raised as the flow passes around the bend due to the additional mean strain associated with the turning of the primary flow and, particularly, the secondary-flow velocity gradients thus created. There are, in addition, changes in the structure of the turbulent field in the core - notably the large increase of streamwise fluctuations at  $90^\circ$  and the rise in  $v'$  observed between  $135^\circ$  and  $177^\circ$  - whose cause cannot be unravelled with any certainty from measurements on the  $\phi = \pi/2$  surface alone.

The numerical simulations have reproduced with a gratifying degree of fidelity the measured evolution of the flow. It strengthens the impression formed in [5] that often the  $k-\epsilon$  eddy viscosity model does better in simulating really

complex flows, such as those found within the 180° bend, than it does in less strongly perturbed flows. For example, in the present case the prediction of the flow recovery downstream of the bend shows the largest disagreement with the measured behavior even though secondary velocities are there very weak. No general conclusions may be drawn, however, for computations of the square bend with the same model of turbulence used here [32,33] display spectacular disagreement with the data of [5].

Future work on bend flows needs to be aimed at providing a more complete mapping of the primary and secondary mean flow and stress distributions over the entire conduit cross-section. This data should help in clarifying the role of the additional pair of vortical structures in curved pipe flow and the relaxation process occurring in the downstream tangent.

#### ACKNOWLEDGEMENTS

The experimental work at the University of California, Berkeley, was initially supported by the Office of Naval Research through Contract Number N 00014-80-C-0031 and, more recently, by the Office of Fossil Energy of the U.S. Department of Energy under Contract Number DE-AC03-76SF00098. The computational work at UMIST was also sponsored by the U.S. Office of Naval Research through Grant Number N00014-83-G-0021. We are grateful to these agencies for their respective support. Thanks go to Ms. Loris C-H Donahue for the typing of this manuscript. The authors' names are listed in alphabetical order.

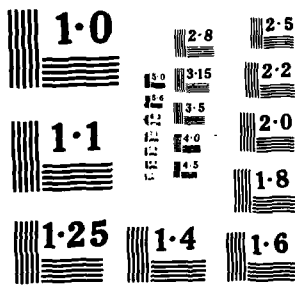
## REFERENCES

1. Humphrey, J.A.C., Whitelaw, J.H. and Yee, G. "Turbulent flow in a square duct with strong curvature," J. Fluid Mech., 103, pp. 443-463, 1981.
2. Enayet, M.M., Gibson, M.M. and Yianneskis, M. "Measurements of turbulent developing flow in a moderately curved square duct," Int. J. Heat and Fluid Flow, 3, No. 4, pp. 221-224, 1982.
3. Taylor, A.M.K.P., Whitelaw, J.H. and Yianneskis, M. "Curved ducts with strong secondary motion: velocity measurements of developing laminar and turbulent flow," J. Fluids Engng., 104, pp. 350-359, 1982.
4. Anderson, B.H., Taylor, A.M.K.P., Whitelaw, J.H. and Yianneskis, M. "Developing flow in S-shaped ducts," Proc. Int. Symposium on Applications of Laser-Doppler Anemometry to Fluid Mechanics, Lisbon, July 1982.
5. Chang, S.M., Humphrey, J.A.C. and Modavi, A. "Turbulent flow in a strongly curved U-bend and downstream tangent of square cross-sections," PhysicoChemical Hydrodynamics, 4, No. 3, pp. 243-269, 1983.
6. Rojas, J., Whitelaw, J.H. and Yianneskis, M. "Flow in sigmoid diffusers of moderate curvature," Proc. Fourth Symposium on Turbulent Shear Flows, Karlsruhe, FDR, September 1983.
7. Brunn, H.H., "An experimental investigation of secondary flow losses in bends with rectangular cross sections," Department of Engineering, Report CUED/A-Turbo/TR 95, University of Cambridge, 1979.
8. Berger, S., Talbot, L. and Yao, L.-S. "Flow in curved pipes," Ann. Rev. Fluid Mech., 15, pp. 461-512, 1983.
9. Cuming, H.G. "The secondary flow in curved pipes," NPL, UK, Reports and Memoranda, No. 2880, February 1952.
10. Azzola, J. and Humphrey, J.A.C. "Developing turbulent flow in a 180° curved pipe and its downstream tangent," Report LBL-17681, Materials and Molecular Research Division, Lawrence Berkeley Laboratory, University of California, 1984.
11. Rowe, M. "Measurements and computations of flow in pipe bends," J. Fluid Mech., 43, pp. 771-783, 1970.
12. Enayet, M.M., Gibson, M.M., Taylor, A.M.K.P. and Yianneskis, M. "Laser-Doppler measurements of laminar and turbulent flow in a pipe bend," Int. J. Heat and Fluid Flow, 3, pp. 211-217, 1982.
13. Humphrey, J.A.C., Iacovides, H. and Launder, B.E. "Some numerical experiments on developing laminar flow in circular-sectioned bends," J. Fluid Mech., 154, 357, 1985.

14. Patankar, S.V., Prapat, V.S. and Spalding, D.B. "Prediction of laminar flow and heat transfer in helically coiled pipes," *J. Fluid Mech.* 62, 539, 1974.
15. Humphrey, J.A.C. "Numerical calculation of developing laminar flow in pipes of arbitrary curvature radius," *Can. J. Chem. Eng.* 56, 151, 1978.
16. Soh, W.Y. and Berger, S.A. "Laminar entrance flow in a curved pipe," *J. Fluid Mech.*, 148, 109, 1984.
17. Prapat, V.S. and Spalding, D.B. "Numerical computations of the flow in curved ducts," *Aero. Quart.*, 26, 219, 1974.
18. Iacovides, H. and Launder, B.E., "The computation of momentum and heat transport in turbulent flow around pipe bends," *Proc. 1st UK National Heat Transfer Conference, Vol. 2, 1097, I. Chem. Engrs. Symposium Series 86*, 1984.
19. Laufer, J. "The structure of turbulence in fully developed pipe flows," *NACA Technical Report No. 1174*, 1954.
20. Durst, F., Melling, A. and Whitelaw, J.H. "Principles and Practice of Laser-Doppler Anemometry," Academic Press, London, 1976.
21. Drain, L.E. "The Laser Doppler Technique," John Wiley and Sons Ltd., New York, 1980.
22. Buchave, P. "The measurement of turbulence with the burst-type laser-Doppler anemometer - errors and correction methods," Ph.D. Thesis, State University of New York at Buffalo, 1979.
23. Melling, A. "Investigation of flow in non-circular ducts and other configurations by laser-Doppler anemometry," Ph.D. Thesis, University of London, 1975.
24. McLaughlin, D.K. and Tiederman, W.G. "Biasing correction for individual realization of laser anemometer measurements in turbulent flows," *Physics of Fluids*, 16, pp. 2082-2088, 1973.
25. Gosman, A.D. and Ideriah, F.J.K. TEACH-2E: A general computer program for two-dimensional, turbulent recirculating flows," *Mech. Eng. Dept., Imperial College*, 1976.
26. Leonard, B. "A stable and accurate convective modelling procedure based on quadratic upstream interpolation," *Com. Meth. Appl. Mech. Engrg.* 19, 59, 1979.
27. Patankar, S.V. Numerical Heat Transfer and Fluid Flow, Hemisphere, 1980.
28. Launder, B.E. and Spalding, D.B. "The numerical computation of turbulent flows," *Comp. Meth. Appl. Mech. Engrg.* 3, 269, 1974.

29. van Driest, E.R. "On turbulent flow near a wall," J. Aero Sci. 23, 1007, 1956.
30. Iacovides, H. and Launder, B.E. "PSL - An economical approach to the numerical analysis of near-wall elliptic flows," ASME J. Fluids Engrg. 106, 245, 1984.
31. Kline, S.J., Cantwell, R. and Lilley, G. (editors) Proc. AFOSR-HTTM-Stanford Conference on Complex Turbulent Flows, Stanford University 1982.
32. Chang, S.M., Humphrey, J.A.C., Johnson, R.W. and Launder, B.E. "Turbulent momentum and heat transport in flow through a 180° bend of square cross-section," Proc. 4th Turbulent Shear Flow Symposium, Karlsruhe, 1983.
33. Choi, Y.D. Personal Communication, 1984.





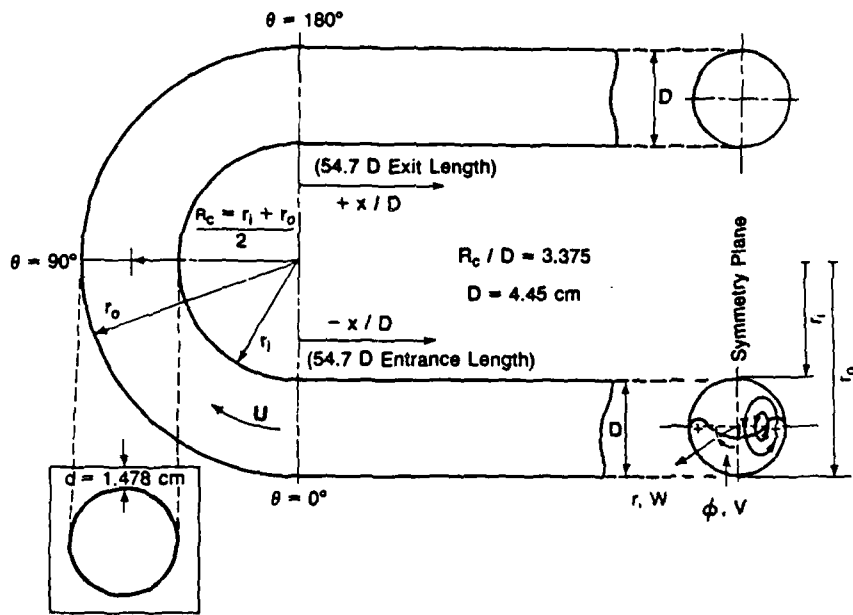


Fig. 1 The test section configuration and definition of coordinate system.

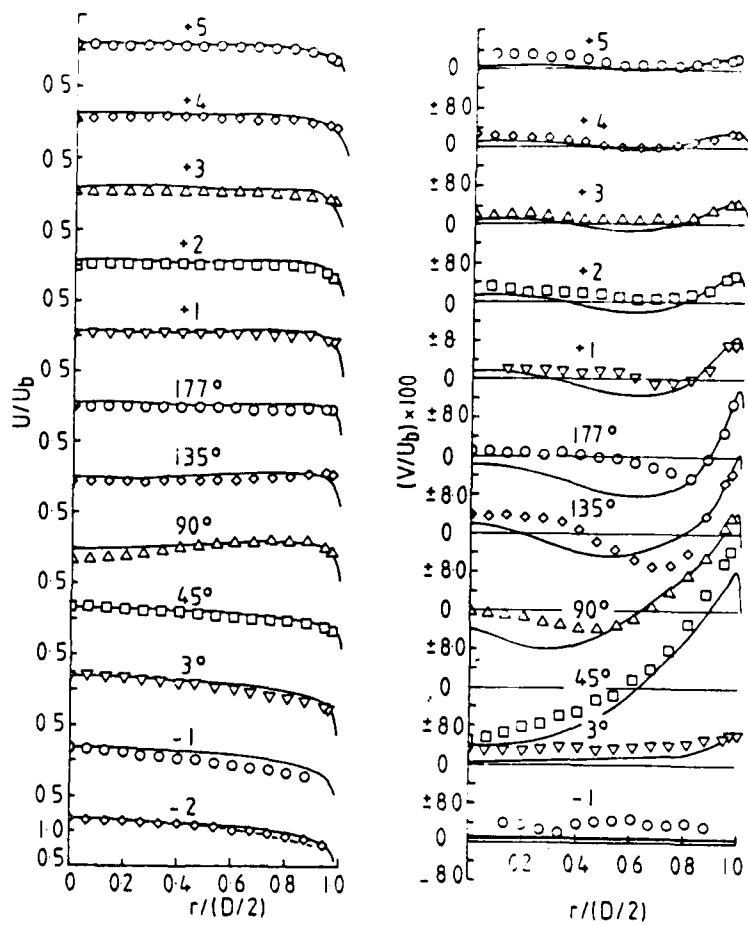


Fig. 2 Measurements (points) and calculations (continuous lines) of the longitudinal ( $U$ ) and circumferential ( $V$ ) mean velocity components at sequential longitudinal stations in a  $180^\circ$  curved pipe with straight tangents. Dashed line at  $X/D = -2$  corresponds to Laufer's [19] developed flow data.

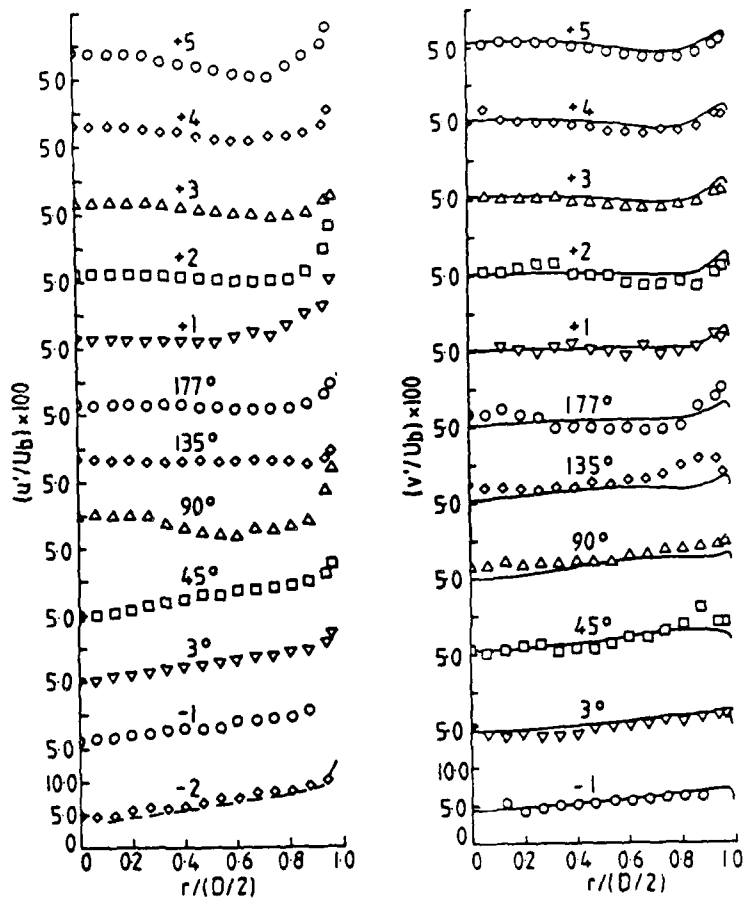


Fig. 3 Measurements (points) and calculations (continuous lines) of the longitudinal ( $u'$ ) and circumferential ( $v'$ ) turbulence intensity components at sequential longitudinal stations in a  $180^\circ$  curved pipe with straight tangents. Dashed line corresponds to Laufer's [19] developed flow data. In the calculations  $u' = v' = (2k/3)^{1/2}$ .

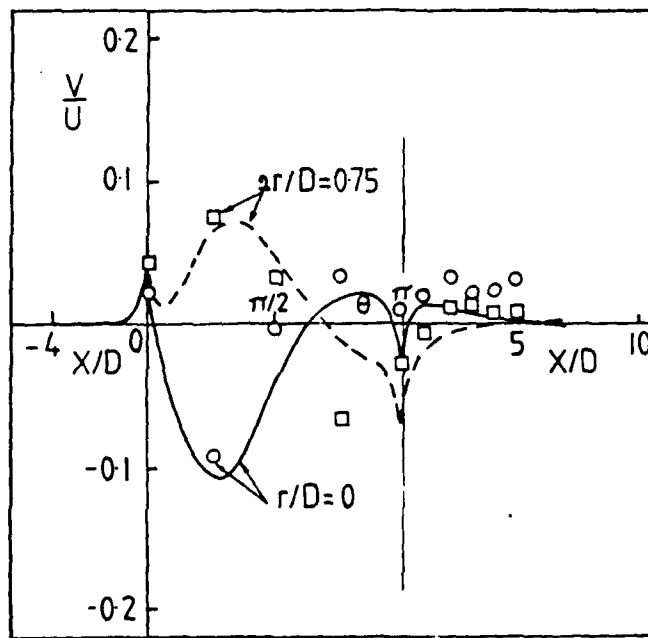
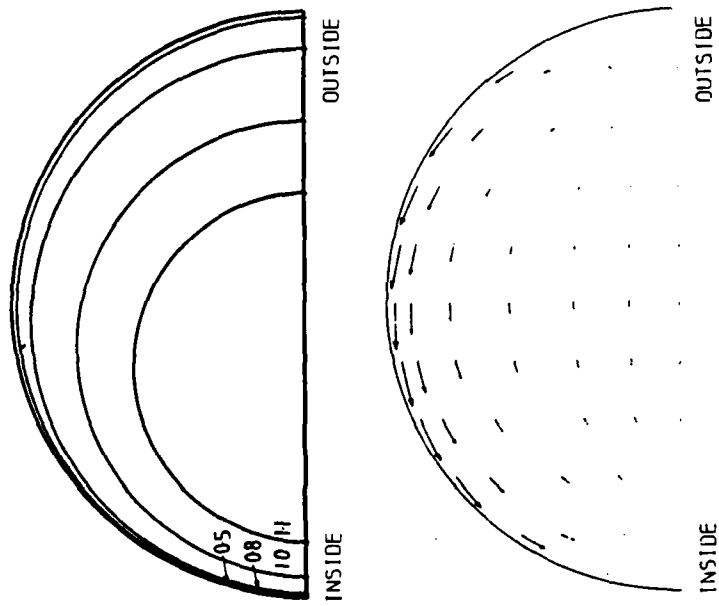
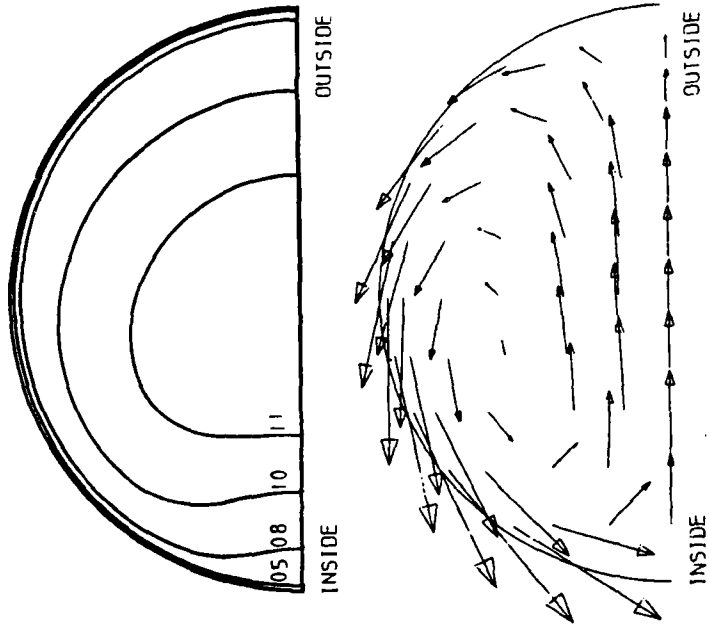


Fig. 4. Measurements (points) and calculations (lines) of developing secondary flow at two radial locations contained in the symmetry plane,  $\phi = \pi/2$ , of a  $180^\circ$  curved pipe with straight tangents.



(L/R) = 0.35 ;  $\theta = 3^\circ$



(L/R) = 5.30 ;  $\theta = 45^\circ$

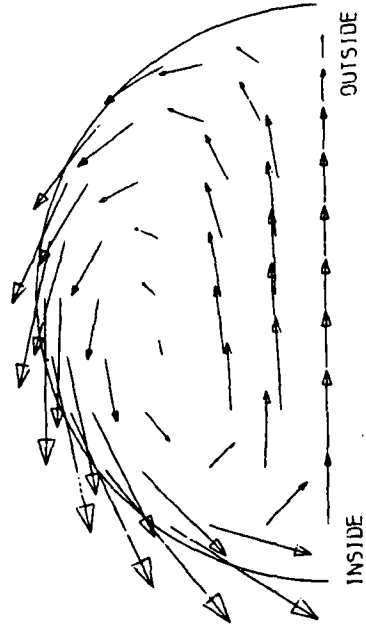
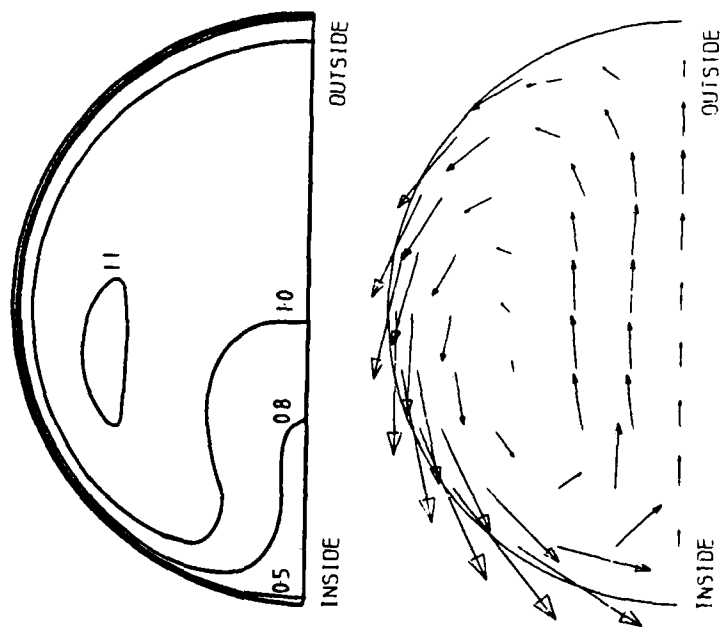
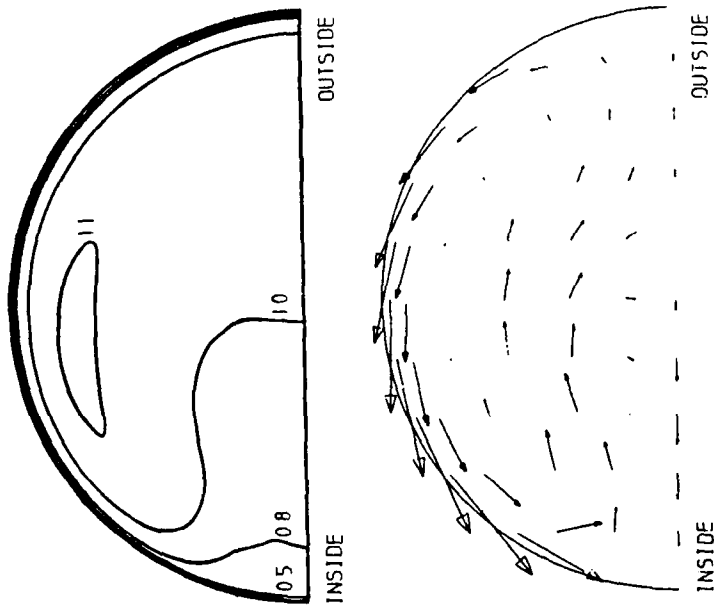


Fig. 5. Calculated flow development in a 180° curved pipe with straight tangents. Top figures show streamwise (U) velocity component contours. Bottom figures show cross-stream vector velocities. In bottom figures, 0.10 D corresponds to 0.08  $u_b$ .



(L/R) = 10.60 ;  $\theta = 90^\circ$



(L/R) = 15.91 ;  $\theta = 135^\circ$

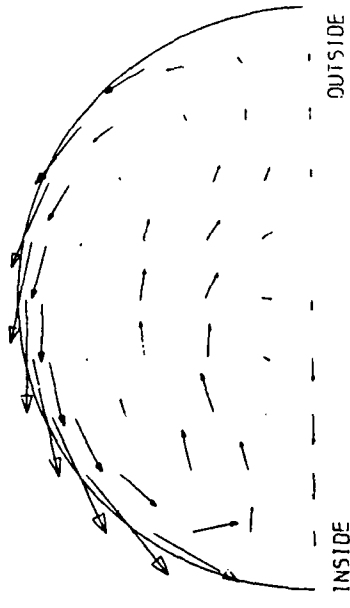
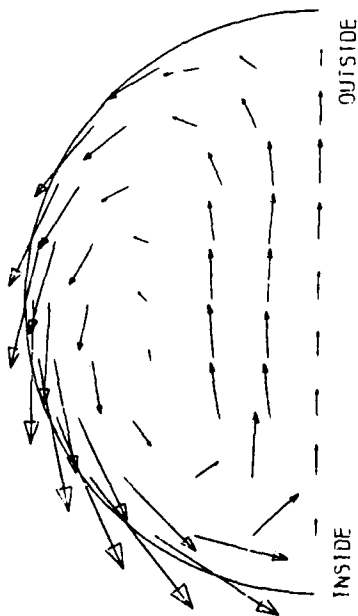
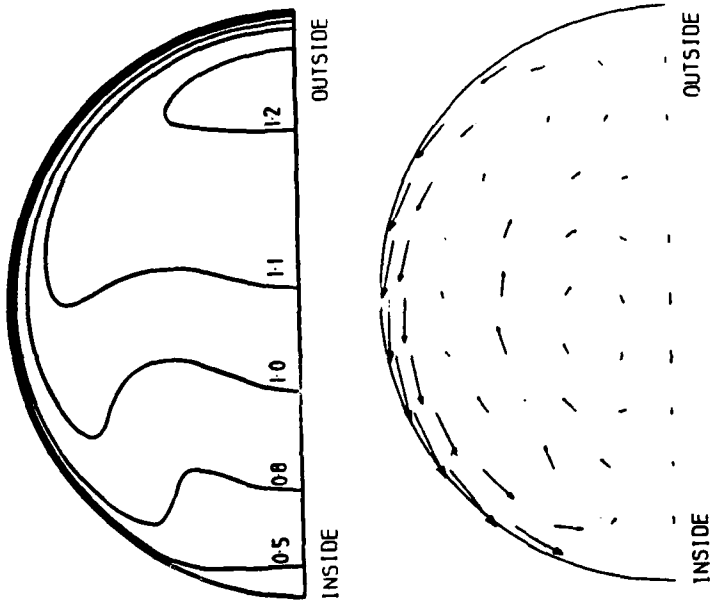
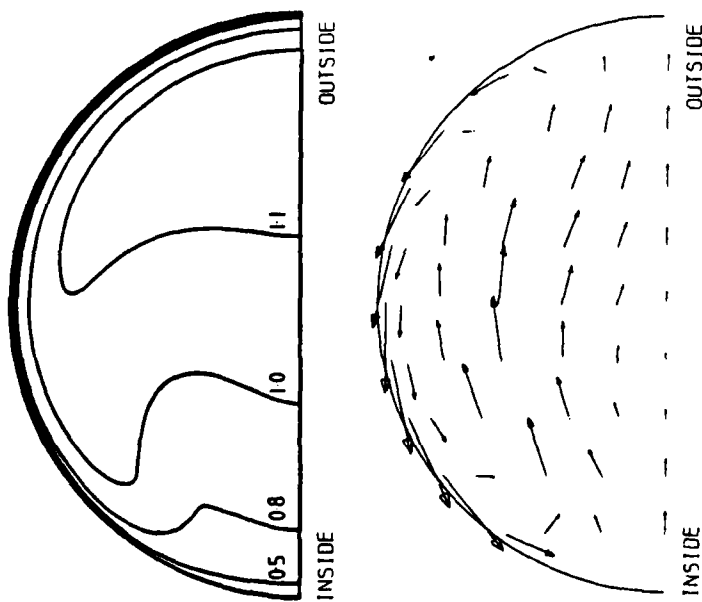


Fig. 5. Calculated flow development in a 180° curved pipe with straight tangents. Top figures show streamwise (U) velocity component contours. Bottom figures show cross-stream vector velocities. In bottom figures, 0.10 D corresponds to 0.08  $U_b$ .

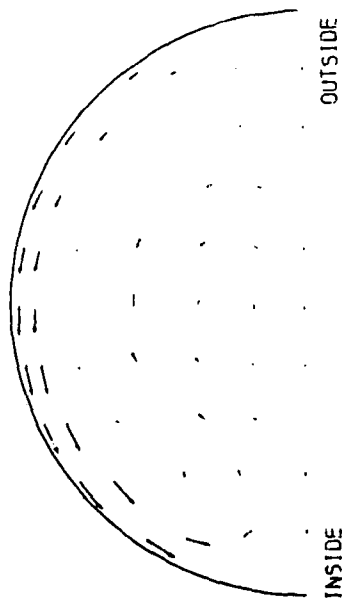
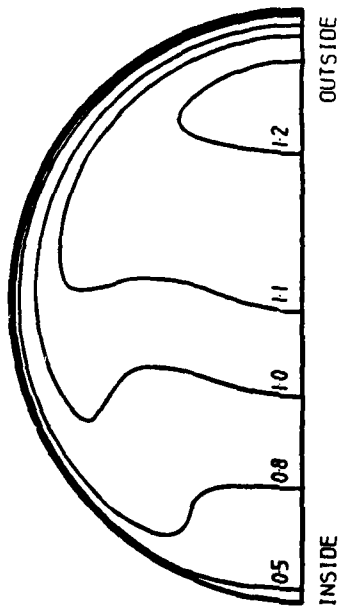


(L/R) = 23.21 ; X/D = 1

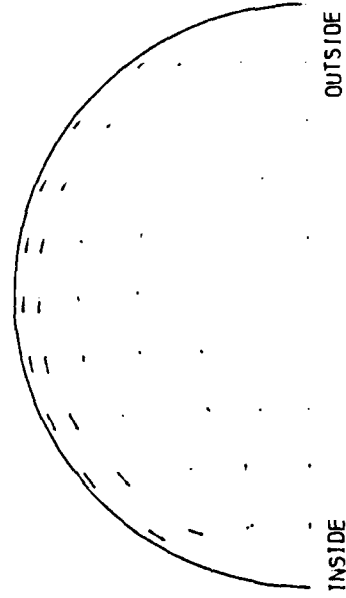
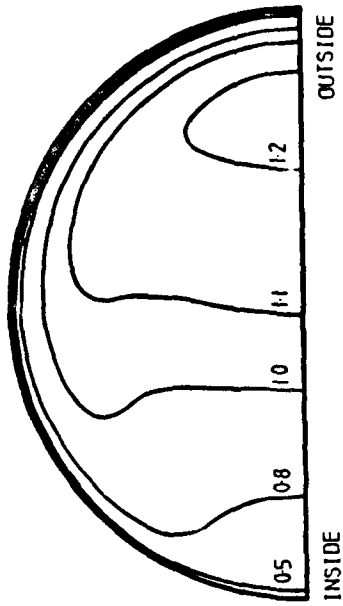


(L/R) = 20.95 ;  $\theta = 177^\circ$

Fig. 5. Calculated flow development in a 180° curved pipe with straight tangents. Top figures show streamwise (U) velocity component contours. Bottom figures show cross-stream vector velocities. In bottom figures, 0.10 D corresponds to 0.08  $U_b$ .



(L/R) = 27.21 ; X/D = 3



(L/R) = 31.21 ; X/D = 5

Fig. 5. Calculated flow development in a 180° curved pipe with straight tangents. Top figures show streamwise (U) velocity component contours. Bottom figures show cross-stream vector velocities. In bottom figures, 0.10 D corresponds to 0.08  $u_b$ .

Proc. 4th Int. Conf. on Numerical Methods in  
Laminar and Turbulent Flow, pp.1023-1045,  
Swansea, July 9-12, 1985

ASM PREDICTIONS OF TURBULENT MOMENTUM AND HEAT TRANSFER IN  
COILS AND U-BENDS

Author's Name Here

H. Iacovides and B.E. Launder  
Mechanical Engineering Department,  
UMIST, Manchester M60 1QD

FIRST The paper describes the incorporation of an algebraic stress model (ASM) of turbulence into an accurate semi-elliptic solution procedure for the Reynolds equations and the corresponding energy equation. Particular attention is given to the devices necessary to procure convergent behaviour. Applications of the approach are reported to the computation of fully-developed flow in coils and of flow developing in U-bends. Generally encouraging agreement with the experimental data is obtained though the computations do not mimic the partial laminarization that appears to occur in the strong acceleration on the inside of the bend at inlet.

1. INTRODUCTION

The numerical simulation of developing turbulent flow through tightly curved pipes poses a number of problems concerning both the physics - the model for turbulent transport - and the numerics. The flow is highly three-dimensional, for the centripetal acceleration of the sheared streamwise flow induces a strong secondary motion with peak velocities 30% or more of the bulk streamwise velocity. In fact, the secondary flow is strongest very close to the pipe walls where cross currents steadily carry fluid from the outside to the inside of the bend. This feature means that the near-wall velocity profile is unlikely to conform closely with the usual semi-logarithmic law. Accordingly, the normal practice of making the velocity field comply not with the no-slip boundary condition at the wall but with the semi-logarithmic profile at some appropriate distance from it needs to be abandoned.

This need accentuates the problem of sheer numerical resolution. For example, to compute the turbulent flow around a U-bend without substantial numerical error requires, with 3rd-order quadratic upwind differencing and a fine near-wall mesh to resolve the viscous sublayer, the velocities to

Start running headline here

be computed at some 50 thousand points in the domain. With such a large number of mesh points it is not routinely possible to store in core all the dependent variables (pressure, three velocity components and usually two turbulence-characterizing parameters). Fortunately, if streamwise flow recirculation is absent, a semi-elliptic treatment may be adopted in which only the pressure is stored over the whole domain while the values of all other variables are held just on two adjacent cross-sectional planes. This approach, developed by Prataap and Spalding [1], has been applied to flow around square bends by its originators [1], Chang et al [2], and Birch [3] and to laminar and turbulent flow through circular-sectioned pipes by the authors [4,5,6].

Author's comment here

The computational results for turbulent flow presented in ref[5] were based on a two-region turbulence model. Over most of the flow the widely used  $k-\epsilon$  eddy viscosity model (EVM) was adopted, the value of the turbulent viscosity at any point being obtained from local values of the turbulence energy ( $k$ ) and its dissipation rate ( $\epsilon$ ). Very near the wall, however, where viscous effects become of direct importance, Van Driest's version of the mixing-length hypothesis was used. The resultant computations displayed fairly satisfactory agreement with experiment although systematic differences were nevertheless evident. Predictions of local heat transfer coefficient, while giving a mean level broadly in line with experiment, exhibited a too small variation between the inside and outside of the bend. Qualitatively this shortcoming was foreseen. Eddy viscosity schemes are known not to capture correctly the strong damping or augmentation of turbulence associated with streamline curvature [7].

Now, in simpler, two-dimensional strains it is well established that turbulence models based on the Reynolds stress transport equations *do* succeed fairly well in mimicking the observed strong effects of curved streamlines in the turbulent stresses. Our objective in the work reported hereunder has thus been to incorporate one of these higher level turbulence models into the solving procedure developed in ref [5]. We use what is known as an "algebraic stress model" (ASM) which truncates the Reynolds stress transport equations to a direct algebraic connection between the local Reynolds stresses and the local strain field - though that connection is far more intricate than with eddy viscosity models.

This enhancement of turbulence model has necessitated major changes to the way the solution procedure is organized in order to secure convergent behaviour. An account of the novel practices introduced is given. In view of length limits on the paper, aspects of the procedure which remain unchanged from our earlier work [4,5,6] are summarized only

Start running headline here  
briefly. Comparisons are drawn in Section 4 with the available experimental data and with computations generated with the k~ε EVM.

2. THE MATHEMATICAL AND PHYSICAL MODEL

2.1 The Describing Mean Flow Equations

The Reynolds equations describing the motion of an incompressible, stationary, turbulent flow in toroidal coordinates, Figure 1, may be expressed

$$\rho \{ C(\Psi) + S_c(\Psi) \} = D(\Psi) - \rho \{ R(\Psi) + S_R(\Psi) \} + S_D(\Psi) + S_P(\Psi) \quad (1)$$

where Ψ stands for any of the components of mean velocity U (azimuthal, φ), V (radial, r) or W (streamwise, θ). The quantities C, D and R denote the convection, molecular-diffusion and turbulent-diffusion operators

$$C(\Psi) \equiv \frac{1}{rr_c} \left\{ \frac{\partial}{\partial \phi} (r_c U \Psi) + \frac{\partial}{\partial r} (rr_c V \Psi) + \frac{\partial}{\partial \theta} (r W \Psi) \right\}$$

$$D(\Psi) \equiv \frac{1}{rr_c} \left\{ \frac{1}{r} \frac{\partial}{\partial \phi} \left( r_c \mu \frac{\partial \Psi}{\partial \phi} \right) + \frac{\partial}{\partial r} \left( rr_c \mu \frac{\partial \Psi}{\partial r} \right) + \frac{1}{r_c} \frac{\partial}{\partial \theta} \left( r \mu \frac{\partial \Psi}{\partial \theta} \right) \right\}$$

$$R(\Psi) \equiv \frac{1}{rr_c} \left\{ \frac{\partial}{\partial \phi} r \overline{u \Psi} + \frac{\partial}{\partial r} rr_c \overline{v \Psi} + \frac{\partial}{\partial \theta} r \overline{w \Psi} \right\}$$

where ψ refers to the fluctuating velocity component in the same direction as Ψ and r<sub>c</sub> is the local radius from the centre of the bend (R + r<sub>c</sub> cos θ), R being the mean bend radius. (When considering flow in straight tangent sections to a bend R is set to some appropriately large value).

The remaining source terms in eq(1) are set out in Table 1.

Equation (1) also describes the mean energy equation for low-speed flow with Ψ now standing for temperature, T (and ψ the fluctuating temperature, t). In that event, C(Ψ) and R(Ψ) retain precisely the same form as for the velocity components while in D(T) the viscosity μ is replaced by μ/σ, σ denoting the fluid Prandtl number. In the energy equation the residual sources are all zero.

2.2 The Turbulence Models

(a) The high Reynolds number region : From the pipe axis to a radius equal to 96% of the pipe radius one of two turbulence models are adopted, the standard k~ε eddy viscosity model (EVM) and an algebraic stress model (ASM).

Start running headline here

$\Psi$	$S_c(\Psi)$	$S_R(\Psi)$	$S_P(\Psi)$
U	$\frac{VU}{r} + \left\{ \frac{W \cdot \sin \phi}{r_c} \right\}$	$\frac{uu}{r} + \left\{ \frac{\bar{w}^2 \cdot \sin \phi}{r_c} \right\}$	$-\frac{1}{r} \frac{\partial P}{\partial \phi}$
V	$-\frac{U^2}{r} - \left\{ \frac{W^2 \cos \phi}{r_c} \right\}$	$-\bar{u}^2 - \left\{ \frac{\bar{w}^2 \sin \phi}{r_c} \right\}$	$-\frac{\partial P}{\partial r}$
W	$\left\{ \frac{VW \cos \phi - UW \sin \phi}{r_c} \right\}$	$\left\{ \frac{uw \cos \phi - uw \sin \phi}{r_c} \right\}$	$-\frac{1}{r_c} \frac{\partial P}{\partial \theta}$
	$S_D(\Psi)$		
U	$\frac{1}{r^2 r_c} \frac{\partial}{\partial \phi} \left\{ r_c \mu \left( \frac{\partial U}{\partial \phi} \right) + 2V \right\} + \frac{1}{r r_c} \frac{\partial}{\partial r} \left\{ r_c \mu \left( \frac{\partial V}{\partial \phi} - U \right) \right\} + \mu \frac{\partial}{\partial r} \frac{U}{r}$ $+ \frac{\mu}{r^2} \frac{\partial V}{\partial \phi} + \frac{1}{r} \frac{\partial}{\partial \theta} \left\{ \mu \frac{\partial}{\partial \phi} \left( \frac{W}{r_c} \right) \right\} - \frac{2\mu \sin \phi}{r_c^2} \left\{ U \sin \phi - V \cos \phi - \frac{\partial W}{\partial \theta} \right\}$		
V	$\frac{1}{r_c} \frac{\partial}{\partial \phi} \left\{ r_c \mu \frac{\partial}{\partial r} \left( \frac{U}{r} \right) \right\} + \frac{1}{r r_c} \frac{\partial}{\partial r} \left\{ r r_c \mu \frac{\partial V}{\partial r} \right\} - \frac{2\mu}{r^2} \left\{ \frac{\partial U}{\partial \phi} + V \right\}$ $+ \frac{1}{r} \frac{\partial}{\partial \theta} \left\{ r \mu \frac{\partial}{\partial r} \left( \frac{W}{r_c} \right) \right\} + \frac{2\mu \cos \phi}{r_c^2} \left\{ U \sin \phi + V \cos \phi - \frac{\partial W}{\partial \theta} \right\}$		
W	$\frac{1}{r r_c} \frac{\partial}{\partial \phi} \left\{ \mu \left( \frac{\partial U}{\partial \theta} + W \sin \phi \right) \right\} + \frac{1}{r r_c} \frac{\partial}{\partial r} \left\{ 2\mu r \left( \frac{\partial V}{\partial \theta} - W \cos \phi \right) \right\}$ $+ \frac{1}{r^2} \frac{\partial}{\partial \theta} \left\{ \mu \left( \frac{\partial W}{\partial \theta} - 2U \sin \phi + 2V \cos \phi \right) \right\} - \frac{\mu \sin \phi}{r} \frac{\partial}{\partial \phi} \left\{ \frac{W}{r_c} \right\}$ $+ \mu \cos \phi \frac{\partial}{\partial r} \left( \frac{W}{r_c} \right) - \frac{\mu r \sin \phi}{r_c^2} \frac{\partial}{\partial \theta} \left( \frac{U}{r} \right) - \mu \frac{\cos \phi}{r_c^2} \left\{ \frac{\partial V}{\partial \theta} \right\}$		

Table 1

Last line here

Start manuscript page here

The EVM adopts the Newtonian stress-strain law

$$-\overline{u_i u_j} = \nu_t \left( \frac{\partial U_i}{\partial x_j} + \frac{\partial U_j}{\partial x_i} \right) \quad (2)$$

( $u_i$  and  $U_i$  denoting fluctuating and mean velocities) where the turbulent viscosity is expressed in terms of the turbulent kinetic energy  $k$  and its rate of dissipation  $\epsilon$ :

$$\nu_t = 0.09 k^2 / \epsilon$$

TITLE OF PAPER HERE  
and  $k$  and  $\epsilon$  are obtained from transport equations as described below. The turbulent heat fluxes  $\overline{u_i t}$  are likewise obtained from

Author's Appointment - 
$$-\overline{u_i t} = \frac{\nu_t}{\sigma_T} \frac{\partial T}{\partial x_i} \quad (3)$$

where  $\sigma_T$ , the turbulent Prandtl number for energy diffusion, is taken as 0.9.

The ASM adopted in this study is essentially the usual isotropization-of-production closure with Rodi's [8] transport hypothesis

$$\frac{(\overline{u_i u_j} - \frac{2}{3} k \delta_{ij})}{k} = \frac{(1 - c_2)}{(c_1 - 1 + P/\epsilon)} \left[ \frac{P_{ij} - \frac{2}{3} P \delta_{ij}}{\epsilon} + (\phi'_{ij1} + \phi'_{ij2}) \right] \quad (4)$$

In equation (4)  $P_{ij}$  is the stress generation rate by mean strain

$$P_{ij} = - \left( \overline{u_i u_k} \frac{\partial U_j}{\partial x_k} + \overline{u_j u_k} \frac{\partial U_i}{\partial x_k} \right) \text{ and } P \equiv \frac{1}{2} P_{kk}$$

$\phi'_{ij1}$  and  $\phi'_{ij2}$  are wall-proximity functions accounting for pressure reflections from the rigid walls of the pipe. We adopt the forms suggested by Shir [9] and Gibson and Launder [10]

$$\phi'_{ij1} = c_1 \frac{\epsilon}{k} \left( \overline{u_k u_m} n_k n_m \delta_{ij} - \frac{3}{2} \overline{u_i u_k} n_k n_j - \frac{3}{2} \overline{u_j u_k} n_i n_k \right) f \left( \frac{\ell}{x_N} \right)$$

$$\phi'_{ij2} = c_2 \left( \phi_{km2} n_k n_m \delta_{ij} - \frac{3}{2} \phi_{ik2} n_k n_j - \frac{3}{2} \phi_{jk2} n_k n_i \right) f \left( \frac{\ell}{x_N} \right)$$

where 
$$\phi_{ij2} \equiv -c_2 \left( P_{ij} - \frac{2}{3} \delta_{ij} P \right)$$

$n_k$  is the unit vector normal to the wall,  $x_N$  is the normal distance from the wall and  $\ell$  is the turbulent length scale  $0.38 k^{3/2} / \epsilon$  (the numerical coefficient being chosen so that in an equilibrium near-wall layer the quantity  $\ell/x_N$  is unity. The function  $f(\ell/x_N)$  was simply taken as  $\ell/x_N$  by Gibson and Launder.

Reference [10] had proposed the above form for a turbulent shear flow near an infinite plane surface (the atmospheric boundary layer). The problem of how to adapt the approach to apply, with any degree of rigour, within a toroidal enclosure is a difficult one that we have not attempted to address here. We have for simplicity retained the form given above merely replacing

$$\text{TITLE OF PAPER } x_N^{-1} \text{ by } \left[ (a - r)^{-1} - (a + r)^{-1} \right]$$

where  $a$  is the pipe radius. Close to the wall the second term in square brackets makes only a small contribution compared with the first which conforms with our expectation that turbulence there should know little about the overall geometry of the cross section. At the axis, however, the two terms cancel thus removing any wall correction. This feature is necessary when working within the framework of the indicated model for otherwise at  $r = 0$  we should get different values for  $u^2$  and  $v^2$ . While not regarding the above simple expedient with much satisfaction, it is our impression that its weaknesses are not having a great effect on the calculated flow and thermal behaviour.

To calculate the turbulent heat fluxes we have adopted the generalized gradient diffusion hypothesis:

$$\overline{u_i - \bar{t}} = -c_t \frac{k}{\epsilon} \overline{u_i u_k} \frac{\partial T}{\partial x_k} \quad (5)$$

where, following Johnson [11], the constant  $c_t$  was taken to be 0.35. This relatively simple formulation is at least a more generally valid statement than eq(3) since it gives rise to non-isotropic diffusivities and, indeed, can produce heat fluxes in directions where there is no temperature variation. A recent experimental paper by Tavoularis and Corrsin [12] has helped underline the importance of this feature.

The turbulent scalars  $k$  and  $\epsilon$  are obtained from the usual transport equations which in toroidal coordinates become:

$$\rho C(k) = D(k) + S_D(k) + P - \epsilon \quad (6)$$

$$\rho C(\epsilon) = D(\epsilon) + S_D(\epsilon) + c_{\epsilon 1} \frac{\epsilon P}{k} - c_{\epsilon 2} \frac{\epsilon^2}{k} \quad (7)$$

where the  $C$  operator is the same as in eq(1) while, in the case of the ASM treatment, the  $D$  and  $S_D$  operators take a common form for both  $k$  and  $\epsilon$ :

$$D(\psi) = \frac{c_w}{r r_c} \left\{ \frac{1}{r} \frac{\partial}{\partial \phi} \left( r_c \frac{k}{\epsilon} \overline{u^2} \frac{\partial \psi}{\partial \phi} \right) + \frac{\partial}{\partial r} \left( r r_c \frac{k}{\epsilon} \overline{v^2} \frac{\partial \psi}{\partial r} \right) + \frac{1}{r_c} \left( r \frac{k}{\epsilon} \overline{w^2} \frac{\partial \psi}{\partial \theta} \right) \right\}$$

----- Last line here ----->

Start from the following

$$S_D(\psi) = \frac{c_k}{r r_c} \left\{ \frac{\partial}{\partial \phi} \left[ r_c \frac{k}{\epsilon} \left( \overline{uv} \frac{\partial \psi}{\partial r} + \frac{\overline{uw}}{r_c} \frac{\partial \psi}{\partial \theta} \right) \right] + \frac{\partial}{\partial r} \left[ r r_c \frac{k}{\epsilon} \left( \frac{\overline{uv}}{r} \frac{\partial \psi}{\partial \phi} + \frac{\overline{vw}}{r_c} \frac{\partial \psi}{\partial \theta} \right) \right] + \frac{\partial}{\partial \theta} \left[ r \frac{k}{\epsilon} \left( \frac{\overline{vw}}{r} \frac{\partial \psi}{\partial \phi} + \overline{vw} \frac{\partial \psi}{\partial r} \right) \right] \right\}$$

The diffusion coefficients for k and ε (i.e.  $c_k$  and  $c_\epsilon$ ) are assigned the values 0.22 and 0.15, again in line with standard practice.

In the case of the EVM the diffusion 'sources' of k and ε,  $S_D(\psi)$ , are zero and the diffusion operator  $D(\psi)$  takes the same form as for the mean velocity component with  $u$  replaced by  $(\mu + \rho v_r / \sigma_\psi)$ . The turbulent Prandtl numbers for turbulent energy ( $\sigma_k$ ) and energy dissipation ( $\sigma_\epsilon$ ) take the values 1.0 and 1.22.<sup>k</sup>

The turbulent energy generation rate P is given by:

$$P \equiv - \left\{ \overline{u^2} \left( \frac{1}{r} \frac{\partial U}{\partial \phi} + \frac{V}{r} \right) + \overline{v^2} \frac{\partial V}{\partial r} + \overline{w^2} \left( \frac{1}{r_c} \frac{\partial W}{\partial \theta} + \frac{V \cos \phi - U \sin \theta}{r_c} \right) + \overline{vw} \left( \frac{\partial W}{\partial r} - \frac{W \cos \phi}{r_c} + \frac{1}{r_c} \frac{\partial V}{\partial \theta} \right) + \overline{uw} \left( \frac{1}{r_c} \frac{\partial U}{\partial \theta} + \frac{1}{r_c} \frac{\partial W}{\partial \phi} + \frac{W \sin \theta}{r_c} \right) + \overline{uv} \left( \frac{1}{r} \frac{\partial V}{\partial \phi} + \frac{\partial U}{\partial r} - \frac{U}{r} \right) \right\} \quad (8)$$

When the EVM is adopted, eq(2) is substituted into (8) so that only mean velocity gradients and the turbulent viscosity arise in evaluating P.

(b) The low-Reynolds-number region : In the immediate vicinity of the wall viscous effects on the turbulent transport processes become substantial. Although low-Reynolds-number forms of the  $k \sim \epsilon$  EVM were available (e.g. [13]), the handling of the k and ε equations in the viscosity affected layers is fairly tricky. Thus, in view of the heavy burden that our calculations would inevitably place on our computing resources, a simpler scheme was adopted. In axisymmetric boundary layer flows near spinning surfaces it is known [14] that Prandtl's mixing length hypothesis with Van Driest's [15] damping function leads to a broadly satisfactory description of the momentum and heat transport processes. Accordingly, in the annular ring  $0.96 < r/a \leq 1.0$  it is assumed that

Start running headline here

Start normal page here

$$v_t = \ell_m^2 \left[ \left( \frac{\partial U_i}{\partial x_j} \right)^2 \right]^{1/2} \quad (9)$$

where the mixing length  $\ell_m$  varies with distance  $y$  from the pipe wall as

$$\ell_m = 0.419 y (1 - \exp(-\rho y U_\tau / 26 \mu))$$

The turbulent Prandtl number for heat transfer is again taken as 0.9.

### 3. DISCRETIZATION AND SOLUTION

#### 3.1 General Strategy

A complete presentation of the procedure developed for solving the system of equations introduced in §2 is given by Iacovides [16]. In the next sub-section we focus on the methods for handling the Reynolds stresses when the ASM is adopted; these represent the principal innovations of this paper so far as the numerics are concerned. Although the introduction of the ASM has necessitated a major restructuring of the code, the same broad solution strategy evolved for use with EVMS (and described in more detail in refs[4], [5] and [6]) has been retained. Namely:

- A finite-volume, primitive-variable decomposition using the now customary staggered mesh in which the nodes for velocity are located on the boundaries of the scalar nodes (p, T, k and ε).
- The use of QUICK [17] for approximating convective transport of all variables in the cross-stream (r-φ) plane.
- The adoption of a 'semi-elliptic' treatment in which all dependent variables except p are stored on just two adjacent r-φ planes, with values being successively transferred from the downstream to the upstream register as each streamwise iteration is made.
- The use of Patankar's SIMPLER algorithm [18] for obtaining the pressure field in compliance with the continuity equation. Some adaptation of the original scheme was needed to incorporate it in a semi-elliptic framework.
- The employment of PSL [19] over a thin band near the wall (which for convenience we take to coincide

9

Start printing here

with the region where the mixing-length scheme is used for computing turbulent viscosities) in which the pressure is obtained from radial equilibrium (rather than continuity) and where, in consequence, three-dimensional storage of  $p$  is not required.

The  $180^\circ$  U-bend computations (both ASM and EVM) have evaluated the dependent variables on a 24 (azimuthal) x 28 (radial) x 160 (streamwise) mesh. Of the radial nodes, 8 were located in the PSL region. Convergence was flagged when the sum of the absolute mass residuals for each control volume was reduced below 1%. This degree of convergence was secured after approximately 100 streamwise iterations over the domain.

### 3.2 Treatment of the Reynolds Stresses

(a) Location of the stresses : The Reynolds stresses lie on a mesh staggered with respect to the velocity nodes as indicated in Figure 2. This choice promotes stability and leads to a minimum the amount of interpolation. Notice, for example, that, located where it is, the shear stress  $\overline{vw}$  lies on the boundary of both a W control volume and a V control volume where it is needed in applying the force momentum principle to these velocity components. Likewise  $\overline{vw}$  is generated (in part) by the differences in both the V and W velocities at the nodes straddling the shear stress.

(b) Pseudo-viscosity tensor and residual stress : Over the whole region in which the ASM is applied the viscous diffusion terms play an insignificant role; the equations are source-term dominated, the sources (and sinks) being the Reynolds stresses. In an EVM treatment, of course, the stresses are re-expressed in terms of a viscosity times a mean strain, introducing into the difference equations a strong coupling between the velocities at one point and those at surrounding nodes. This linkage decisively improves the stability of the equation set.

With an ASM the intercoupling among the sources is vastly more complex and, based on experience in much simpler two-dimensional flows, attempts to solve the equations by treating the Reynolds stresses entirely as explicit sources and sinks would not have led to convergence. Accordingly, a (fairly) strong implicit coupling among neighbouring velocities is created by introducing a pseudo-viscosity tensor  $\hat{u}_{ij}$ . In the  $U_i$  momentum equation, the value of  $\hat{u}_{ij}$  is simply the magnitude of the coefficient multiplying  $\partial U_i / \partial x_j$  in the ASM expression for  $\overline{u_i u_j}$ . For the toroidal coordinate system adopted, the components of the pseudo-viscosity are given in Table 2. The part of the Reynolds stress not accounted for through the pseudo-viscosity is termed the "residual stress",  $\hat{u}_{ij}$ , the components of which, for

i \ j	1	2	3
1	$\frac{2\rho\alpha(2+\phi_2)k\bar{u}^2}{3\epsilon}$	$\frac{\rho(1+\frac{3}{2}\phi_2)k\bar{u}^2}{(\frac{1}{\alpha}+\frac{3}{2}\phi_1)\epsilon}$	$\frac{\rho\alpha k\bar{u}^2}{\epsilon}$
2	$\frac{\rho(1+\frac{3}{2}\phi_2)k\bar{v}^2}{(\frac{1}{\alpha}+\frac{3}{2}\phi_1)\epsilon}$	$\frac{2\rho(1+2\phi_2)k\bar{v}^2}{(\frac{1}{\alpha}+\frac{3}{2}\phi_1)\epsilon}$	$\frac{\rho(1+\frac{3}{2}\phi_2)k\bar{v}^2}{(\frac{1}{\alpha}+\frac{3}{2}\phi_1)\epsilon}$
3	$\frac{\rho\alpha k\bar{w}^2}{\epsilon}$	$\frac{\rho(1+\frac{3}{2}\phi_2)k\bar{w}^2}{(\frac{1}{\alpha}+\frac{3}{2}\phi_1)\epsilon}$	$\frac{2\rho\alpha(2+\phi_2)k\bar{w}^2}{3\epsilon}$

$$\alpha \equiv (1-c_2)/(c_1-1+P/\epsilon); \quad \phi_1 = \left(\frac{c_1}{1-c_2}\right) f\left(\frac{y}{x_N}\right); \quad \phi_2 = \frac{c_2 c_2}{1-c_2} f\left(\frac{y}{x_N}\right)$$

Table 2 Components of Pseudo Viscosity Tensor  $\bar{\mu}_{ij}$ 

i \ j	1	2	3
1	$\bar{u}^2 - \bar{\mu}_{11} \frac{\partial U}{r\partial\phi}$	$\bar{u}\bar{v} - \bar{\mu}_{12} \frac{\partial v}{r\partial\phi}$	$\bar{u}\bar{w} - \bar{\mu}_{13} \frac{\partial w}{r\partial\phi}$
2	$\bar{u}\bar{v} - \bar{\mu}_{21} \frac{\partial u}{\partial r}$	$\bar{v}^2 - \bar{\mu}_{22} \frac{\partial v}{\partial r}$	$\bar{v}\bar{w} - \bar{\mu}_{23} \frac{\partial w}{\partial r}$
3	$\bar{u}\bar{w} - \bar{\mu}_{31} \frac{\partial u}{r\partial\theta}$	$\bar{v}\bar{w} - \bar{\mu}_{31} \frac{\partial v}{r\partial\theta}$	$\bar{w}^2 - \bar{\mu}_{33} \frac{\partial w}{r\partial\theta}$

Table 3 Residual Stress Tensor  $\bar{u}_{ij}$

completeness, are given in Table 3. The residual stresses can be accommodated as sources and sinks in the equations without provoking divergence.

(c) Generation term treatment : Although it is physically possible for interactions among the turbulent stresses and mean strains to lead to negative "generation" rates of turbulence energy, in practical shear flows this occurs only, if at all, in limited regions and the magnitude of this extra sink of turbulence energy is so small as to be an unimportant contributor to the energy balance in the region in question. In an iterative numerical solution there is no guarantee that during the progress of iteration substantial negative generation rates will not occur, however. When they do, a very rapid divergence can result. This behaviour has been reported by others who have usually restored convergence by setting P to zero whenever negative values arise. This practice proved ineffective in the present study, however. The problem arises not just from the kinetic energy and dissipation rate equations where P appears as a source. The anisotropy of the Reynolds stresses is directly sensitive to the value of P/ε and it is this sensitivity that is the most damaging to securing convergence. The problem has been removed by the following treatment. We define a residual turbulence energy generation P̃ as

$$\tilde{P} \equiv P - P_{EVM}$$

where  $P_{EVM}$  is the value of the turbulence energy generation given by an eddy-viscosity approximation of the Reynolds stresses, viz

$$P_{EVM} = \frac{1}{2} \frac{c_{11} k^2}{\epsilon} \left( \frac{\partial U_i}{\partial x_j} + \frac{\partial U_j}{\partial x_i} \right)^2$$

While  $P_{EVM}$  is always positive,  $\tilde{P}$  may be positive or negative. In evaluating the Reynolds stresses from the ASM equations the dimensionless parameter  $P/\epsilon$  is replaced by  $P'/\epsilon'$  where

$$P' = P_{EVM} + \text{Max}(\tilde{P}, 0)$$

$$\epsilon' = \epsilon + \text{Max}(-\tilde{P}, 0)$$

Thus, when  $\tilde{P}$  is positive,  $P'/\epsilon'$  is identical to  $P/\epsilon$  while negative residual generations augment the dissipation term. In the kinetic energy equation  $P'$  and  $\epsilon'$  likewise replace  $P$  and  $\epsilon$  while, in the dissipation rate equation, if  $\tilde{P}$  is negative the source/sink terms become

$$\underbrace{c_{\epsilon 1} P_{EVM} \epsilon/k}_{\text{source}} - \underbrace{(c_{\epsilon 2} \epsilon - c_{\epsilon 1} \tilde{P}) \epsilon/k}_{\text{sink}}$$

Last line here

Start the main heading here

Although *algebraically* the  $k$  and  $\epsilon$  equations are unchanged by this rearrangement, there are implied differences in the numerical processing since, following long established practice, source terms are handled explicitly while sink terms are treated implicitly.

(d) Solution of the algebraic stress equations : Perhaps the obvious way to handle the six coupled algebraic equations for the Reynolds stresses would be to solve the  $6 \times 6$  matrix at each point in the flow. One may recognize, however, that there are distinct differences between the role of the diagonal and off-diagonal elements. For a given node location the three diagonal elements (the normal stresses) are located at a coincident point while the off-diagonal terms (the shear stresses) are scattered. Moreover, the normal stresses can physically never be negative - and must not be allowed to become so during progress towards a solution for that would produce negative components of pseudo-viscosity (Table 2).

For these and other reasons we have followed the practice of Huang and Leschziner [20] in handling the normal and shear stresses separately<sup>(I)</sup>. However, because of the strong coupling between the shear and normal stresses, direct solution of the two  $3 \times 3$  matrices is not viable. Instead, a successive-substitution approach has been adopted. Iacovides [16] provides a detailed account of the steps; here we simply summarize the main points. At every point on an  $r-\phi$  plane the three normal stresses are obtained, explicitly using values of (the other) Reynolds stresses from the corresponding node on the upstream plane and current-plane values of other dependent variables. Initially just that single iteration is made at any plane; this limitation is applied not just because there is little merit in obtaining very precise values for the turbulent stresses while the momentum and continuity equations are far from converged, but also because such attempts to obtain more accurate stresses actually slow convergence - and on occasions have caused divergence. The three shear stresses are determined next in much the same way. As, with successive streamwise passes over the solution domain, the residuals in the mean field variables become small, first one and then two additional iterations are made on the Reynolds stresses at each point. Because of the large number of streamwise planes (160) the change in Reynolds stress over a single forward step is usually only a few percent. Thus, the use of the upstream value gives an initial estimate of each stress component that is quite close to the actual solution; only a few iterations

I. Huang and Leschziner have been concerned with two-dimensional flows in which only one shear stress component is non-zero.

where  
here

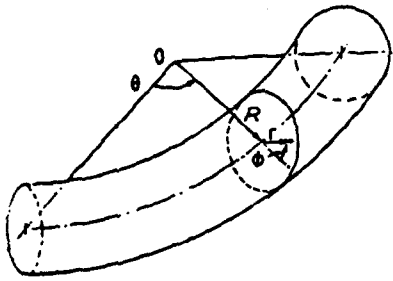


Fig. 1 The configuration considered and the describing coordinates

LOADING HERE  
HERE

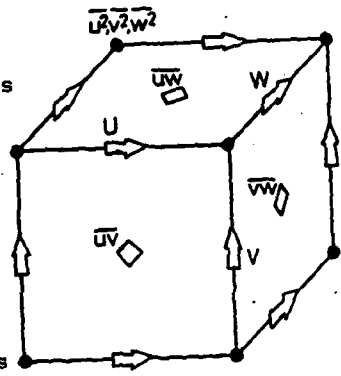


Fig. 2 Relative location of velocities and Reynolds stresses

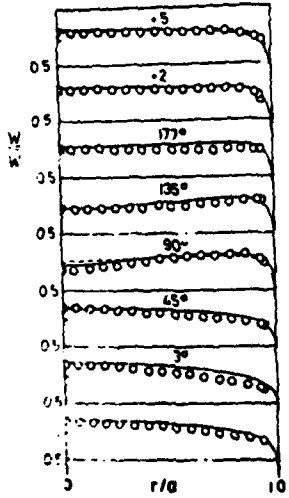


Fig. 3 Streamwise velocity distribution along  $\phi = 90^\circ$   
 Measurements [21]  
 — 45M computation;  
 --- 64M computation

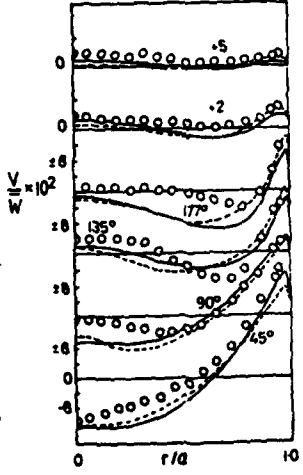


Fig. 5 Circumferential velocity along  $\phi = 90^\circ$ . Key as Fig. 3.

Start running heading here

are therefore required.

3.3 Boundary Conditions

For the case of the U-bend, the velocity and turbulence profiles at inlet appropriate to fully-developed flow were prescribed. These were obtained by running the code for the case of a straight pipe. At exit the only constraint applied was on pressure where the streamwise gradient was taken uniform over the pipe cross section.

At the pipe wall all velocity components were set to zero. The turbulence energy and its dissipation rate were not solved in the low-Reynolds-number region. However, at the interface between this sublayer and the fully turbulent core, effective values of  $k$  and  $\epsilon$  were obtained by setting equal to the turbulence energy generation rate (given by the mixing length hypothesis) and requiring that the viscosity given by the mixing length and  $k\sim\epsilon$  formulae should be the same.

The value of the circumferential velocity  $U$  was set to zero along the symmetry plane while the gradient of all other dependent variables was set to zero. References [4] and [5] describe the procedure for handling the symmetry at the pipe centre.

4. PRESENTATION AND DISCUSSION OF RESULTS

Comparisons are here limited to the 180°-bend experiments undertaken by Azzola and Humphrey [21] and the authors [22] and to the heat transfer data of flow in a coil by Seban and McLaughlin [23]. A fuller set of comparisons is given by Iacovides [16]. The reader is referred to ref [4] and [5] which show excellent agreement with data of various laminar flows, thus providing an indication that numerical errors are small with the discretization practices and mesh densities here adopted. Although the turbulent flow transport equations using an ASM are far more complicated than for laminar flow, substantial grid refinement for the Seban-McLaughlin test case (see below) produced insignificant changes in heat transfer coefficient.

The Reynolds numbers of the U-bend computations do not correspond exactly with those of the experiments principally because computational work has proceeded in parallel with experiments and 'nominal' flow rates were adopted. At a Reynolds number of  $6 \times 10^4$  a difference of 10% in  $Re$  is known not to have a perceptible effect on the flow structure<sup>(II)</sup>.

II. Azzola and Humphrey [6] report measurements for two values of  $Re$ : 57,400 and 110,000. Differences in velocity profiles at these two Reynolds numbers are indistinguishable from experimental uncertainty.

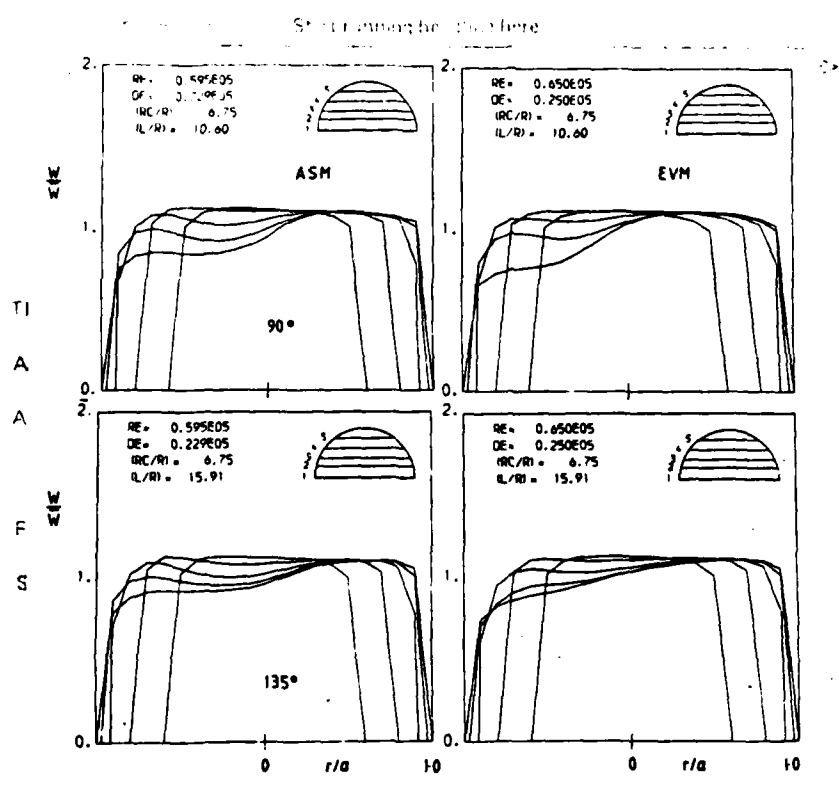


Fig. 4 ASM and EVM streamwise velocity profiles along surfaces parallel to plane of symmetry

a)  $\theta = 90^\circ$       b)  $\theta = 135^\circ$

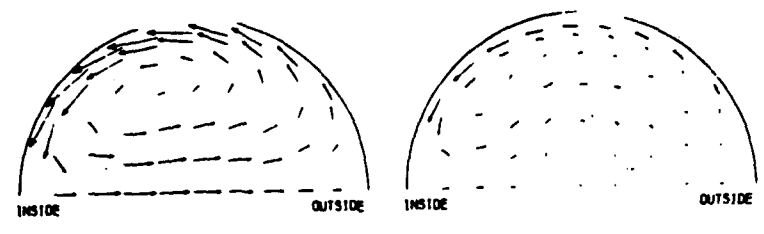


Fig. 6 ASM vector plots of secondary velocity. Arrow length such that 10% of pipe diameter corresponds to 16% of bulk streamwise velocity,  $W$ .

a)  $\theta = 45^\circ$       b)  $135^\circ$

----- Last line here ----->

Predicted levels of Nusselt number have been converted to the 'true' Reynolds number by multiplying by the ratio of the true to the computed Reynolds number to the power 0.8.

Azzola and Humphrey [21] report velocity profiles along the radial line for  $\phi = 90^\circ$ , i.e. orthogonal to the plane of symmetry. Their measurements of the streamwise velocity  $w$  are compared in Figure 3 with predictions of both the EVM and ASM schemes. Both models capture the overshoot of the mean velocity by  $90^\circ$  into the bend and the subsequent flattening of the velocity profile over the central core. As it turns out, the velocity distribution along this line is not a sensitive discriminator between the two models. Figure 4 therefore shows computed mean velocity distributions along lines parallel to the plane of symmetry of the flow at  $90^\circ$  and  $135^\circ$  into the U-bend. The ASM distributions show a more distinct secondary peak near the inside of the bend than those generated by the EVM. Based on our experience of flow in  $90^\circ$  bends [6] we have no doubt that the sharper peaking exhibited by the ASM computations better accords with the experimental behaviour.

The secondary (circumferential) velocity profile along the  $90^\circ$  line is compared with experiment at several stations in Figure 5. Both predicted curves indicate, in accord with experiment, that the peak secondary flow occurs at  $45^\circ$  and that by  $135^\circ$  the flow near the pipe centre is directed towards the inside of the bend. The overall implications of these changes in the profile are most clearly seen by the secondary flow vector plots of Figure 6: the conventional picture of the single-cell secondary circulation at  $45^\circ$  gives way at  $135^\circ$  to a kidney-shaped primary eddy and a weak counter-rotating secondary vortex near the tube centre. The ASM predictions in Figure 5 achieve somewhat closer agreement with the measured profiles than do the EVM calculations. The largest relative differences between the two numerical computations actually occur *downstream* of the bend, the ASM results showing a stronger movement towards (what had been) the inside of the bend than near the wall, the reverse of what the EVM predicts.

Turning now to the convective heat transfer results, the Nusselt number profiles for the Seban-McLaughlin coil shown in Figure 7 display a 2:1 variation in heat transfer coefficient between the inside and outside of the coil arising partly from the damping/augmentation of turbulence near the convex/concave surfaces and partly from the secondary flow. Since, for this case, the flow is fully developed in the streamwise direction, storage of the pressure field imposes no large core requirements. Accordingly, a second ASM computation was made with 40 radial and 30 circumferential nodes. The calculated levels of  $Nu$  differed by at most 14% from those obtained with the standard

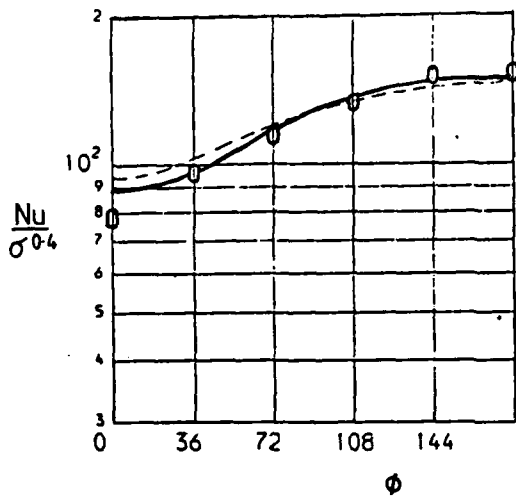


Fig. 7 Comparison of Nusselt numbers in flow through a coil,  $R/a = 10^4$   
 o Expt, [23]; — ASM; ---- EVM

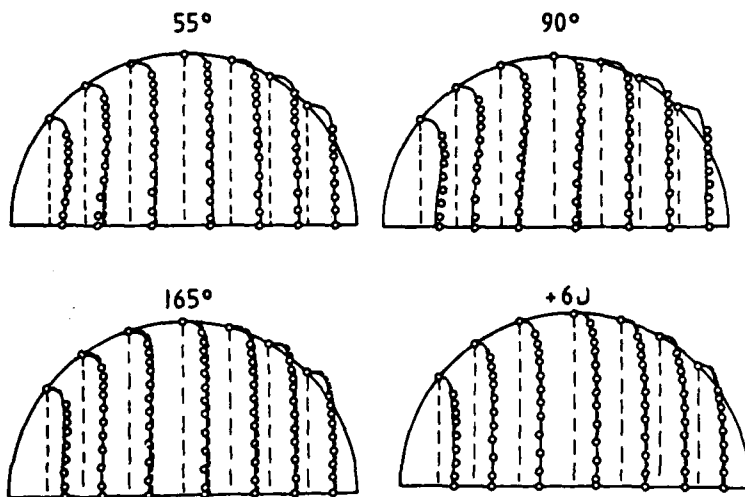


Fig. 8 Development of normalized temperature profiles in flow around a 180° bend; o Measurements [22];  
 — ASM; ---- EVM

28 x 24 mesh. The result helps confirm our view that numerical errors have been kept to unimportant levels. The circumferential variation of Nusselt number computed with the ASM is somewhat less than the measured though agreement is better than for the EVM results.

In fact, this set of measurements do not provide an ideal test case because experimental difficulties give rise to uncertainties in the data comparable with the differences shown between experiment and computation in Figure 7. The principal convective heat transfer test is thus the data of developing flow in a 180° bend obtained recently at UMIST [22]. The experiment is one at uniform wall temperature, the local heat flux being obtained by measuring the electrical power supply to a small circular disc required to keep the disc at the same temperature as the rest of the thick aluminium U-bend. Heating starts 30 diameters upstream of the bend so the thermal field is nearly fully developed at the start of the bend. The experimental uncertainty of the resultant Nusselt numbers is believed to be within ±7%. The geometric arrangement of the apparatus is a (roughly twice) scale replica of the U-bend of Azzola and Humphrey and the test flow Reynolds numbers in the two cases differ by no more than 5%. Moreover, the difference in temperature between the wall and the entering fluid was only 20°C so the thermal experiment was essentially one with uniform fluid properties. We may thus assume that the velocity field measured by Azzola and Humphrey [21] describes the hydrodynamic development in the thermal experiment also.

Normalized temperature profiles measured with a thermocouple rake are shown in Figure 8 for three positions in the bend and at 6 diameters downstream. The secondary circulation carries hot fluid from near the inside of the bend along the symmetry plane (viz. Figure 6) and this leads to an 'overshoot' in the temperature profile (III). The pattern is well reproduced by the two sets of predictions though, in so far as differences are discernible, the ASM computations give the better agreement with the measurements.

The development of the local Nusselt number around the bend is compared in Figure 9 with predictions generated by the two turbulence models; here, because the experiment was one of constant wall temperature, the variation of the bulk mean temperature around the bend is unknown. The Nusselt number presented in Figure 9 is thus based on the difference between the wall temperature and that at the centre of the pipe. The fully-developed flow Nusselt number for a straight

---

III. The normalization makes the coolest fluid correspond with the maximum in the temperature profile.

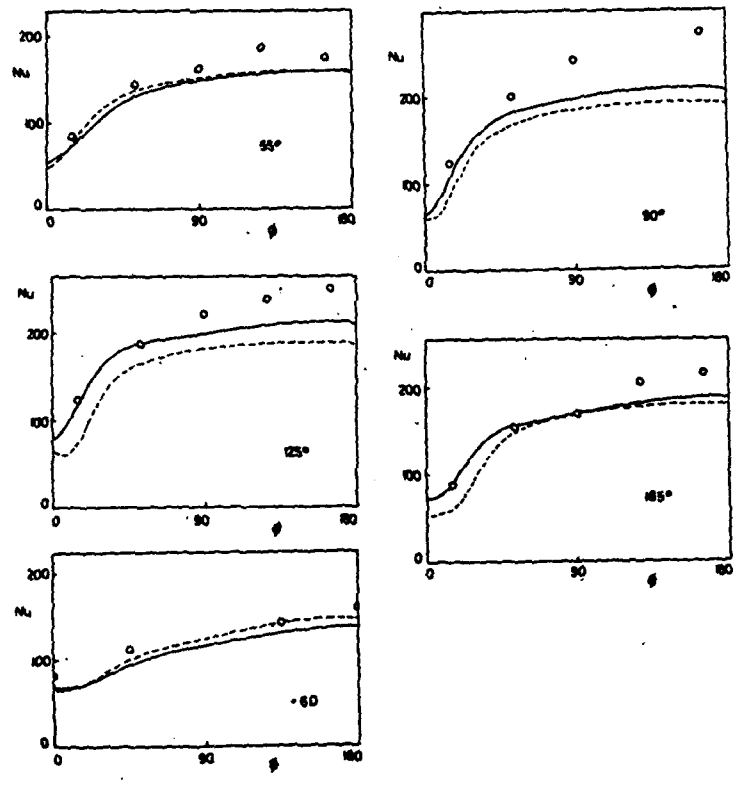


Fig. 9 Development of local Nusselt number around 180° bend  
Key as Fig. 8

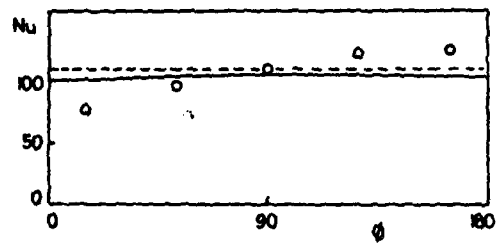


Fig. 10 Local Nusselt number at  $\theta = 15^\circ$  showing effects of laminarization. Key as Fig. 8.

tube at this Reynolds number is about 110. As the flow develops around the bend the Nusselt number is depressed on the inside of the bend and augmented on the outside. The maximum level occurs at the 90° station with a ratio of maximum:minimum Nu of about 3.5:1. Over the second half of the bend there is a gradual reduction in this ratio and in the average level. At 55° the two predicted curves show nearly the same distribution reproducing fairly well the measurements through with levels about 10% lower. By 90° significant differences have developed both between the predictions themselves and the measurements and predictions. The Nu levels given by the EVM are substantially too low over the whole circumference - nearly 30% low near the outside of the bend. The ASM results accord more closely with the data, particularly over the inside of the bend, but they still give values of Nu nearly 25% below the measurements at the outside. A similar pattern is exhibited at 125° and 165°. At the former position we note that the EVM predicts a minimum Nu off the symmetry plane but the ASM curve is in markedly better agreement with experiment, the maximum disagreement with experiment now being only 15%. Downstream of the bend the ASM predictions display a faster decay towards fully developed flow than the EVM and in Figure 9(c) this model predicts levels of Nu slightly below the EVM values. We have seen earlier that the secondary flow behaviour (Figure 5) indicated that the ASM computations predict more correctly the downstream recovery so the 'good' performance of the EVM at this station is really a fortuitous outcome of a weakness in the model.

Finally, we must draw attention to an interesting anomaly in the predicted heat transfer behaviour at the entry to the bend. At 15° into the bend, Figure 10, the experimental data indicate that the heat transfer coefficient on the inner line of symmetry is more than 40% below that on the outside whereas the predictions show an essentially uniform level. This might seem to suggest that the computations were not responding rapidly enough to the effects of applying curvature of the streamlines. However, the streamwise acceleration on the inside of the bend is rather severe at the bend entry: the parameter  $-(v/U_1^2) \partial p / r \partial \theta$  reaches a value in excess of  $2 \times 10^{-2}$ . If this strength of acceleration were applied to a two-dimensional boundary layer laminarization would occur. When applied for only a short distance complete reversion to laminar flow does not occur but the viscous sublayer becomes substantially thicker than normal substantially increasing thermal resistance and thus reducing the heat transfer coefficient. On the outside of the bend there is a substantial adverse pressure gradient that will tend to thin the sublayer producing the reverse effect to that found on the inside of the bend. Not unexpectedly our computations based on the standard Van Driest mixing length treatment for the near-wall region

entirely miss this unforeseen (and hitherto unreported) phenomenon at entry to the bend. It is, of course, possible to tune the mixing length hypothesis to reproduce at least partially this laminarization by making  $A^+$  a function of the local acceleration (this has been done in many mixing-length variants of the late '60s). A better approach, however, would probably be to employ a low-Reynolds-number version of the 2-equation EVM, for example [13], which is known to do fairly well at predicting laminarization without introducing flow-dependent parameters into the model coefficients.

## 5. CONCLUSIONS

The paper has reported the various tactics adopted to achieve convergent numerical predictions of strongly three-dimensional flow incorporating an algebraic stress model of turbulence and has presented predictions for flow in a 180° U-bend. Apart from the partial laminarization that appears to occur at entry to the bend, overall, the ASM-based computations have achieved a satisfactory simulation of the resultant flow and thermal fields. Indeed, this model achieves consistently better results than the EVM, albeit at the expense of roughly double the computational effort. A remaining weakness of the model is that heat transfer coefficients are predicted significantly too low on the outside (concave surface) of the bend. A more detailed experimental mapping of the mean and turbulent velocity field in this flow would be very helpful in tracing the source of this disagreement in the model.

## ACKNOWLEDGEMENTS

The work has been carried out in close collaboration with Prof. J.A.C. Humphrey and his group at the University of California, Berkeley who kindly provided their experimental results prior to publication. Prof. Humphrey also supplied his early toroidal-coordinate laminar flow solver which provided the starting point for developing the code used in this work. Sponsorship has been provided by the US Office of Naval Research (Power Program) through grant N00014-83-G-0021. We appreciate the unswerving support of the ONR technical monitor, Keith Ellingsworth. The camera-ready manuscript was prepared by Mrs. L.J. Ball and Mr. J. Batty traced many of the figures.

Authors' names appear alphabetically.

## REFERENCES

1. PRATAP, S.V. and SPALDING, D.B. - Aero. Quart., 1975, 26, 219.

2. CHANG, S.M., HUMPHREY, J.A.C., JOHNSON, R.W. and LAUNDER, B.E. - Proc. 4th Symp. Turbulent Shear Flows 6.20, University of Karlsruhe, 1983.
3. BIRCH, N. - 'The calculation of 3-D flow in curved ducts using Q385', Rep.TSG0161, Rolls-Royce, Derby, 1984.
4. HUMPHREY, J.A.C., IACOVIDES, H. and LAUNDER, B.E. - 'Some numerical experiments on developing laminar flow in circular-sectioned bends', J. Fluid Mech. To appear 1985.
5. IACOVIDES, H. and LAUNDER, B.E. - Proc. 1st U.K. National Heat Transfer Conf., I. Chem. E. Symp. Series No.86, 1984, 2, 1097.
6. AZZOLA, J., HUMPHREY, J.A.C., IACOVIDES, H. and LAUNDER, B.E. - Submitted to ASME J. Fluids Eng., 1985.
7. BRADSHAW, P. - Agardograph 169, 1973.
8. RODI, W. - ZAMM, 1976, 56, 1976.
9. SHIR, C.C. - J. Atmos. Sci., 1973, 30, 1327.
10. GIBSON, M.M. and LAUNDER, B.E. - J. Fluid Mech.
11. JOHNSON, R.W. - PhD Thesis, Faculty of Technology, University of Manchester, 1984.
12. TAVOULARIS, and CORRISIN, S. - Int. J. Heat & Mass Trans., 28, 265, 1984.
13. JONES, W.P. and LAUNDER, B.E. - Int. J. Heat & Mass Transfer, 1972, 15, 301.
14. KOOSINLIN, M.L., LAUNDER, B.E., and SHARMA, B.I. - J. Heat Transfer, 1974, 94C, 204.
15. VAN DRIEST, E.R. - J. Aero. Soc., 1956, 23, 1007.
16. IACOVIDES, H. - PhD Thesis, Faculty of Technology, University of Manchester, 1985.
17. LEONARD, B.P. - Comp. Meth. Appl. Mech. Engrg., 1979, 19, 59.
18. PATANKAR, S.V. - Numerical Heat Transfer and Fluid Flow, Hemisphere Publishing Corp.-McGraw Hill, 1980.
19. IACOVIDES, H. and LAUNDER, B.E. - 'PSL - An economical approach to the numerical analysis of near-wall elliptic flow', ASME J. Fluids Engrg., 106, 241, 1984.

20. HUANG, P.G. and LESCHZINER, M.A. - 'Stabilization of re-circulating-flow computations with second-moment closures and 3rd-order discretization', to appear on Proc. 5th Turbulent Shear Flow Symp., Cornell, August 1985.
21. AZZOLA, J. and HUMPHREY, J.A.C. - 'Developing turbulent flow in a 180° curved pipe and its downstream tangent', Rep. LBL-17681, Materials Science & Molecular Research Div., LBL, 1984.
22. BAUGHN, J.W., IACOVIDES, H., JACKSON, D.C. and LAUNDER, B.E. - 'Field temperatures and local heat fluxes in turbulent flow around a 180° bend', submitted to Int. J. Heat & Mass Transfer, 1985.
23. SEBAN, R.A. and MCLAUGHLIN, E.F. - Int. J. Heat & Mass Transfer, 1963, 6, 387.

END

DATE  
FILMED

1 - 86

DTIC

END

DATE  
FILMED

1 - 86

DTI